

ib



Una publicación de:
SOMIB
Sociedad Mexicana
de Ingeniería Biomédica

Revista Mexicana de Ingeniería Biomédica

New publishing model

Continuous publication:
once a manuscript is accepted and
prepared, it will be released online



SOMIB
Sociedad Mexicana
de Ingeniería Biomédica

Sociedad Mexicana de Ingeniería Biomédica

La Mesa Directiva de la Sociedad Mexicana de Ingeniería Biomédica hace una extensa invitación a las personas interesadas en participar, colaborar y pertenecer como Socio Activo de la SOMIB. La SOMIB reúne a profesionistas que se desarrollan en áreas de Ingeniería Biomédica, principalmente ingenieros biomédicos, así como otros profesionistas afines con el desarrollo de tecnología para la salud.

Membresía Estudiante

\$1,400.00 PESOS MXN

15% de descuento para grupos de 5 o más personas.

Membresía Profesionista

\$2,400.00 PESOS MXN

15% de descuento para grupos de 5 o más personas.

Membresía Institucional

\$11,600.00 PESOS MXN

No aplica descuento.

Membresía Empresarial

\$20,000.00 PESOS MXN

No aplica descuento.

EL PAGO CUBRE UN AÑO DE CUOTA. EN CASO DE REQUERIR FACTURA FAVOR DE SOLICITARLA, ADJUNTANDO COMPROBANTE DE PAGO Y ESPECIFICANDO CONCEPTO, AL CORREO ELECTRÓNICO: gerencia@somib.org.mx

Para ser socio

- Realiza el pago de derechos, de acuerdo a la categoría que te corresponde.
- Ingresa a www.somib.org.mx/membresias y elige el tipo de membresía por el cual realizaste el pago de derechos.
- Completa el formulario correspondiente y envíalo.
- Se emitirá carta de aceptación y número de socio por parte de la mesa directiva (aprobada la solicitud).
- Para mayor información sobre beneficios, ingresa a www.somib.org.mx; o escribe a gerencia@somib.org.mx.

Datos bancarios

- Beneficiario:** Sociedad Mexicana de Ingeniería Biomédica A. C.
- Banco:** Scotiabank
- Referencia:** 1000000333
- Cuenta:** 11006665861
- CLABE Interbancaria:** 044770110066658614

ib Revista Mexicana de Ingeniería Biomédica

AUTORES

Los trabajos a publicar en la RMIB, deben ser originales, inéditos y de excelencia. Los costos de publicación para autores son los siguientes:

NO SOCIOS: \$200 DÓLARES AMERICANOS

SOCIOS: \$150 DÓLARES AMERICANOS

PUBLICIDAD

A las empresas e instituciones interesadas en publicitar su marca o productos en la RMIB, los costos por número son los siguientes:

MEDIA PLANA: \$4,999.00 PESOS MXN (INCLUYE I.V.A.)

UNA PLANA: \$6,799.00 PESOS MXN (INCLUYE I.V.A.)

CONTRAPORTADA: \$7,799.00 PESOS MXN (INCLUYE I.V.A.)

FORROS INTERIORES: \$7,799.00 PESOS MXN (INCLUYE I.V.A.)

DESCUENTO DEL 20% AL CONTRATAR PUBLICIDAD EN DOS O MÁS NÚMEROS.

La inserción de la publicidad será publicada en el libro electrónico y en el área de patrocinios en el sitio Web de la revista (RMIB), disponible en:

<http://rmib.mx>

Fundador
Dr. Carlos García Moreira

COMITÉ EDITORIAL

Editora en Jefe
Dra. Dora-Luz Flores Gutiérrez
UNIVERSIDAD AUTÓNOMA DE BAJA CALIFORNIA

Editores Asociados Nacionales

Dr. Christian Chapa González
UNIVERSIDAD AUTÓNOMA DE CIUDAD JUÁREZ

Dra. en C. Citlalli Jessica Trujillo Romero
DIVISIÓN DE INVESTIGACIÓN EN INGENIERÍA MÉDICA
INSTITUTO NACIONAL DE REHABILITACIÓN "LUIS GUILLERMO IBARRA IBARRA"

Dr. Rafael Eliecer González Landaeta
UNIVERSIDAD AUTÓNOMA DE CIUDAD JUÁREZ

Dra. Rebeca Romo Vázquez
UNIVERSIDAD DE GUADALAJARA

Dra. Isela Bonilla Gutiérrez
UNIVERSIDAD AUTÓNOMA DE SAN LUIS POTOSÍ

Comité Editorial Internacional

Dr. Leonel Sebastián Malacrida Rodríguez
UNIVERSIDAD DE LA REPÚBLICA, URUGUAY

Dra. Elisa Scalco
INSTITUTE OF BIOMEDICAL TECHNOLOGY
ITALIAN NATIONAL RESEARCH COUNCIL, MILAN, ITALY

Dra. Natali Olaya Mira
INSTITUTO TECNOLÓGICO METROPOLITANO
ITM, MEDELLÍN, COLOMBIA

Índices

La Revista Mexicana de Ingeniería Biomédica aparece en los siguientes índices científicos:
Sistema de Clasificación de Revistas Científicas y Tecnologías del CONACYT - Q4, SCOPUS, SciELO, EBSCO, LATINDEX, Medigraphic Literatura Biomédica, Sociedad Iberoamericana de Información Científica - SIIC.

www.rmib.mx
ISSN 2395-9126

Asistente Editorial
Carla Ivonne Guerrero Robles

Editor Técnico y en Internet
Enrique Ban Sánchez

Se autoriza la reproducción parcial o total de cualquier artículo a condición de hacer referencia bibliográfica a la Revista Mexicana de Ingeniería Biomédica y enviar una copia a la redacción de la misma.



Sociedad Mexicana de Ingeniería Biomédica

Juan Vázquez de Mella #481, Polanco I Sección, Alc. Miguel Hidalgo, C. P. 11510, Ciudad de México, México, (555) 574-4505



SOMIB
Sociedad Mexicana
de Ingeniería Biomédica

MESA DIRECTIVA

Ing. Francisco Javier Aceves Aldrete

PRESIDENTE

Mtra. Natalia Gabriela Sámano Lira

VICEPRESIDENTA

Mtra. Verónica Guadalupe Castillo Sánchez

TESORERA

Ing. Janette Mariana Tarín León

SECRETARÍA GENERAL

Dra. Dora-Luz Flores

EDITORA EN JEFE DE RMIB

Afiliada a:

International Federation of Medical and Biological Engineering (IFMB-IUPSM-ICSU)
Federación de Sociedades Científicas de México, A.C. (FESOCIME)
Consejo Regional de Ingeniería Biomédica para América Latina (CORAL)

SOMIB

Juan Vázquez de Mella #481, Polanco I Sección, Alc. Miguel Hidalgo, C. P. 11510, Ciudad de México, México (555) 574-4505

www.somib.org.mx

REVISTA MEXICANA DE INGENIERÍA BIOMÉDICA, Vol. 43, No. 2, Mayo-Agosto 2022, es una publicación cuatrimestral editada por la Sociedad Mexicana de Ingeniería Biomédica A.C., Juan Vázquez de Mella #481, Polanco I Sección, Alc. Miguel Hidalgo, C. P. 11510, Ciudad de México, México, (555) 574-4505, www.somib.org.mx, rmib.somib@gmail.com. Editora responsable: Dra. Dora-Luz Flores. Reserva de Derechos al Uso Exclusivo No. 04-2015-041310063800-203, ISSN (impreso) 0188-9532; ISSN (electrónico) 2395-9126, ambos otorgados por el Instituto Nacional del Derecho de Autor. Responsable de la última actualización de este número: Lic. Enrique Federico Ban Sánchez, Juan Vázquez de Mella #481, Polanco I Sección, Alc. Miguel Hidalgo, C. P. 11510, Ciudad de México, México, (555) 574-4505, fecha de última modificación, 20 de agosto de 2022.

El contenido de los artículos, así como las fotografías son responsabilidad exclusiva de los autores. Las opiniones expresadas por los autores no necesariamente reflejan la postura del editor de la publicación.

Queda estrictamente prohibida la reproducción total o parcial de los contenidos e imágenes de la publicación sin previa autorización de la Sociedad Mexicana de Ingeniería Biomédica.

Disponible en línea:

www.rmib.mx

CONTENTS
CONTENIDO

Contents p 5

Review Article p 6

Hydroxyapatite and Biopolymer Composites with Promising Biomedical Applications

Research Article p 24

Studying the Effect of Temperature on the Tensile Strength of an Intravascular Catheter Using a Degradation Model

Estudiando el Efecto de la Temperatura en la Resistencia Tensil de un Catéter Intravascular Usando un Modelo de Degradación

Research Article p 39

Comparison of Accuracy of Color Spaces in Cell Features Classification in Images of Leukemia types ALL and MM

Comparación de Precisión de Espacios de Color en la Clasificación de Características de Células en Imágenes de Leucemia tipos ALL y MM

Research Article p 53

Retinal Lesion Segmentation Using Transfer Learning with an Encoder-Decoder CNN

Segmentación de Lesiones en la Retina Usando Transferencia de Conocimiento con CNN Encoder-Decoder

Research Article p 64







Secure Exchange of Medical Images Via Extended Visual Cryptography

Intercambio Seguro de Imágenes Médicas Mediante Criptografía Visual Extendida

dx.doi.org/10.17488/RMIB.43.2.1

E-LOCATION ID: 1245

Hydroxyapatite and Biopolymer Composites with Promising Biomedical Applications

Juanita Daria Flores Valdez¹  , Aidé Sáenz Galindo¹ , Claudia Magdalena López Badillo¹ ,
Adali Oliva Castañeda Facio¹ , Pablo Acuña Vazquez² 

¹Facultad de Ciencias Químicas, Universidad Autónoma de Coahuila

²Centro de Investigación en Química Aplicada

ABSTRACT

The purpose of tissue engineering (regenerative medicine) is to develop materials that replace human tissue, having as main characteristics' biodegradability, biocompatibility, no toxicity, osteoconductivity, which lead to cell maturation and proliferation. Due to the importance of the development of this type of materials, several researchers have used biopolymers and calcium phosphate salts (hydroxyapatite) as composites to be used in this area as drug releases, scaffolds, implants, among others. Different biopolymers can be suitable for this type of application, in this work we have described the most widely used biopolymers for biomedical purposes, such as alginate, collagen, gelatin gum, chitosan, and polylactic acid, in addition to a detailed description of hydroxyapatite, biopolymers, as well as biopolymer/hydroxyapatite composites, to highlight their potential and the most relevant characteristics of these materials.

KEYWORDS: Composites, Hydroxyapatite, Biopolymers

Corresponding author

TO: Juanita Daria Flores Valdez
INSTITUTION: Facultad de Ciencias Químicas,
Universidad Autónoma de Coahuila
ADDRESS: Blvd. Venustiano Carranza #935
y José Cárdenas Valdés, Col. República, C. P. 25280,
Saltillo, Coahuila, México
CORREO ELECTRÓNICO: juanitaflores@uadec.edu.mx

Received:

14 February 2022

Accepted:

25 April 2022

INTRODUCTION

Currently, bone diseases are estimated to be one of the main causes of disability in humans. Osteoporosis, for example, causes approximately 9 million bone fractures worldwide with a high risk of morbidity and mortality of 12-20 % of sufferers [1]. A bone replacement must imitate the tissue by replicating its structural and functional requirements, in such a way that it generates an adequate response from the biological system to which it has been subjected [2]. To achieve this, the use of tissue engineering (TE) has been applied, which is a multidisciplinary science that uses the principles of engineering and life sciences to improve or develop biomaterials that generate a suitable microenvironment through the combination of cell [3]. The objective of TE is to produce biomaterials that are biocompatible, biodegradable, bioactive, capable of promoting cell proliferation, non-toxic, and osteoconductive, in order to provide similar characteristics to the cellular configuration of human tissue [4] [5].

Hence, several researches have developed biomaterials capable of satisfying this type of needs through the use of composite materials based on ceramics and biopolymers, since they have been shown to have a great similarity with bone tissue, since it consists of an inorganic phase (minerals such as calcium phosphate) and an organic phase (collagen and proteins) [6].

In this paper, given the importance of the development of this type of biomaterials, an extensive literature review has been carried out about the most utilized biopolymers in composites with inorganic hydroxyapatite phase, which have potential biomedical applications, describing the generalities of each of them, as well as recent research on this type of biomaterials.

MATERIALS AND METHODS

A bibliographic review was carried out to collect information about hydroxyapatite, biopolymers, as well as biopolymer/hydroxyapatite composites using the key-

words hydroxyapatite, biopolymers, polymer matrix composites, tissue engineering, composite procurement, etc. Original papers and books were taken into account, both in English and Spanish, published in scientific journals indexed in Scopus, Science Direct, Google Scholar, and Web of Science. No limits on the year of publication were used, but the articles published in the last ten years were chosen for the description of how biopolymer/hydroxyapatite composites are obtained, selecting a total of 132 references including both articles and books.

RESULTS AND DISCUSSION

Hydroxyapatite

The skeleton of the average adult is composed of 40% bone structure with size and shape defined for specific functions, the most important of which are to facilitate movement, protect vital organs, store minerals, deposit bone marrow, and provide the support structure of the body [7] [8]. Human bone is a complex dynamic tissue of dense nature, its extracellular matrix is composed mainly of collagen fiber (organic phase 30%) and the mineral part of which the major component is calcium phosphates (inorganic phase 70%). The inorganic content of the bone matrix is hydroxyapatite (Ha), which in combination with other biomaterials has been demonstrated to provide biocompatibility, biodegradability, and osteoconductivity [4] [9].

Ha is closely related to basic calcium phosphate, which is the predominant inorganic material in the bones of all vertebrates, as well as in dental enamel. Has the chemical formula $\text{Ca}_{10}(\text{PO}_4)_6(\text{OH})_2$, this phosphate crystallizes in a hexagonal form, see Figure 1, with a P63/m symmetry group, with lattice parameters $a = b = 9.432 \text{ \AA}$ and $c = 6.88 \text{ \AA}$, it is commonly obtained in aqueous conditions and often tends to have particle sizes around 5 to 1 nm, so they have a large surface area, which intensifies its chemical activity. The ionic character of the Ha makes it a hard ceramic, refractory, with a melting point above 1600 C [10] [11] [12].

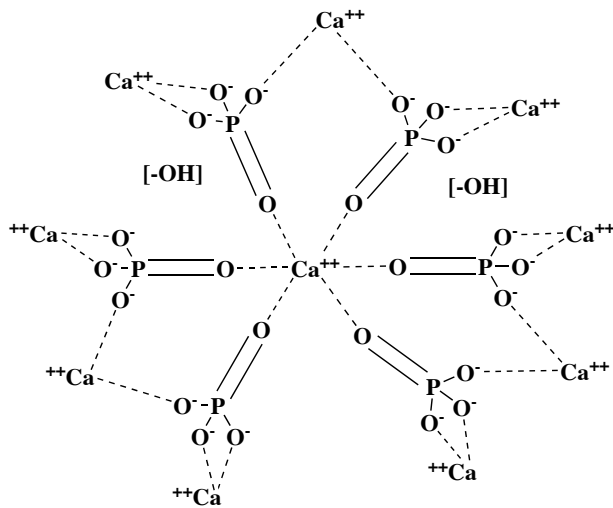


FIGURE 1. Chemical structure of the Ha.

Ha's biomedical applications have been of great relevance due to their high degree of biocompatibility and bioactivity. Has been employed in the manufacture of different scaffold systems, including porous structures and hydrogels, with potential applications for the regeneration of bone tissue [13], and several methods have been developed to obtain this material, the main ones being precipitation, sol-gel, mechanochemistry, and solid-state reaction.

Ha can be obtained from natural sources, the most well-known are eggshells, corals, and animal bones, through thermal treatments at high temperatures [14]. Figure 2 provides a general description of the methodologies used to obtain Ha.

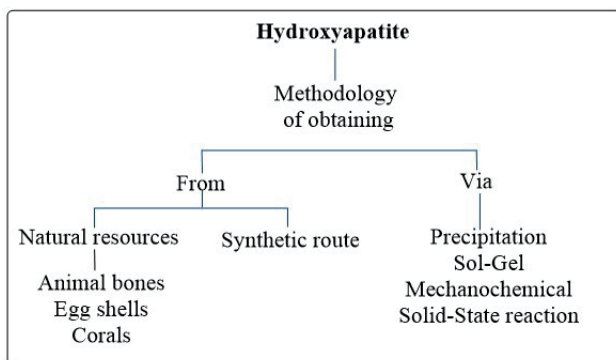


FIGURE 2. General scheme of the methodology to obtain Ha.

Biopolymers

The prefix "bio" indicates that these polymers are obtained from living matter or natural sources such as animals, plants, and microorganisms. They possess diverse characteristics such as biodegradability, low toxicity, biocompatibility, etc., which make them good candidates for a wide range of applications ranging from food and textiles up to electronics and medicine [15].

However, the term "biopolymer" is not strictly defined in the literature. There is some ambiguity in the term's biopolymers, biodegradable polymers, bio-based polymers and bioplastics [16]. Biopolymers are those polymers that are derived from natural resources and exhibit biodegradability, but do not include synthetic polymers that are biodegradable, they are also often referred to as natural polymers [17]. Biodegradable polymers include polymers of both natural and synthetic origin and are also known as bioresorbable polymers [18]. Bio-based polymers are those that are obtained partially or totally from renewable resources or waste and can be biodegradable or non-biodegradable [19]. And bioplastics can become biodegradable even if they are not necessarily derived from natural sources [20].

Biopolymers have been designed by nature itself with a single purpose, the sustenance of life. They can be grouped in different ways [21], as illustrated in Figure 3. Based on their nature, they are classified into three main categories: polysaccharides, proteins, and nucleic acids, where polysaccharides are macromolecular chains of low molecular weight that are linked by covalent sugar bonds, the best-known being glucose compounds or their derivatives such as starch and cellulose, which make the structure of plants. The proteins are the most important macromolecules present in animals, these are formed by the polymerization of amino acids, each type of protein has its own sequence of amino acids and structure which make its purpose determined, the most well-known proteins are hemoglobin, collagen, albumin, lactin, among others. Nu-

cleic acids are linear polymers formed mainly of sugar molecules, phosphates, and bases, the most mentioned are RNA and DNA, which are found in living organisms for the purpose of storing and reading genetic information [22] [23] [24]. Depending based on their polymeric structure are polysaccharides, polyesters, polypeptides, polyamides, polyurethanes, and vinyl polymers [25].

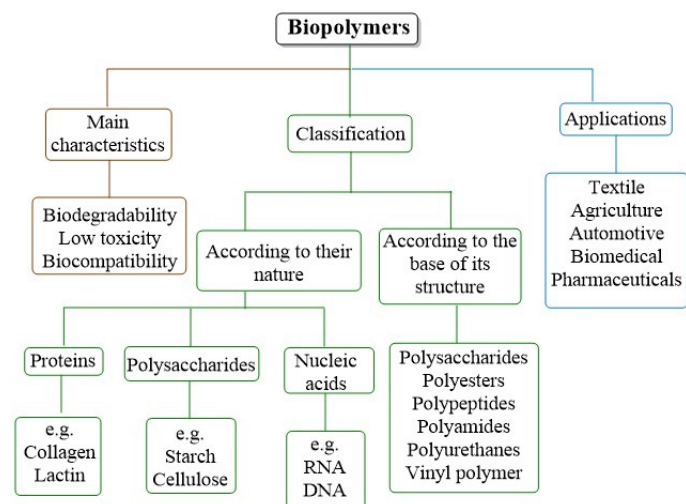


FIGURE 3. General information about biopolymers.

Due to the characteristics of biopolymers, they have become a tendency for their use in diverse applications, among which the pharmaceutical and biomedical areas stand out [22]. For this reason, the design of new materials based on biopolymers or biomaterials that include a composite of a polymer and a material in order to be compatible with human tissue, is one of the most promising areas in reconstructive medicine and orthopedics. In the case of implants made from biopolymers, they are used as a temporary osteoconductive scaffold, to which new bone tissue, compatible with the biopolymer, will eventually be anchored and grow. One of the greatest advantages of biopolymers in this area is that the implants do not require additional surgical intervention to remove them from the organism. Although one limitation they may have is their low mechanical properties since their high Young's modulus does not allow them to maintain the mor-

phology of the polymeric implants under the load suffered by the musculoskeletal system [26] [27] [28]. Biopolymers, therefore, tend to have a wide field of utility, since they can be used for prostheses and implants, bone cements, and components of artificial organs [29].

Composites

Composites are materials consisting of two phases, illustrated in Figure 4, where the first is called the discontinuous or dispersed phase (reinforcement or filler) and the second is the continuous or "matrix" phase. The reinforcements or fillers can be fibers, particles, or sheets, whereas the matrix is the predominant phase [30].

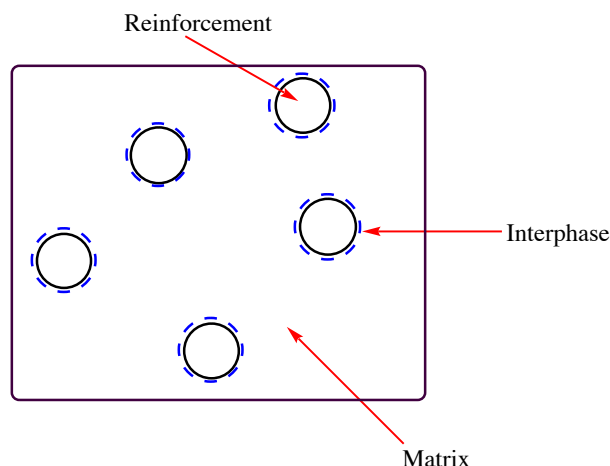


FIGURE 4. Phases of a composite.

Composite materials have originated since old times, human beings have used them for different purposes, such as hunting weapons [31], in the same way nature provides these materials, for example, wood is composed of cellulose fibers in a lignin matrix, or the bones of mammals are constituted by collagen fibers in a calcium phosphate matrix [32].

These materials are developed to enhance their properties in relation to their pure components. The most desirable characteristics of these composites are their physicochemical properties, such as resistance to chemical attack, high mechanical properties, as well as favoring their use in everyday life. In the develop-

ment of these composites, the aim has been to combine the properties of two or more components in a single compound, as well as to generate energy savings both in their production and application [33]. Based on this range of qualities, composites are considered as a feasible replacement for conventional materials in several industries such as aerospace, automotive, medical, among others [34].

Biopolymers and calcium phosphate salts composites have been used for bone replacement, because biopolymers are a good substitute for synthetic polymers, in addition to the fact that their composition can imitate the extracellular matrix due to the fact that they are bioabsorbable, biocompatible, and biodegradable. This type of materials with biomedical applications must have a great similarity with the structure and composition of the components present in the molecular structure of living beings; in this sense, proteins and polysaccharides are widely used in TE and regenerative medicine [35]. Therefore, the following sections will describe biopolymer/hydroxyapatite composites with potential biomedical applications, focusing on the most widely used for this purpose.

Alginate/Hydroxyapatite (Alg/Ha)

Alginic acid, also called alginate (Alg), occurs in nature mainly in brown algae (Phaeophyceae). Alg is an non-branched linear polysaccharide composed of the monomers $\beta(1-4)$ D-mannuronic acid and $\alpha(1-4)$ L-guluronic acid, referred to as M- and G-block, respectively [36], its chemical structure is shown in Figure 5. Alg has diverse properties such as biodegradability, biocompatibility, bioadhesiveness, low toxicity, hydrophilicity, non-immunogenic effects, low cost, in addition to the fact that with the presence, even in low concentrations, of different cations (K^+ , Na^+ , Ca^{2+} , Mg^{2+} , Ba^{2+} , and Sr^{2+}) a stable hydrogel can be formed, due to the carboxylate groups of Alg [37]. In recent years, Alg has been reported to be utilized in medicine as a surgical and wound dressing [38], as a drug releas-

ing agent and as a scaffold for bone, cartilage and/or skin [39]. These characteristics have led to it being widely studied as it is considered suitable for use in TE due to its biocompatibility with living cells and its property for the formation of hydrogels [40].

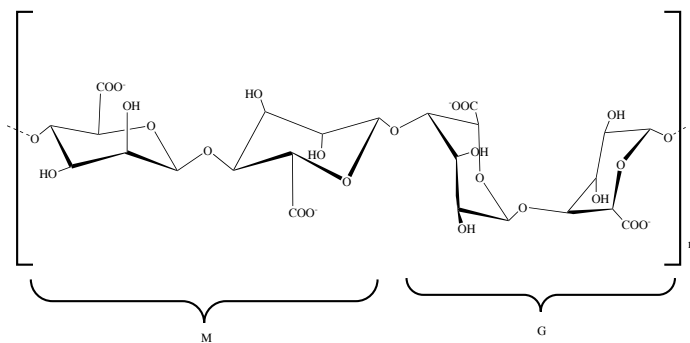


FIGURE 5. Chemical structure of sodium alginate.

With respect to Alg/Ha composites, these have been prepared by various processes and techniques, such as freeze-drying, electrospinning, extrusion, layer-by-layer, uniaxial hot pressing, liquid-gas systems, impregnation, coprecipitation [41], but the method most commonly used to obtaining them is crosslinking, however, it generally leads to a lack of homogeneity causing a decrease in mechanical properties [42].

Different researchers have developed this type of composites, such as that carried out in 2021 by Ocando *et al.*, who report obtaining an Alg/Ha composite in which Ha was doped with Mg, since it plays an important role in the proliferation of osteoblasts. In this work they obtained a biomaterial, by means of the crosslinking method, highly porous, with a uniform morphology, good biocompatibility and bioactivity [43].

This type of composite provides an improvement in different properties like mechanical strength, porosity, cell adhesion, biocompatibility, excellent osteogenic differentiation and mineralization [44], good bone regeneration, and can be used in the fixation of bone implants [45]. Table 1 shows the description of Alg/Ha systems where in some cases there are three-phase systems.

TABLE 1. Description and application of Alg/Ha systems.

System	Possible applications	Properties/Results	Ref.
Alg/Ha-DS	Drug release	The <i>in-situ</i> production of Ha into the Alg polymeric matrix allowed for reduced swelling and dissolution rate. It was successfully applied to the release of the drug diclofenac sodium (DS) and a controlled release of up to 8 h was obtained.	[97]
Alg/Ha-CHX	Drug release in dentistry	The composite demonstrated good stability due to electrostatic interactions between chlorhexidine (CHX), Ha and Alg. In addition, a controlled release of CHX was achieved, obtaining the highest concentration at 72 h.	[98]
Alg/Ha	Implant	This composite developed was shown to have biological control within the subject under study, and the bone formed around the biomaterial had a lamellar structure, demonstrating that the biomaterial induces rapid bone production.	[99]
Alg/Ha	Biomedical application	The Alg/Ha composite tended to have better bioresorption at a higher weight percentage of Alg. An improvement in mechanical properties was also found compared to pure Ha and Alg.	[100]
Alg/Ha/MWCNT	Tissue engineering	The developed a composite with high porosity and showed improved compressive strength (72.02 ± 1.7 kPa). In addition, improved biocompatibility, differentiation and cell attachment were observed in the MG-63 cell line.	[101]
Alg/Ha	Tissue engineering	The obtained a composite that proved to have good biocompatibility and biodegradability. A histological study determined that the scaffolds developed can support both endochondral and intramembranous bone formation, and the defect was completely regenerated after 6 months.	[102]
Alg/Ha	Coatings	This composite showed improved mechanical properties and in microbiological studies they found that the composite significantly reduced the growth of the gram-positive bacterial <i>L. monocytogenes</i> compared to the pure Alg.	[103]

Collagen/Hydroxyapatite (Col/Ha)

Collagen (Col), specifically type I, is the most abundant protein in the human body and can be found in different mammalian tissues such as the cornea, cartilage, skin, bones, tendons, ligaments, and others. It provides mechanical strength and stimulates cell adhesion and proliferation [36]. Is arranged as a triple helical structure which is mostly stabilized by hydrogen bridges [46] as shown in Figure 6. Has several properties that make it unique such as biodegradability, non-immunogenicity, bioabsorbability, and biocompatibility [47] [48].

Col has been used in TE and regenerative medicine for many years due to its biocompatibility and low immunogenicity, however, by itself it is not naturally osteoconductive and tends to have low compressive strength [49]. Col/Ha composites have been successfully

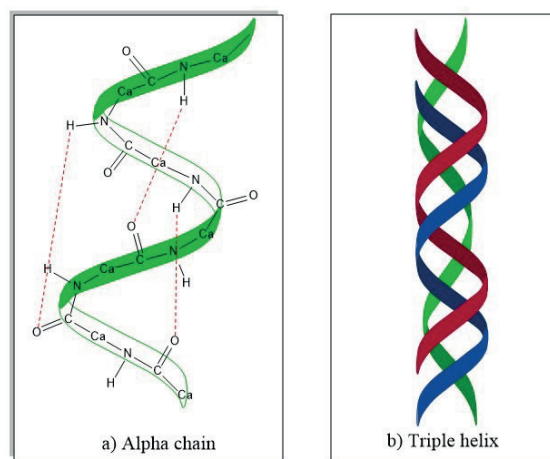


FIGURE 6. Chemical structure of collagen.

used in tissue procurement, since this combination provides good mechanical properties and osteoconductivity, in addition to favoring cell adhesion, cell migration, vascularization and osteoblastic differentiation [50]. In the same way, several researchers have

opted for Col as the polymeric matrix par excellence in this type of composites since it is naturally present in the composition of human bones ^[51].

Col/Ha composites have been commonly obtained by different methods ^{[52] [53] [54]}:

- a) Mixing in collagen solution with Ha powder and subsequent lyophilization.
- b) Co-Precipitation of Ca and P precursors in collagen solution.
- c) Crosslinking for hydrogel formation.
- d) Mechanical mixing.
- e) Electrochemical deposition.

Studies realized in 2018 by Kaczmarek *et al.*, demonstrated that this type of composites shows an increment in osteoconductivity, mechanical properties, and biocompatibility ^[55], in the same sense these authors also found with this composite a high cell proliferation and a high mineralization potential ^{[56] [57]}.

Similarly, these biomaterials have a great potential to be applied in regenerative medicine through implants and/or bone tissue regenerator ^[58]. In addition, it can be used as a controlled drug release system thanks to its absorbent properties ^[59]. For a clearer comprehension, Table 2 presents a brief overview of Col/Ha systems.

TABLE 2. Description of Col/Ha systems.

System	Possible applications	Properties/Results	Ref.
Col/Ha	Tissue engineering	The composite has a bone composition similar to human bone and was shown to have superior mechanical properties compared to pure Col, thus providing reinforcement at the interphase.	[104]
Col/Ha	Tissue engineering	The developed composite showed to be doubled in strength with respect to its mechanical properties, thanks to the strengthening of the chemical bonds that occur between the Col-Ha, in addition, the scaffold maintained fibrillar structures and appropriate porosity, which permits a good cell proliferation.	[105]
Col/Ha/Graphene	Coatings	A composite with a composition very similar to that of human bone was developed and successfully electrodeposited on the surface of a Ti16Nb alloy. This coating provided a hydrophilic surface suitable for fibroblast cell development and adhesion.	[106]
Col/Ha	Bone defects	The composite produced adequately retains some trace elements that help its biocompatibility, thanks to the Ha synthesized from bovine bones, so it has a good bioactivity and can be used as a bone repair material.	[107]
Col/Ha/CNT	Bone replacement	This composite increased the flexural strength and fracture toughness up to 3%, and also exhibited positive osteoblast cell growth, thus improving its biological properties.	[108]
Col/Ha	Implant and bone regeneration	The composite exhibited a cell viability of 108.9 %, inferring that Ha and Col are biocompatible and non-toxic, since a viability above 100 % indicates cell proliferation.	[109]
Col/Ha	Tissue engineering	In the development of this composite obtained a high porosity of between 85-90 %, they also found an improvement in the compressive modulus obtaining a value over 1MPa, they also demonstrated that the architecture, permeability and composition of the scaffold favor infiltration and differentiation in vitro after subcutaneous implantation, proving that this type of scaffolds are osteoinductive.	[110]
Col/Ha	Tissue engineering	The composite shows good swelling properties, having that crosslinking and concentration of Col and Ha is important to modify the microstructure, mechanical properties and degradation rate of the composite.	[111]

Gellan Gum/Hydroxyapatite (GG/Ha)

Natural gums can be obtained from different sources such as vegetable fibers (gum arabic, gum ghatti, gum tragacanth, etc.), seeds (guar gum, konjac gum, etc.), algae (agar-agar gum, alginates, etc.), or microorganisms (gellan gum, xanthan gum, rhamsan gum, etc.)^[60].

Microbial gums are of high molecular weight, approximately 1,000,000 Da, and are composed of carbohydrates, proteins, lipids, and humic substances. Are produced by certain microorganisms from the aerobic fermentation of sugar^[61], Gellan gum (GG) is an exopolysaccharide of anionic nature consisting of a repeating unit of a tetrasaccharide (D-glucose, 1-3, glucuronic acid, D-glucose and 1,4, L-rhamnose), see Figure 7.

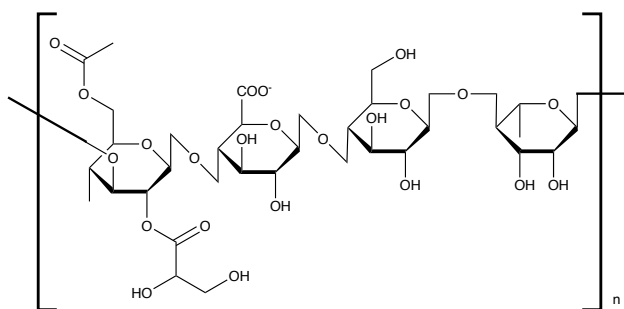


FIGURE 7. Chemical structure of gellan gum.

Similar to Alg, GG forms gels in presence of metal ions and can be easily processed^[36], some of the main characteristics of GG are its non-toxicity, biocompatibility, and biodegradability.

This polysaccharide is produced by the excretion of the bacteria *Sphingonomas elodea* and *Sphingomonas paucimobilis*. In addition, is highly thermally stable and the gels obtained are mainly translucent^[62] and have high porosity, antibacterial nature, proliferation, and bone formation^[63]. They are commonly prepared by lyophilization, rehydration, and co-precipitation for the formation of cellular adhesive sponge-type hydrogels^[64]. Diverse studies have shown that the gelation temperature, strength, texture, clarity, and speed of gel formation depend directly on the pH value during the obtaining process^[60].

Due to its characteristics, GG has been used in diverse applications in the food, cosmetic and pharmaceutical industries; in the last of these, its application in ophthalmology, drug release, cell immobilization, biosensor synthesis, among others, stands out^[64]. In recent decades, GG has been studied for numerous applications in cellular tissue, including brain TE, dentistry, cartilage, and intervertebral disc^[65]. Shin *et al.* employed the photoreticulation reaction in order to obtain rigid microgels of GG. The product obtained was immersed in a modified gelatin solution, which was photoreticulated, and the final material showed increased mechanical strength^[66].

On the other hand, several studies report that it is possible to increase the mechanical strength of GG by adding calcium phosphate salts, such as Ha. These inorganic particles can be easily incorporated into hydrogels by mechanical mixing^[67]. Previous studies have shown that mineralization of GG hydrogels could enhance mechanical properties, as well as promote cell adhesion and growth, and osteogenic differentiation^[68].

Recent research by Pereira *et al.* at 2018 successfully reported the obtaining of a GG/Ha composite by incorporating different concentrations of Ha (5, 10, 15, and 20 %) using the crosslinking method, obtaining a material with improved mechanical properties, high stability in degradation and promoting high cell proliferation, null toxicity, and excellent biocompatibility^[69]. The Table 3 shows the description of GG/Ha composites.

Chitosan/Hydroxyapatite (Ch/Ha)

Chitin is the second most abundant organic compound on planet earth, it is a biopolymer found in various living organisms, such as the animal, plant, and fungi kingdoms. It is found in the exoskeleton of crustaceans, the cuticle of insects, and cell walls of fungi, for example, in shrimp, lobsters, crabs, squid, mollusks, scorpions, ants, beetles, cockroaches, bees, spiders, *Agaricus bisporus*, *Aspergillus niger*, *Auricularia auriculajudae*, and others. Chitin is an effective material for suturing, wound heal-

TABLE 3. Description of GG/Ha systems.

System	Possible applications	Properties/Results	Ref.
GG/Ha	Bone repairment	The addition of Ha in the polymeric matrix of GG is reported to favor mechanical strength.	[112]
GG/Ha	Bone regeneration	This composite was made in 3D which allowed a maturation of the bone cells because it assimilates the structure of human bone.	[113]
GG/Ha	Bone reconstruction	The obtained composites showed high mechanical strength, good porosity with the capacity to absorb nutrients necessary for proper cell growth, as well as slow degradation, which provides the necessary time to induce osteoconduction and the generation of new bone.	[114]
GG/Ha	Bone replacements	The addition of Ha in the GG polymer matrix provides good cell adhesion on the surface of the material. in addition, it was observed that increasing the percentage of Ha significantly increased the proliferation of MC3T3-E1 cells.	[115]
GG/Ha	Bone grafting	The developed material improved its mechanical properties with respect to pure GG, in addition to showing a clear organization of the cytoskeleton and cell motility from day 7. Hence, this composite favors cell adhesion and propagation.	[116]
GG/Ha-Ce	Bone grafting	A composite of GG/Ha developed with the addition of doped cerium (Ce) to the hydroxyapatite. This material demonstrated high porosity, increased mechanical properties, and demonstrated that it is non-toxic and biocompatible.	[117]

ing and drug release thanks to its biocompatibility, non-toxicity, immunogenicity, biodegradability and antimicrobial activity [70]. Although the most important aspect of chitin is its main derivative, chitosan (Ch), which is obtained by deacetylation of chitin. Chemically, Ch has a similar structure to cellulose and chitin, as shown in Figure 8, its differentiator is the functional group at the C-2 position. While cellulose has a hydroxyl group (-OH) and chitin has an N-acetylamine group (-NHCOOH₃), Ch has an amino group (-NH₂). Ch is a linear polysaccharide consisting of an acetylated unit (N-acetyl-2-amino-2-deoxy-d-glucopyranose) and a deacetylated unit (2-amino-2-deoxy-d-glucopyranose), where the repetitive units are linked by $\beta(1-4)$ glycosidic bonds [71]. The degree of deacetylation and molecular weight are of major influence on the physicochemical properties of Ch, where the degree of deacetylation represents the ratio of glucosamine to N-acetyl-glucosamine [72].

Non-toxicity, biodegradability, biocompatibility, antimicrobial activity, anticancer activity, antiinflammatory, hydrophilicity, crystallinity, immunogenicity, cell

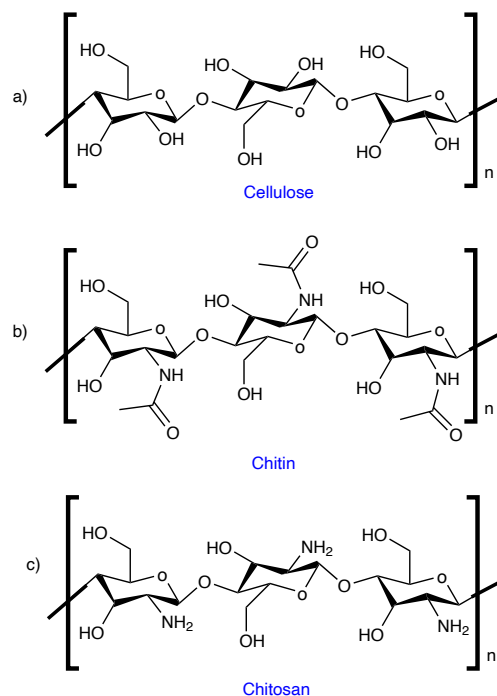


FIGURE 8. Chemical structure of cellulose (a), chitin (b) and chitosan (c).

adhesion, cell proliferation and differentiation, and osteoconductivity [73] [74] [75] are some of the properties of Ch which make it unique. For this reason, it has been

used in countless applications in the food industry, agriculture, pharmacy, medicine, dentistry, ophthalmology, cosmetics, the textile industry, veterinary medicine, wastewater treatment, and has also been used in the formulation of fire-retardant foams, among others [71] [76] [77]. Ch has been shown to be suitable for use in IT as a bone tissue graft, in the manufacture of porous scaffolds, films for superficial wounds, drug release, and in formulations for the production of hydrogels [78].

However, Ch presents as a disadvantage its poor mechanical properties [79], so to improve this, several investigations report the development of composites based on Ch/Ha because both biomaterials present excellent biocompatibility with human cellular tissue [80], it is reported that this composite presents improvements in its mechanical properties, due to the binding of the amino and hydroxyl groups of Ch to the calcium ions present in Ha [81] [82]. The Ch/Ha composite can be produced mainly by freeze-drying; this technique is one of the most widely used to obtain scaffolds, and other techniques can also be used, such as NSN textile methodology for the production of fibrous structures and the use of enzymes. This composite can be used as a bioactive interface between the metallic implant and the human bone [75]. In 2017 Okada *et al.*, used the coagulation method to obtain a Ch/Ha composite fiber, where they reported that this material improves the mechanical properties [83]. Also, Balagangadharan *et al.*, reported in 2018 the development of a Ch/Ha composite to which they added ZrO₂ nanoparticles obtaining scaffolds, which presented an osteoconductive improvement and osteoblast differentiation, resulting in a beneficial composite for bone tissue regeneration [84]. Descriptions of some of the Ch/Ha systems are presented in Table 4.

Polylactic Acid-Hydroxyapatite (PLLA/Ha)

Polylactic acid (PLLA), its chemical structure can be seen in Figure 9, is a linear aliphatic thermoplastic polyester derived 100% from renewable resources with wide availability of raw materials (sugar, corn,

potatoes, sugarcane, sugar beet, among many others) [85]. This material is simple to process, using any technique, such as extrusion, injection and compression molding, thermoforming and foaming, as well as blow molding, electrospinning, spinning, and stretching of molten polymer, among others. Extrusion is commonly used for PLA processing because it can be adapted for various applications [86]. The industry most known is packaging; in fact, it is approved by the United States Food and Drug Administration (FDA) [87], for its excellent properties of transparency, low toxicity, versatility, osteoconductivity, biodegradability, biocompatibility, bioresorbability [88], properties influenced by its molecular weight and stereochemistry [89].

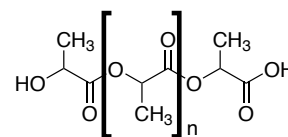


FIGURE 9. Chemical structure of polylactic acid.

PLLA exists in two stereoisomeric forms D-PLLA (DPLLA) and L-PLLA (PLLA), and a mixture of D- and L-lactic acid also exists as D,L-PLLA (PDLLA). Polymers derived from the optically active D- and L-monomers are semi-crystalline and those derived from the optically inactive D,L-PLLA are amorphous. Generally, L-PLLA is preferred for applications where high mechanical strength and toughness are required, for example, orthopedic devices and sutures. On the other hand, due to the amorphous nature of D,L-PLLA is considered for drug release applications, since for this purpose it is very important to have a homogeneous dispersion of the active species within a matrix. It has been reported that PLLA degradation is significantly affected with increasing crystallinity, so the mixture of PLLA and PDLLA is effective in adjusting the crystallization and morphology of the polymer, and thus its mechanical properties [90]. In recent years, it has been successfully used as a surgical implant material, drug release, and in the fabrication of 3D printed scaffolds [91].

TABLE 4. Description of Ch/Ha systems.

System	Possible applications	Properties/Results	Ref.
Ch/Ha/Magnetite	Superficial wounds	The Ch/Ha composite increases the bending modulus up to 2.6 GPa, with the addition of magnetite, however, it showed a lower bending strength. In contrast, magnetic nanoparticles had no negative effect on the cytocompatibility of the material.	[118]
Ch/Ha	Coatings	The composites developed showed good swelling and crosslinking properties, and the L929 and Saos-2 cell lines showed cell proliferation.	[119]
Ch/Ha-DOX	Drug release	This study incorporated an anticancer drug (doxorubicin, DOX) into Ha nanoparticles modifying this with Ch. The modified Ha did not show cytotoxicity in the MG-63 cell line.	[120]
Cu-Ch/Ha-Sr	Tissue engineering	The composite showed an improvement in the mechanical properties of Ch, as well as excellent cell infiltration, cell migration and neovascularization due to the high porosity, making them cytocompatible.	[121]
MWCNT-Ch/Ha	Bone replacements	The nanocomposite exhibited excellent mechanical properties, good biocompatibility and bioactivity, hence fulfilling the required properties of the extracellular matrix of bone.	[122]
Ch/Ha	Bone replacements and coatings	The composite had a tensile strength of 30-70 MPa, showed to be cytocompatible in the L929 cell line after 24 h of incubation.	[123]
Ch/HaNPsAg	Drug release and implant	This type of scaffolds exhibited an improvement in mechanical resistance, as well as improved cell penetration, adhesion and propagation. The presence of silver nanoparticles (NPsAg) provides antibacterial activity, thus reducing the risk of infections.	[124]
Ch/Ha	Tissue engineering	The composite showed a high similarity compared to natural bone. Also observed that increasing the concentration of Ha resulted in a higher adhesion of osteoblasts. In addition, this material showed a high degree of proliferation in the MC3T3-E1 cell line. Compared to the pure Ch scaffold, the compressive strength increased by 33.07 %.	[125]

A disadvantage that PLLA may present is the absence of the property that facilitates cell binding on its surface and its proliferation, due to a scarcity of cell binding capacity [92]. This deficiency in cohesion could be improved by employing the addition of Ha as a strategy since calcium phosphates promote cell proliferation on the scaffold surface. It has also been shown that PLA/Ha composites tend to enhance their overall properties such as biocompatibility, resorbability, osteoconductivity, cell proliferation, and mechanical strength [93].

The dispersion of Ha on PLA is considered one of the critical factors that determine the properties of the composite, for which different methods and techniques are used to obtain it, highlighting melt mixing, electrospinning, processing by compression, emulsion and solvent casting, the latter being the most used [94]. On the other hand, Zhang *et al.*, reported in 2015 the obtaining of a

PLA/Ha composite by the electrospinning method, which led to an easily obtained material with great potential in terms of its biomedical applications such as rapid mineralization and high biocompatibility [95]. Also, at 2019 de Moura *et al.*, obtained a PLA/Ha material with improved mechanical resistance and bioactivity, reported that the addition of Ha increases the protein adsorption capacity, suppresses cell death by apoptosis, and creates a favorable microenvironment for cell proliferation [96]. The table 5 present a description of the PLLA/Ha systems and their potential application.

CONCLUSIONS

Biopolymers are materials used in a diversity of applications due to their excellent qualities such as biodegradability, biocompatibility, and non-toxicity, therefore several researchers have studied them for their application in tissue engineering, however, these materials have poor

TABLE 5. Description of PLLA/Ha systems.

System	Possible applications	Properties/Results	Ref.
PLLA/Ha	Bone replacements	The composite had an increase in Young's modulus incorporating a low quantity of Ha in the polymeric matrix. It was also demonstrated that the material is not cytotoxic in the MC3T3-E1 cell line, in besides having a good osteoblastic maturation.	[126]
PLLA/Ha	Bone tissue engineering	The developed composite has a hydrophilic part of the Ha, which contributes to cell growth and bone repair, as well as a hydrophobic part of the PLLA, which acts as a barrier between tissues. As a result, this material has a high cytocompatibility.	[127]
PLLA/Ha-NPsAg	Coatings	The antimicrobial activity of the composite exhibited better inhibition efficacy on <i>E. coli</i> bacteria. In the hemocompatibility assay showed 2 % hemolytic activity, so it is considered compatible with human blood.	[128]
PLLA/Ha	Coatings	The composite shown that the mechanical properties and thermal behavior increased with the addition of Ha to the PLLA matrix. In addition, the material exhibited good biocompatibility.	[129]
PLLA/Ha	Scaffold	The composite demonstrated mechanical properties comparable to those of normal bone. Furthermore, it exhibited excellent 3D printability at 90:10 ratio of PLLA/Ha respectively.	[130]
PLLA/Ha	Scaffold	The composite demonstrated good adhesion and cellular proliferation in the material, with adequate osteoconductivity.	[131]
PLLA/Ha	Scaffold	The composite showed good adhesion and cell proliferation on the surface, adequate porosity, as well as an increase in mechanical properties with respect to pure PLLA.	[132]

mechanical properties. In response to this mechanical deficiency, composites based on biopolymers/calcium phosphate salts (hydroxyapatite) have been used, since it has been shown that these types of materials show improvements in their mechanical properties and biocompatibility. For this reason, these composites are a viable option for the development of biomaterials that can be used in different applications in tissue engineering, such as drug delivery, tissue implants, scaffolds, etc.

AUTHOR CONTRIBUTIONS

J.D.F.V. conceptualized the project, performed bibliographical research, and provided briefing to the team members to carry out the project, participated in the writing of the original manuscript and translated it to the English language. A.S.G. provided funding through a SEP-CONACYT grant for basic science, specially used for providing payment for publication; oversaw the scheduling and progress of the project; contributed to the writing of the manuscript, mainly with comments from her field of expertise. C.M.L.B. contributed to the

writing of the manuscript, especially with topics regarding her field of expertise, provided bibliographical resources key to the finalization of the project and helped with the English translation. A.O.C.F. contributed to writing the draft and final version of the manuscript, edited comments on her field of expertise key to the conclusion of the project. P.A.V. conceptualized the project, designed the objectives of the project, and oversaw its development; participated in all the writing stages of the manuscript and helped with the translation to English language. All authors reviewed and approved the final version of the manuscript.

ACKNOWLEDGMENTS

To CONACYT for the scholarship 1078907 awarded. As well as to the support provided to CONACYT through the Project SEP-CONACYT Basic Sciences 2017-2018 CB2017-2018 A1-S-44977.

CONFLICTS OF INTEREST

The authors do not report any conflict of interest.

REFERENCES

- [1] El-Habashy SE, Eltahir HM, Gaballah A, Zaki EI, et al. Hybrid bioactive hydroxyapatite/polycaprolactone nanoparticles for enhanced osteogenesis. *Mater Sci Eng C* [Internet]. 2021;119:111599. Available from: <https://doi.org/10.1016/j.msec.2020.111599>
- [2] Escobar Sierra D, Mesa Ospina D. Evaluación de recubrimientos de quitosano sobre cuerpos porosos de hidroxiapatita. *Sci Tech* [Internet]. 2019;24(1):161-172. Available from: <https://doi.org/10.22517/23447214.20051>
- [3] Chen J, Yu Q, Zhang G, Yang S, et al. Preparation and biocompatibility of nanohybrid scaffolds by in situ homogeneous formation of nano hydroxyapatite from biopolymer polyelectrolyte complex for bone repair applications. *Colloids Surf B* [Internet]. 2012;93:100-107. Available from: <http://dx.doi.org/10.1016/j.colsurfb.2011.12.022>
- [4] Chakravarty J, Rabbi MF, Chalivendra V, Ferreira T, et al. Mechanical and biological properties of chitin/poly(lactide) (PLA)/hydroxyapatite (HAP) composites cast using ionic liquid solutions. *Int J Biol Macromol* [Internet]. 2020;151:1213-1223. Available from: <https://doi.org/10.1016/j.ijbiomac.2019.10.168>
- [5] Kalisz G, Przekora A, Kazimierczak P, Gieroba B, et al. Physicochemical changes of the chitosan/ β -1,3-glucan/hydroxyapatite biocomposite caused by mesenchymal stem cells cultured on its surface in vitro. *Spectrochim Acta A Mol Biomol* [Internet]. 2021;251:119439. Available from: <https://doi.org/10.1016/j.saa.2021.119439>
- [6] Benedini L, Laiuppa J, Santillán G, Baldini M, et al. Antibacterial alginate/nano-hydroxyapatite composites for bone tissue engineering: Assessment of their bioactivity, biocompatibility, and antibacterial activity. *Mater Sci Eng C* [Internet]. 2020;115:111101. Available from: <https://doi.org/10.1016/j.msec.2020.111101>
- [7] Sathiyavimal S, Vasantharaj S, Lewis Oscar F, Selvaraj R, Brindhadevi K, Pugazhendhi A. Natural organic and inorganic-hydroxyapatite biopolymer composite for biomedical applications. *Prog Org Coat* [Internet]. 2020;147:105858. Available from: <https://doi.org/10.1016/j.porgcoat.2020.105858>
- [8] Lett AJ, Sagadevan S, Fatimah I, Hoque ME, et al. Recent advances in natural polymer-based hydroxyapatite scaffolds: Properties and applications. *Eur Polym J* [Internet]. 2021;148:110360. Available from: <https://doi.org/10.1016/j.eurpolymj.2021.110360>
- [9] Trakoolwannachai V, Kheolamai P, Ummartyotin S. Characterization of hydroxyapatite from eggshell waste and polycaprolactone (PCL) composite for scaffold material. *Compos B Eng* [Internet]. 2019;173:106974. Available from: <https://doi.org/10.1016/j.compositesb.2019.106974>
- [10] Williams RAD, Elliot JC. Bioquímica dental básica y aplicada. Distrito Federal, México: El Manual Moderno; 1990. 263p. Spanish.
- [11] Rahavi SS, Ghaderi O, Monshi A, Fathi MH. A comparative study on physicochemical properties of hydroxyapatite powders derived from natural and synthetic sources. *Russ J Non-Ferrous Metals* [Internet]. 2017;58(3):276-286. Available from: <https://doi.org/10.3103/S1067821217030178>
- [12] Giraldo-Betancur A, Espinosa-Arbelaez DG, del Real-López A, Millan-Malo BM, et al. Comparison of physicochemical properties of bio and commercial hydroxyapatite. *Curr Appl Phys* [Internet]. 2013;13(7):1383-1390. Available from: <http://dx.doi.org/10.1016/j.cap.2013.04.019>
- [13] Alvarez-Barreto J, Márquez K, Gallardo E, Moret J, et al. Mesenchymal Stem Cell Culture on Composite Hydrogels of Hydroxyapatite Nanoparticles and Photo-Crosslinking Chitosan. *Rev Mex Ing Biom* [Internet]. 2017;38(3):524-536. Available from: <http://dx.doi.org/10.17488/RMIB.38.3.2>
- [14] Rivera JA, Fetter G, Bosch P. Efecto del pH en la síntesis de hidroxiapatita en presencia de microondas. *Rev Mater* [Internet]. 2011;15(4):488-505. Available from: <https://doi.org/10.1590/S1517-70762010000400003>
- [15] Flores-Valdez JD, Sáenz-Galindo A, Múzquiz-Ramos EM, Soria Aguilar MJ. Biopolymers and applications. *CienciaCierta* [Internet]. 2021;(66):61-72. Available from: <http://www.cienciacierta.uadec.mx/articulos/CC66/biopolimerosyaplicaciones.pdf>
- [16] Sivakanthan S, Rajendran S, Gamage A, Madhujith T, et al. Antioxidant and antimicrobial applications of biopolymers: A review. *Food Res Int* [Internet]. 2020;136:109327. Available from: <https://doi.org/10.1016/j.foodres.2020.109327>
- [17] Lizundia E, Kundu D. Advances in Natural Biopolymer-Based Electrolytes and Separators for Battery Applications. *Adv Funct* [Internet]. 2021;31(3):2005646. Available from: <https://doi.org/10.1002/adfm.202005646>
- [18] Hochmańska-Kaniewska P, Janiszewska D, Oleszek T. Enhancement of the properties of acrylic wood coatings with the use of biopolymers. *Prog Org Coat* [Internet]. 2022;162:106522. Available from: <https://doi.org/10.1016/j.porgcoat.2021.106522>
- [19] Tuan Naiwi TSR, Aung MM, Rayung M, Ahmad A, et al. Dielectric and ionic transport properties of bio-based polyurethane acrylate solid polymer electrolyte for application in electrochemical devices. *Polym Test* [Internet]. 2022;106:107459. Available from: <https://doi.org/10.1016/j.polymertesting.2021.107459>
- [20] Wan Mahari AW, Kee SH, Foong SY, Amelia TSM, et al. Generating alternative fuel and bioplastics from medical plastic waste and waste frying oil using microwave co-pyrolysis combined with microbial fermentation. *Renew Sustain Energy Rev* [Internet]. 2022;153:111790. Available from: <https://doi.org/10.1016/j.rser.2021.111790>
- [21] Parveen FK. Recent Advances in Biopolymers [Internet]. London: IntechOpen; 2016. 288p. Available from: <https://doi.org/10.5772/60630>
- [22] Narain, R. Polymer Science and Nanotechnology Fundamentals and Applications [Internet]. United Kingdom: Elsevier; 2020. 488p. Available from: <https://doi.org/10.1016/C2018-0-01134-2>
- [23] Rebelo R, Fernandes M, Fangueiro R. Biopolymers in Medical Implants: A Brief Review. *Procedia Eng* [Internet]. 2017;200:236-243. Available from: <https://doi.org/10.1016/j.proeng.2017.07.034>
- [24] Hassan MES, Bai J, Dou D-Q. Biopolymers; Definition, Classification and Applications. *Egypt J Chem* [Internet]. 2019;62(9):133-145. Available from: <https://dx.doi.org/10.21608/ejchem.2019.6967.1580>
- [25] Ahmed S, Kanchi S, Kumar G. Handbook of Biopolymers: Advances and Multifaceted Applications. California: Jenny Stanford Publishing; 2018. 308p.
- [26] Dubinenko GE, Zinoviev AL, Bolbasov EN, Novikov VT, et al. Preparation of Poly(L-lactic acid)/Hydroxyapatite composite scaffolds by fused deposit modeling 3D printing. *Mater Today Proc* [Internet]. 2020;22:228-234. Available from: <https://doi.org/10.1016/j.matpr.2019.08.092>

- [27] Kumar PPP, Lim D-K. Gold-Polymer Nanocomposites for Future Therapeutic and Tissue Engineering Applications. *Pharmaceutics* [Internet]. 2021;14(1):70. Available from: <https://doi.org/10.3390/pharmaceutics14010070>
- [28] Biswal T. Biopolymers for tissue engineering applications: A review. *Mater Today Proc* [Internet]. 2021;41:397-402. Available from: <https://doi.org/10.1016/j.matpr.2020.09.628>
- [29] Villareal Valdiviezo GP, Múzquiz Ramos EM, Farías Cepeda L. Medical applications of biopolymers. *CienciaCierta* [Internet]. 2020;63:83. Available from: <http://www.cienciacierta.uadec.mx/articulos/CC63/83AplicacionesMedicas.pdf>
- [30] Aboudi J, Arnold SM, Bednarczyk BA. *Mechanics of Composite Materials* [Internet]. 2nd ed. Butterworth-Heinemann: Elsevier; 2013. 984p. Available from: <https://doi.org/10.1016/C2011-0-05224-9>
- [31] Gay D, Hoa SV, Tsai SW. *Composite Materials: Design and Applications*. 1st ed. Florida: CRC Press; 2002. 552p.
- [32] Gibson RE. *Principal of Composite Mechanics*. 4th ed. Boca Raton: CRC Press; 2016. 700p.
- [33] Mohanty AK, Misra M, Drzal LT, Selke S, Harte B, Hinrichsen G. *Natural Fibers, Biopolymers, and Biocomposites* [Internet]. 1st ed. Boca Raton: CRC Press; 2005. 896p. Available from: <https://doi.org/10.1201/9780203508206>
- [34] Sankaran S, Ravishankar BN, Ravi Sekhar K, Dasgupta S, et al. Syntactic Foams for Multifunctional Applications. In: Kar, K (eds.). *Composite Materials* [Internet]. Berlin: Springer Berlin Heidelberg; 2017. 281-314p. Available from: https://doi.org/10.1007/978-3-662-49514-8_9
- [35] Holban AM, Grumezescu A (eds.). *Materials for Biomedical Engineering: Hydrogels and Polymer-based Scaffolds* [Internet]. Amsterdam, Oxford, Cambridge: Elsevier; 2019. 562p. Available from: <https://doi.org/10.1016/C2017-0-04477-4>
- [36] Moraes MA, Silva CF, Vieira RS (eds.). *Biopolymers Membranes and Films Health, Food, Environment, and Energy Applications*. Amsterdam, Oxford, Cambridge: Elsevier; 2020. 633p. Available from: <https://doi.org/10.1016/C2018-0-02693-6>
- [37] Benedini L, Laiuppa J, Santillán G, Baldini M, et al. Antibacterial alginate/nano-hydroxyapatite composites for bone tissue engineering: Assessment of their bioactivity, biocompatibility, and antibacterial activity. *Mater Sci Eng C* [Internet]. 2020;115:111101. Available from: <https://doi.org/10.1016/j.msec.2020.111101>
- [38] Wang L, Li Y, Li C. In situ processing and properties of nanostructured hydroxyapatite/alginate composite. *J Nanopart Res* [Internet]. 2009;11(3):691-699. Available from: <https://doi.org/10.1007/s11051-008-9431-y>
- [39] Chae T, Yang H, Leung V, Ko F, et al. Novel biomimetic hydroxyapatite/alginate nanocomposite fibrous scaffolds for bone tissue regeneration. *J Mater Sci: Mater Med* [Internet]. 2013;24(8):1885-1894. Available from: <https://doi.org/10.1007/s10856-013-4957-7>
- [40] Sukhodub LF, Sukhodub LB, Litsis O, Prylutsky Y. Synthesis and characterization of hydroxyapatite-alginate nanostructured composites for the controlled drug release. *Mater Chem Phys* [Internet]. 2018;217:228-34. Available from: <https://doi.org/10.1016/j.matchemphys.2018.06.071>
- [41] Mahmoud EM, Sayed M, El-Kady AM, Elsayed H, et al. In vitro and in vivo study of naturally derived alginate/hydroxyapatite bio composite scaffolds. *Int J Biol Macromol* [Internet]. 2020;165:1346-1360. Available from: <https://doi.org/10.1016/j.ijbiomac.2020.10.014>
- [42] You F, Chen X, Cooper DML, Chang T, et al. Homogeneous hydroxyapatite/alginate composite hydrogel promotes calcified cartilage matrix deposition with potential for three-dimensional bioprinting. *Biofabricación* [Internet]. 2018;11:015015. Available from: <https://doi.org/10.1088/1758-5090/aaf44a>
- [43] Ocando C, Dinescu S, Samoila I, Ghitulica CD, et al. Fabrication and properties of alginate-hydroxyapatite biocomposites as efficient biomaterials for bone regeneration. *Eur Polym J* [Internet]. 2021;151:110444. Available from: <https://doi.org/10.1016/j.eurpolymj.2021.110444>
- [44] Sukhodub LF, Sukhodub LB, Pogrebnyak AD, Turlybekuly A, et al. Effect of magnetic particles adding into nanostructured hydroxyapatite-alginate composites for orthopedics. *J Korean Ceram Soc* [Internet]. 2020;57(5):557-569. Available from: <https://doi.org/10.1007/s43207-020-00061-w>
- [45] De Paula FL, Barreto IC, Rocha-Leão MH, Borojevic R, et al. Hydroxyapatite-alginate biocomposite promotes bone mineralization in different length scales in vivo. *Front Mater Sci China*. 2009;3(2):145-153. Available from: <https://doi.org/10.1007/s11706-009-0029-9>
- [46] González Paz R, Grillo A, Feijoo JL, Noris-Suárez K, et al. Estudio de Mezclas de Polietileno de Alta Densidad (PEAD) con colágeno/acetato de sodio e Hidroxiapatita (HA). In: Müller-Karger C, Wong S, La Cruz A. (eds). *IV Latin American Congress on Biomedical Engineering 2007* [Internet]. Berlin: IFMBE Proceedings; 2008;18:676-680. Available from: https://doi.org/10.1007/978-3-540-74471-9_157
- [47] Yoruc ABH, Aydinoglu AK. Synthesis of Hydroxyapatite/Collagen (HA/COL) Composite Powder Using a Novel Precipitation Technique. *Acta Phys Pol* [Internet]. 2015;127(4):1264-1267. Available from: <http://dx.doi.org/10.12693/APhysPolA.127.1264>
- [48] Sukul M, Min Y-L, Lee B-T. Collagen-hydroxyapatite coated unprocessed cuttlefish bone as a bone substitute. *Mater* [Internet]. 2016;181:156-560. Available from: <http://dx.doi.org/10.1016/j.matlet.2016.05.170>
- [49] Lara-Rico R, Claudio-Rizo JA, Múzquiz-Ramos E, Lopez-Badillo CM. Hidrogeles de colágeno acoplados con hidroxiapatita para aplicaciones en ingeniería tisular. *TIP Rev Espec Cienc Quim-Biol* [Internet]. 2020;23:1-12. Available from: <https://doi.org/10.22201/fesz.23958723e.2020.0.224>
- [50] Cholas R, Padmanabhan SK, Gervaso F, Udayan G, et al. Scaffolds for bone regeneration made of hydroxyapatite microspheres in a collagen matrix. *Mater Sci Eng C* [Internet]. 2016;63:499-505. Available from: <http://dx.doi.org/10.1016/j.msec.2016.03.022>
- [51] Bhuiyan D, Jablonsky MJ, Kolesov I, Middleton J, et al. Novel synthesis and characterization of a collagen-based biopolymer initiated by hydroxyapatite nanoparticles. *Acta Biomater* [Internet]. 2015;15:181-190. Available from: <http://dx.doi.org/10.1016/j.actbio.2014.11.044>
- [52] Sun R-X, Lv Y, Niu Y-R, Zhao X-H, et al. Physicochemical and biological properties of bovine-derived porous hydroxyapatite/collagen composite and its hydroxyapatite powders. *Ceram Int* [Internet]. 2017;43(18):16792-16798. Available from: <http://dx.doi.org/10.1016/j.ceramint.2017.09.075>
- [53] Becerra J, Rodriguez M, Leal D, Noris-Suarez K, et al. Chitosan-collagen-hydroxyapatite membranes for tissue engineering. *J Mater Sci: Mater Med* [Internet]. 2022;33(2):18. Available from: <https://doi.org/10.1007/s10856-022-06643-w>

- [54] Zhao X, Li H, Xu Z, Li K, et al. Selective preparation and characterization of nano-hydroxyapatite/collagen coatings with three-dimensional network structure. *Surf Coat Technol* [Internet]. 2017;322:227-237. Available from: <http://dx.doi.org/10.1016/j.surfcoat.2017.05.042>
- [55] Kaczmarek B, Sionkowska A, Osyczka AM. Physicochemical properties of scaffolds based on mixtures of chitosan, collagen and glycosaminoglycans with nano-hydroxyapatite addition. *Int J Biol Macromol* [Internet]. 2018;118:1880-1883. Available from: <https://doi.org/10.1016/j.ijbiomac.2018.07.035>
- [56] Kaczmarek B, Sionkowska A, Gołyńska M, Polkowska I, et al. In vivo study on scaffolds based on chitosan, collagen, and hyaluronic acid with hydroxyapatite. *Int J Biol Macromol* [Internet]. 2018;118:938-944. Available from: <https://doi.org/10.1016/j.ijbiomac.2018.06.175>
- [57] Kikuchi M, Itoh S, Ichinose S, Shinomiya K, et al. Self-organization mechanism in a bone-like hydroxyapatite/collagen nanocomposite synthesized in vitro and its biological reaction in vivo. *Biomaterials* [Internet]. 2001;22(13):1705-1711. Available from: [https://doi.org/10.1016/S0142-9612\(00\)00305-7](https://doi.org/10.1016/S0142-9612(00)00305-7)
- [58] Dou DD, Zhou G, Liu HW, Zhang J, et al. Sequential releasing of VEGF and BMP-2 in hydroxyapatite collagen scaffolds for bone tissue engineering: Design and characterization. *Int J Biol Macromol* [Internet]. 2019;123:622-628. Available from: <https://doi.org/10.1016/j.ijbiomac.2018.11.099>
- [59] Taniyama T, Masaoka T, Yamada T, Wei X, et al. Repair of Osteochondral Defects in a Rabbit Model Using a Porous Hydroxyapatite Collagen Composite Impregnated With Bone Morphogenetic Protein-2. *Artif Organs* [Internet]. 2015;39(6):529-535. Available from: <https://doi.org/10.1111/aor.12409>
- [60] Osmalek T, Froelich A, Tasarek S. Application of gellan gum in pharmacy and medicine. *Int J Pharm*. 2014;466(1-2):328-340. Available from: <https://doi.org/10.1016/j.ijpharm.2014.03.038>
- [61] Zare EN, Makvandi P, Borzacchiello A, Tay FR, et al. Antimicrobial gum bio-based nanocomposites and their industrial and biomedical applications. *Chem Commun* [Internet]. 2019;55(99):14871-14885. Available from: <https://doi.org/10.1039/C9CC08207G>
- [62] Santos MVB, Oliveira AL, Osajima JA, Silva-Filho EC. Development of composites scaffolds with calcium and cerium-hydroxyapatite and gellan gum. *Ceram Int* [Internet]. 2020;46(3):3811-3817. Available from: <https://doi.org/10.1016/j.ceramint.2019.10.104>
- [63] Rajesh R, Ravichandran YD, Reddy MJK, Ryu SH, et al. Development of functionalized multi-walled carbon nanotube-based polysaccharide-hydroxyapatite scaffolds for bone tissue engineering. *RSC Adv* [Internet]. 2016;6(85):82385-82393. Available from: <http://dx.doi.org/10.1039/C6RA16709H>
- [64] Manda MG, da Silva LP, Cerqueira MT, Pereira DR, et al. Gellan gum-hydroxyapatite composite spongy-like hydrogels for bone tissue engineering. *J Biomed Mater Res A* [Internet]. 2018;106(2):479-490. Available from: <https://doi.org/10.1002/jbm.a.36248>
- [65] Vieira S, da Silva Morais A, Garet E, Silva-Correia J, et al. Self-mineralizing Ca-enriched methacrylated gellan gum beads for bone tissue engineering. *Acta Biomater* [Internet]. 2019;93:74-85. Available from: <https://doi.org/10.1016/j.actbio.2019.01.053>
- [66] Shin H, Olsen BD, Khademhosseini A. Gellan gum microgel-reinforced cell-laden gelatin hydrogels. *J Mater Chem B* [Internet]. 2014;2(17):2508-2516. Available from: <https://doi.org/10.1039/C3TB20984A>
- [67] Nayak AK, Alkahtani S, Hasnain MS. Jackfruit Seed Starch-Based Composite Beads for Controlled Drug Release. In: Nayak AK, Alkahtani S, Hasnain MS (eds). *Polymeric and Natural Composites. Advances in Material Research and Technology* [Internet]. Springer Cham; 2022. 213-240p. Available from: https://doi.org/10.1007/978-3-030-70266-3_7
- [68] Xu L, Bai X, Yang J, Li J, et al. Preparation and characterisation of a gellan gum-based hydrogel enabling osteogenesis and inhibiting *Enterococcus faecalis*. *Int J Biol Macromol* [Internet]. 2020;165:2964-2973. Available from: <https://doi.org/10.1016/j.ijbiomac.2020.10.083>
- [69] Pereira DR, Canadas RF, Silva-Correia J, da Silva Morais A, et al. Injectable gellan-gum/hydroxyapatite-based bilayered hydrogel composites for osteochondral tissue regeneration. *Appl Mater Today* [Internet]. 2018;12:309-321. Available from: <https://doi.org/10.1016/j.apmt.2018.06.005>
- [70] Altieri MA, Nicholls CI. Agroecology Scaling Up for Food Sovereignty and Resiliency. Lichtfouse E (eds). *Sustainable Agriculture Reviews* [Internet]. Dordrecht: Springer Dordrecht; 2012. 1-29 p. Available from: <https://doi.org/10.1007/978-94-007-5449-2>
- [71] Ahmed S, Ikram S. *Chitosan: Derivatives, Composites and Applications*. Hoboken: Wiley; 2017. 516p.
- [72] Thomas MS, Koshy RR, Mary SK, Thomas S, et al. Starch, Chitin and Chitosan Based Composites and Nanocomposites [Internet]. Springer Cham; 2019. 57p. Available from: <https://doi.org/10.1007/978-3-030-03158-9>
- [73] Shakir M, Jolly R, Khan AA, Ahmed SS, et al. Resol based chitosan/nano-hydroxyapatite nanoensemble for effective bone tissue engineering. *Carbohydr Polym* [Internet]. 2018;179:317-327. Available from: <http://dx.doi.org/10.1016/j.carbpol.2017.09.103>
- [74] Shen J, Jin B, Qi Y-C, Jiang Q, et al. Carboxylated chitosan/silver-hydroxyapatite hybrid microspheres with improved antibacterial activity and cytocompatibility. *Mater Sci Eng C* [Internet]. 2017;78:589-597. Available from: <http://dx.doi.org/10.1016/j.msec.2017.03.100>
- [75] Costa-Pinto AR, Lemos AL, Tavaría FK, Pintado M. Chitosan and Hydroxyapatite Based Biomaterials to Circumvent Periprosthetic Joint Infections. *Materials* [Internet]. 2021;14(4):804. Available from: <https://doi.org/10.3390/ma14040804>
- [76] Li L, Iqbal J, Zhu Y, Zhang P, et al. Chitosan/Ag-hydroxyapatite nanocomposite beads as a potential adsorbent for the efficient removal of toxic aquatic pollutants. *Int J Biol Macromol* [Internet]. 2018;120:1752-1759. Available from: <https://doi.org/10.1016/j.ijbiomac.2018.09.190>
- [77] Nabipour H, Wang X, Song L, Hu Y. A fully bio-based coating made from alginate, chitosan and hydroxyapatite for protecting flexible polyurethane foam from fire. *Carbohydr Polym* [Internet]. 2020;246:116641. Available from: <https://doi.org/10.1016/j.carbpol.2020.116641>
- [78] Alvarez-Barreto J, Márquez K, Gallardo E, Moret J, et al. Mesenchymal Stem Cell Culture on Composite Hydrogels of Hydroxyapatite Nanoparticles and Photo-Crosslinking Chitosan. *Rev Mex Ing Biom* [Internet]. 2017;38(3):524-536. Available from: <https://doi.org/10.17488/RMIB.38.3.2>
- [79] Trakoolwannachai V, Kheolamai P, Ummartyotin S. Development of hydroxyapatite from eggshell waste and a chitosan-based composite: In vitro behavior of human osteoblast-like cell (Saos-2) cultures. *Int J Biol Macromol* [Internet]. 2019;134:557-564. Available from: <https://doi.org/10.1016/j.ijbiomac.2019.05.004>

- [80] Tripathi A, Saravanan S, Pattnaik S, Moorthi A, et al. Bio-composite scaffolds containing chitosan/nano-hydroxyapatite/nano-copper-zinc for bone tissue engineering. *Int J Biol Macromol* [Internet]. 2012;50(1):294-299. Available from: <http://dx.doi.org/10.1016/j.ijbiomac.2011.11.013>
- [81] Soriente A, Fasolino I, Gomez-Sánchez A, Prokhorov E, et al. Chitosan/hydroxyapatite nanocomposite scaffolds to modulate osteogenic and inflammatory response. *J Biomed Mater Res Part A* [Internet]. 2022;110(2):266-272. Available from: <https://doi.org/10.1002/jbm.a.37283>
- [82] Kaczmarek B, Sionkowska A, Skopinska-Wisniewska J. Influence of glycosaminoglycans on the properties of thin films based on chitosan/collagen blends. *J Mech Behav Biomed Mater* [Internet]. 2018;80:189-193. Available from: <https://doi.org/10.1016/j.jmbbm.2018.02.006>
- [83] Okada T, Nobunaga Y, Konishi T, Yoshioka T, et al. Preparation of chitosan-hydroxyapatite composite mono-fiber using coagulation method and their mechanical properties. *Carbohydr Polym* [Internet]. 2017;175:355-360. Available from: <http://dx.doi.org/10.1016/j.carbpol.2017.07.072>
- [84] Balagangadharan K, Chandran SV, Arumugam B, Saravanan S, et al. Chitosan/nano-hydroxyapatite/nano-zirconium dioxide scaffolds with miR-590-5p for bone regeneration. *Int J Biol Macromol* [Internet]. 2018;111:953-958. Available from: <https://doi.org/10.1016/j.ijbiomac.2018.01.122>
- [85] Chakravarty J, Rabbi MF, Chalivendra V, Ferreira T, et al. Mechanical and biological properties of chitin/poly(lactide (PLA)/hydroxyapatite (HAP) composites cast using ionic liquid solutions. *Int J Biol Macromol* [Internet]. 2020;151:1213-1223. Available from: <https://doi.org/10.1016/j.ijbiomac.2019.10.168>
- [86] Akindoyo JO, Beg MDH, Ghazali S, Heim HP, et al. Effects of surface modification on dispersion, mechanical, thermal and dynamic mechanical properties of injection molded PLA-hydroxyapatite composites. *Compos Part A Appl Sci Manuf* [Internet]. 2017;103:96-105. Available from: <http://dx.doi.org/10.1016/j.compositesa.2017.09.013>
- [87] Grémare A, Guduric V, Bareille R, Heroguez V, et al. Characterization of printed PLA scaffolds for bone tissue engineering. *J Biomed Mater Res Part A* [Internet]. 2018;106(4):887-894. Available from: <https://doi.org/10.1002/jbm.a.36289>
- [88] Akindoyo JO, Beg MDH, Ghazali S, Heim HP, et al. Impact modified PLA-hydroxyapatite composites - Thermo-mechanical properties. *Compos Part A Appl Sci Manuf* [Internet]. 2018;107:326-333. Available from: <https://doi.org/10.1016/j.compositesa.2018.01.017>
- [89] Armentano I, Bitinis N, Fortunati E, Mattioli S, et al. Multifunctional nanostructured PLA materials for packaging and tissue engineering. *Prog Polym Sci* [Internet]. 2013;38(10-11):1720-1747. Available from: <http://dx.doi.org/10.1016/j.progpolymsci.2013.05.010>
- [90] Mohammadi MS, Bureau MN, Nazhat SN. Poly(lactide acid (PLA) biomedical foams for tissue engineering. In: *Netti PA* (eds). *Biomedical Foams for Tissue Engineering Applications* [Internet]. United Kingdom: Elsevier; 2014. 313-334. Available from: <https://doi.org/10.1533/9780857097033.2.313>
- [91] Esposito Corcione C, Gervaso F, Scalerà F, Padmanabhan SK, et al. Highly loaded hydroxyapatite microsphere/ PLA porous scaffolds obtained by fused deposition modelling. *Ceram Int* [Internet]. 2019;45(2):2803-2810. Available from: <https://doi.org/10.1016/j.ceramint.2018.07.297>
- [92] Mondal S, Nguyen TP, Hiệp PV, Hoang G, et al. Hydroxyapatite nano bioceramics optimized 3D printed poly(lactide acid) scaffold for bone tissue engineering application. *Ceram Int* [Internet]. 2020;46(3):3443-3455. Available from: <https://doi.org/10.1016/j.ceramint.2019.10.057>
- [93] Talal A, Waheed N, Al-Masri M, McKay JJ, et al. Absorption and release of protein from hydroxyapatite-poly(lactide acid (HA-PLA) membranes. *J Dent* [Internet]. 2009;37(11):820-826. Available from: <https://doi.org/10.1016/j.jdent.2009.06.014>
- [94] Thanh DTM, Trang PTT, Thom NT, Phuong NT, et al. Effects of Porogen on Structure and Properties of Poly(Lactide Acid)/Hydroxyapatite Nanocomposites (PLA/HAP). *J Nanosci Nanotechnol* [Internet]. 2016;16(9):9450-9459. Available from: <https://doi.org/10.1166/jnn.2016.12032>
- [95] Zhang H, Fu Q-W, Sun T-W, Chen F, et al. Amorphous calcium phosphate, hydroxyapatite and poly(D,L-lactide acid) composite nanofibers: Electrospinning preparation, mineralization and in vivo bone defect repair. *Colloids Surf B* [Internet]. 2015;136:27-36. Available from: <http://dx.doi.org/10.1016/j.colsurfb.2015.08.015>
- [96] Moura NKd, Siqueira IAWB, Machado JPD, Kido HW, et al. Production and Characterization of Porous Polymeric Membranes of PLA/PCL Blends with the Addition of Hydroxyapatite. *J Compos Sci* [Internet]. 2019;3(2):45. Available from: <https://doi.org/10.3390/jcs3020045>
- [97] Zhang J, Wang Q, Wang A. In situ generation of sodium alginate/hydroxyapatite nanocomposite beads as drug-controlled release matrices. *Acta Biomater* [Internet]. 2010;6(2):445-454. Available from: <http://dx.doi.org/10.1016/j.actbio.2009.07.001>
- [98] Sukhodub LF, Sukhodub LB, Litsis O, Prylutskiy Y. Synthesis and characterization of hydroxyapatite-alginate nanostructured composites for the controlled drug release. *Mater Chem Phys* [Internet]. 2018;217:228-234. Available from: <https://doi.org/10.1016/j.matchemphys.2018.06.071>
- [99] Rossi AL, Barreto IC, Maciel WQ, Rosa FP, et al. Ultrastructure of regenerated bone mineral surrounding hydroxyapatite-alginate composite and sintered hydroxyapatite. *Bone* [Internet]. 2012;50(1):301-310. Available from: <http://dx.doi.org/10.1016/j.bone.2011.10.022>
- [100] Rajkumar M, Meenakshisundaram N, Rajendran V. Development of nanocomposites based on hydroxyapatite/sodium alginate: Synthesis and characterisation. *Mater Charact* [Internet]. 2011;62(5):469-479. Available from: <http://dx.doi.org/10.1016/j.matchar.2011.02.008>
- [101] Rajesh R, Ravichandran YD. Development of a new carbon nanotube- alginate-hydroxyapatite tricomponent composite scaffold for application in bone tissue engineering. *Int J Nanomedicine* [Internet]. 2015;10:7-15. Available from: <https://doi.org/10.2147/IJN.S79971>
- [102] Mahmoud EM, Sayed M, El-Kady AM, Elsayed H, et al. In vitro and in vivo study of naturally derived alginate / hydroxyapatite bio composite scaffolds. *Int J Biol Macromol* [Internet]. 2020;165:1346-1360. Available from: <https://doi.org/10.1016/j.ijbiomac.2020.10.014>
- [103] Gholizadeh BS, Buazar F, Hosseini SM, Mousavi SM. Enhanced antibacterial activity, mechanical and physical properties of alginate/hydroxyapatite bionanocomposite film. *Int J Biol Macromol* [Internet]. 2018;116:786-792. Available from: <https://doi.org/10.1016/j.ijbiomac.2018.05.104>

- [104] Bian T, Xing H. A collagen (Col)/nano-hydroxyapatite (nHA) biological composite bone scaffold with double multi-level interface reinforcement. *Arab J Chem* [Internet]. 2022;15(5):103733. Available from: <https://doi.org/10.1016/j.arabjc.2022.103733>
- [105] Bian T, Zhao K, Meng Q, Tang Y, et al. The construction and performance of multi-level hierarchical hydroxyapatite (HA)/collagen composite implant based on biomimetic bone Haversian motif. *Mater Des* [Internet]. 2019;162:60-69. Available from: <https://doi.org/10.1016/j.matdes.2018.11.040>
- [106] Yilmaz E, Çakıroğlu B, Gökçe A, Fındık F, et al. Novel hydroxyapatite/graphene oxide/collagen bioactive composite coating on Ti16Nb alloys by electrodeposition. *Mater Sci Eng C* [Internet]. 2019;101:292-305. Available from: <https://doi.org/10.1016/j.msec.2019.03.078>
- [107] Sun R-X, Lv Y, Niu Y-R, Zhao X-H, et al. Physicochemical and biological properties of bovine-derived porous hydroxyapatite/collagen composite and its hydroxyapatite powders. *Ceram Int* [Internet]. 2017;43(18):16792-16798. Available from: <http://dx.doi.org/10.1016/j.ceramint.2017.09.075>
- [108] Li H, Sun X, Li Y, Wang H, et al. Carbon nanotube-collagen@hydroxyapatite composites with improved mechanical and biological properties fabricated by a multi in situ synthesis process. *Biomed Microdevices* [Internet]. 2020;22:64. Available from: <https://doi.org/10.1007/s10544-020-00520-5>
- [109] Siswanto S, Hikmawati D, Kulsum U, Rudyardjo DI, et al. Biocompatibility and osteoconductivity of scaffold porous composite collagen-hydroxyapatite based coral for bone regeneration. *Open Chem* [Internet]. 2020;18(1):584-590. Available from: <https://doi.org/10.1515/chem-2020-0080>
- [110] Kane RJ, Weiss-Bilka HE, Meagher MJ, Liu Y, et al. Hydroxyapatite reinforced collagen scaffolds with improved architecture and mechanical properties. *Acta Biomater* [Internet]. 2015;17:16-25. Available from: <http://dx.doi.org/10.1016/j.actbio.2015.01.031>
- [111] Sionkowska A, Kozłowska J. Properties and modification of porous 3-D collagen/hydroxyapatite composites. *Int J Biol Macromol* [Internet]. 2013;52(1):250-259. Available from: <http://dx.doi.org/10.1016/j.ijbiomac.2012.10.002>
- [112] Zvicer J, Medic A, Veljovic D, Jevtic S, et al. Biomimetic characterization reveals enhancement of hydroxyapatite formation by fluid flow in gellan gum and bioactive glass composite scaffolds. *Polym Test* [Internet]. 2019;76:464-472. Available from: <https://doi.org/10.1016/j.polymertesting.2019.04.004>
- [113] Bastos AR, Raquel Maia F, Miguel Oliveira J, Reis RL, et al. Influence of gellan gum-hydroxyapatite spongy-like hydrogels on human osteoblasts under long-term osteogenic differentiation conditions. *Mater Sci Eng C* [Internet]. 2021;129:112413. Available from: <https://doi.org/10.1016/j.msec.2021.112413>
- [114] Anandan D, Madhumathi G, Nambiraj NA, Jaiswal AK. Gum based 3D composite scaffolds for bone tissue engineering applications. *Carbohydr Polym* [Internet]. 2019;214:62-70. Available from: <https://doi.org/10.1016/j.carbpol.2019.03.020>
- [115] Jamshidi P, Chouhan G, Williams RL, Cox SC, et al. Modification of gellan gum with nanocrystalline hydroxyapatite facilitates cell expansion and spontaneous osteogenesis. *Biotechnol Bioeng* [Internet]. 2016;113(7):1568-1576. Available from: <https://doi.org/10.1002/bit.25915>
- [116] Manda MG, da Silva LP, Cerqueira MT, Pereira DR, et al. Gellan gum-hydroxyapatite composite spongy-like hydrogels for bone tissue engineering. *J Biomed Mater Res Part A* [Internet]. 2018;106(2):479-490. Available from: <https://doi.org/10.1002/jbm.a.36248>
- [117] dos Santos MVB, Bastos Nogueira Rocha L, Gomes Vieira E, Leite Oliveira A, et al. Development of Composite Scaffolds Based on Cerium Doped-Hydroxyapatite and Natural Gums—Biological and Mechanical Properties. *Materials* [Internet]. 2019;12(15):2389. Available from: <https://doi.org/10.3390/ma12152389>
- [118] Heidari F, Razavi M, E.Bahrololoom M, Bazargan-Lari R, et al. Mechanical properties of natural chitosan/hydroxyapatite/magnetite nanocomposites for tissue engineering applications. *Mater Sci Eng C* [Internet]. 2016;65:338-344. Available from: <http://dx.doi.org/10.1016/j.msec.2016.04.039>
- [119] Shavandi A, Bekhit AE-DA, Ali MA, Sun Z, et al. Development and characterization of hydroxyapatite/ β -TCP/chitosan composites for tissue engineering applications. *Mater Sci Eng C* [Internet]. 2015;56:481-493. Available from: <http://dx.doi.org/10.1016/j.msec.2015.07.004>
- [120] Ghosh S, Ghosh S, Pramanik N. Bio-evaluation of doxorubicin (DOX)-incorporated hydroxyapatite (HAp)-chitosan (CS) nanocomposite triggered on osteosarcoma cells. *Adv Compos Hybrid Mater* [Internet]. 2020;3(3):303-314. Available from: <https://doi.org/10.1007/s42114-020-00154-4>
- [121] Gritsch L, Maqbool M, Mouriño V, Ciraldo FE, et al. Chitosan/hydroxyapatite composite bone tissue engineering scaffolds with dual and decoupled therapeutic ion delivery: copper and strontium. *J Mater Chem B* [Internet]. 2019;7(40):6109-6124. Available from: <https://doi.org/10.1039/C9TB00897G>
- [122] Chen L, Hu J, Shen X, Tong H. Synthesis and characterization of chitosan-multiwalled carbon nanotubes/hydroxyapatite nanocomposites for bone tissue engineering. *J Mater Sci: Mater Med* [Internet]. 2013;24(8):1843-1851. Available from: <https://doi.org/10.1007/s10856-013-4954-x>
- [123] Li X, Nan K, Shi S, Chen H. Preparation and characterization of nano-hydroxyapatite/chitosan cross-linking composite membrane intended for tissue engineering. *Int J Biol Macromol* [Internet]. 2012;50(1):43-49. Available from: <http://dx.doi.org/10.1016/j.ijbiomac.2011.09.021>
- [124] Saravanan S, Nethala S, Pattnaik S, Tripathi A, et al. Preparation, characterization and antimicrobial activity of a bio-composite scaffold containing chitosan/nano-hydroxyapatite/nano-silver for bone tissue engineering. *Int J Biol Macromol* [Internet]. 2011;49(2):188-193. Available from: <http://dx.doi.org/10.1016/j.ijbiomac.2011.04.010>
- [125] Zhang J, Nie J, Zhang Q, Li Y, et al. Preparation and characterization of bionic bone structure chitosan/hydroxyapatite scaffold for bone tissue engineering. *J Biomater Sci Polym Ed* [Internet]. 2014;25(1):61-74. Available from: <https://doi.org/10.1080/09205063.2013.836950>
- [126] Carfi Pavia F, Conoscenti G, Greco S, La Carrubba V, et al. Preparation, characterization and in vitro test of composites poly-lactic acid/hydroxyapatite scaffolds for bone tissue engineering. *Int J Biol Macromol* [Internet]. 2018;119:945-953. Available from: <https://doi.org/10.1016/j.ijbiomac.2018.08.007>






- [127] Ma B, Han J, Zhang S, Liu F, et al. Hydroxyapatite nanobelt/poly(lactic acid) Janus membrane with osteoinduction/barrier dual functions for precise bone defect repair. *Acta Biomater* [Internet]. 2018;71:108-117. Available from: <https://doi.org/10.1016/j.actbio.2018.02.033>
- [128] Anita Lett J, Sagadevan S, Paiman S, Mohammad F, et al. Exploring the thumbprints of Ag-hydroxyapatite composite as a surface coating bone material for the implants. *J Mater Res Technol* [Internet]. 2020;9(6):12824-12833. Available from: <https://doi.org/10.1016/j.jmrt.2020.09.037>
- [129] Chuan D, Fan R, Wang Y, Ren Y, et al. Stereocomplex poly(lactic acid)-based composite nanofiber membranes with highly dispersed hydroxyapatite for potential bone tissue engineering. *Compos Sci Technol* [Internet]. 2020;192:108107. Available from: <https://doi.org/10.1016/j.compscitech.2020.108107>
- [130] Zare RN, Doustkhah E, Assadi MHN. Three-dimensional bone printing using hydroxyapatite-PLA composite. *Mater Today Proc* [Internet]. 2021;42(3):1531-1533. Available from: <https://doi.org/10.1016/j.matpr.2019.12.046>
- [131] Alksne M, Kalvaityte M, Simoliunas E, Rinkunaite I, et al. In vitro comparison of 3D printed poly(lactic acid)/hydroxyapatite and poly(lactic acid)/bioglass composite scaffolds: Insights into materials for bone regeneration. *J Mech Behav Biomed Mater* [Internet]. 2020;104:103641. Available from: <https://doi.org/10.1016/j.jmbbm.2020.103641>
- [132] Zhang H, Mao X, Zhao D, Jiang W, et al. Three dimensional printed poly(lactic acid)-hydroxyapatite composite scaffolds for prefabricating vascularized tissue engineered bone: An in vivo bioreactor model. *Sci Rep* [Internet]. 2017;7(1):15255. Available from: <http://dx.doi.org/10.1038/s41598-017-14923-7>

dx.doi.org/10.17488/RMIB.43.2.2

E-LOCATION ID: 1238

Studying the Effect of Temperature on the Tensile Strength of an Intravascular Catheter Using a Degradation Model

Estudiando el Efecto de la Temperatura en la Resistencia Tensil de un Catéter Intravascular Usando un Modelo de Degradación

Kimberly Esqueda Hernández , Luis Alberto Rodríguez-Picón  , Luis Carlos Méndez-González ,
Roberto Romero-López 

Universidad Autónoma de Ciudad Juárez

ABSTRACT

The accelerated aging process is incorporated into the design and development of intravascular catheters to assess their reliability assuring that this medical device is safe and effective for the intended use during their shelf life. The accelerated aging process is based on a common approach that assumes that the rate of aging increases by a factor of $2^{(\Delta T/10)}$, where ΔT is the temperature increment. However, with the life data obtained from this empirical method is difficult to do inferences about reliability. This paper presents an accelerated destructive degradation test using thermal stress to obtain degradation data directly relates reliability to critical performance characteristic, which is the tensile strength in the intravascular catheter tip considered as a critical concern in patients' safety. The degradation data model is given by a stochastic Wiener process with the drift parameter being represented as Arrhenius function. The parameters of the Wiener process and Arrhenius function are estimated using maximum likelihood; these parameters are used to estimate the first-passage time (time to failure) distribution when the intravascular catheters degradation path reaches a tensile strength critical value in each thermal stress level. Based on this, a complete product reliability assessment is performed and presented.

KEYWORDS: Accelerated aging, degradation, first passage time, intravascular catheter, Wiener process

RESUMEN

El proceso de envejecimiento acelerado es incorporado en el diseño y desarrollo de catéteres intravasculares para evaluar su confiabilidad y asegurar que el dispositivo médico es seguro y efectivo para su uso durante su vida de estante. Este proceso está basado en un enfoque que asume que la tasa de envejecimiento se incrementa por un factor de $2^{(\Delta T/10)}$, en donde ΔT es el incremento de temperatura. Sin embargo, con los datos de vida obtenidos de este método empírico resulta complicado realizar inferencias sobre la confiabilidad del dispositivo. Este artículo presenta una prueba de degradación acelerada destructiva que considera un estrés termal para obtener datos de degradación que se relaciona directamente la confiabilidad con la resistencia tensil de la punta de un catéter intravascular y que es considerada como una característica crítica para la seguridad de los pacientes. El modelo de degradación está dado por un proceso estocástico Wiener, con el parámetro de deriva representado la relación de Arrhenius. Los parámetros del proceso Wiener y la relación de Arrhenius son estimados mediante máxima verosimilitud; estos parámetros son usados para estimar la distribución de primer paso, la cual se caracteriza cuando la resistencia de un catéter alcanza el nivel crítico de resistencia en cada nivel de estrés. Considerando esto, se lleva a cabo y se presenta una evaluación de confiabilidad completa del producto.

PALABRAS CLAVE: Envejecimiento acelerado, degradación, Tiempo de primer paso, Catéter intravascular, Proceso Wiener

Corresponding author

TO: Luis Alberto Rodríguez-Picón
INSTITUTION: Universidad Autónoma de Ciudad Juárez
ADDRESS: Av. del Charro #450 Norte,
Col. Partido Romero, C. P. 32310, Ciudad Juárez,
Chihuahua, México
CORREO ELECTRÓNICO: luis.picon@uacj.mx

Received:

24 January 2022

Accepted:

28 April 2022

INTRODUCTION

Elevated temperature is frequently used as a factor to stimulate the aging process, also known as “accelerated aging”. This process is applied to different polymers that are used in the fabrication of medical devices and other materials applications from nuclear, space, and geomembrane industries ^{[1][2]}.

The objective of the accelerated aging process in the medical device industry is reducing the amount of time required for performance qualification of medical devices including their shelf life. The concept of shelf life must be incorporated into the product reliability during the process of medical device development for commercial distribution ^{[1][3]}.

The introduction of medical devices in the market requires to assure that they can be stored for an extended period in accordance with their labeling, without any decrease in the performance that may affect safety and efficacy when the device is used ^{[3][4]}. The accelerated aging process provides experimental data in support of the performance and shelf life until real-time aged samples become available ^[4].

The accelerated aging techniques used in the medical device industry are well documented by Standards Development Organizations (SDO), such as Advancement of Medical Instrumentation (AAMI) in the Technical Information Report TIR17, entitled “Radiation Sterilization Material Qualification”, and American Society for Testing and Materials (ASTM) in their standard F1980-7. Both SDO provide a method based on van’t Hoff’s observation and Arrhenius reaction rate function. This function, known as accelerated aging factor (AAF), states that a 10°C increase or decrease in temperature, the rate of chemical reactions increases by a factor of two. It can be expressed as in Equation (1).

$$AAF = Q_{10}^{\Delta T/10} \quad (1)$$

Where, $\Delta T = T - T_{ref}$ is a reference temperature that determines the effect of aging, and T is an accelerated temperature used to stimulate the effect of aging. This is also known as the $Q_{10} = 2$ rule ^{[1][5]}. This mathematical expression is a predictive equation from empirical observation that is considered into the approaches to accelerated aging methods. There are many approaches to accelerated aging that have been documented and summarized in the literature, from simple holding the materials at conditions as close as possible to the use conditions to minimize the aging factor, up to complex chemical and analytical methods ^[2]. Different studies of elastomer aging and their application to biomaterials have been reviewed by Hukins *et al.* ^[1]. Additionally, accelerated aging testing using the Arrhenius model with elevated temperatures has been studied to determine the failure modes of LEDs for medical applications ^[6].

Even though it has been demonstrated that the empirical method of $Q_{10} = 2$ rule outlined in AMMI TIR17 and ASTM F1980-7 is reasonable and responsible, it is only valid for $T \leq 60$ °C ^{[1][2]}. In this condition it is difficult to obtain life data and have inferences about medical device reliability; therefore, critical concern in patients’ safety is not considered. Reliability analysis using accelerated degradation tests (ADTs) can often acquire a better accuracy of life estimation in comparison to accelerated life tests (ALTs) e.g., accelerated aging. Since, using accelerated degradation data directly relates reliability to a physical characteristic also known as critical performance characteristic ^{[7][8]}. Furthermore, an accelerated degradation-based model characterizes the degradation process as a function of time. A typical degradation model is given by a stochastic process ^[9]. Degradation models based on stochastic processes have been particularly studied in the last years ^[10]. The different stochastic processes including the Wiener Process are described by Lim and Yum ^[9], Rodríguez-Picón *et al.* ^[10] and Rodríguez-Picón *et al.* ^[11].

The Wiener process is a non-monotone stochastic process, which suggests that negative increments may be present in the process. This process has been widely used in the reliability analysis of different applications^[12]. For example, Pan *et al.*^[7] validated a life estimation method using degradation dataset of the LED and the Wiener degradation process. Li *et al.*^[13] used a Wiener process model to predict the remaining useful life (RUL) in two study cases, the first in gyroscopes used as critical component of the inertial navigation system (INS) and the second in the lithium-ion batteries, which are used as the energy solutions in many fields. Lyu *et al.*^[14] applied the Wiener process to model the degradation-based in burn-in method to maximizing the mean lifetime to failure (MTTF) of a certain product.

On the other hand, in certain applications of ADTs, the measurements of the degradation level in the critical performance characteristic are destructive, so that only one measurement can be obtained from each test unit; this approach is based on accelerated destructive degradation tests (ADDT)^[15] and some examples of the ADDTs applications have described below. Escobar *et al.*^[15] applied an ADDT for assessing reliability using the strength of an adhesive bond. The considered test was destructive because the strength can only be measured once for each unit. Chih-Chun Tsai *et al.*^[16] used an ADDT to assess the long-term reliability of a polymer material that was subjected to an alkaline environment at high temperatures; the critical performance characteristic was the tensile strength so that was destructive. Some studies have been conducted on ADDT planning; as described in^[17]^[18].

Driven by the above-mentioned works, the objective of this paper is to develop a ADDT model based on the Wiener process as an alternative approach to the accelerated aging method outlined in AAMI TIR17 and ASTM F 1980-7 that are used in the design and development of medical devices specifically intravascular

catheters to provide evidence for claimed shelf life as part of the product reliability. An intravascular catheter is a medical device that is described in Food and Drug Administration (FDA) regulation, 21 Code of Federal Regulations (CFR) part 880.5200 as a slender tube that is inserted into the patient's vascular system for short term use to sample blood, monitor blood pressure, or administer fluids intravenously^[19]. For the ADDT performed in this paper, the critical performance characteristic selected is the tensile strength in the catheter tip (tip pull test). This test assesses the bond strength of polymeric thermal fusion between the distal tip and the catheter shaft to demonstrate that bond can withstand tensile forces greater than those that may be experienced during clinical use. The tensile force that separates the distal tip from the catheter shaft is a critical concern patients' safety because a failure of bonds in the distal tip could lead to vessel damage, embolic risk (obstruction of blood flow) due to the device remnants within the vasculature, and their death, which may also potentially occur^[20]^[21]^[22]. There are numerous adverse events and recalls reported on the medical device databases from FDA related with the distal tip separation. This information can be found in^[23]^[24].

The contents of this paper are organized as follows: Section 2 describes the devices under test (DUT), and the ADDT design with the stress condition that is applied to the DUT over time. Section 3 explains the theory and modeling principle of the degradation model in terms of stress level, and the parameter estimation method. The theory of times to failure and the accelerated factor calculation are explained as well. Section 4 provides the results of the degradation model, and their estimated parameters which are obtained from the ADDT described in section 2. The degradation model parameters are used to calculate the estimated time to failure in the DUT, and an estimated acceleration factor. We concluded this paper in Section 5.

MATERIALS AND METHODS

In this section, a description of the DUT is presented. A description of the experimental conditions and obtained results is also presented.

Test Samples

The DUT are intravascular catheters over the wire (OTW) single-lumen with atraumatic distal tip designed for use in the peripheral vascular system. The Intravascular catheter consists of a lubricious inner liner, a stainless-steel braid over the liner, and a shaft (outer layer) that involve different polymers. The shaft is bon-ded with a polymeric distal tip trough out a thermal fusion method. Additionally, a radiopaque marker band is positioned on the distal

tip, and a hub is attached to the proximal end of the intravascular catheter. The distal tip is made from a polymer with low stiffness in comparison to the catheter shaft polymers. For the distal tip, low stiffness is required to passage through curved pathways in the vasculature in an easy and non-traumatic manner while the catheter shaft requires greater stiffness to achieve precise transmission of the movement carry on by the physician's hand up to the tip of the device. This mechanical property is required to successfully navigate the vascular system [25]. The DUT have an outer diameter of 6 French size or 1.92 mm, an inner diameter of 1.58 mm, and they are available in a variety of lengths. An illustration of the DUT is presented in Figure 1.

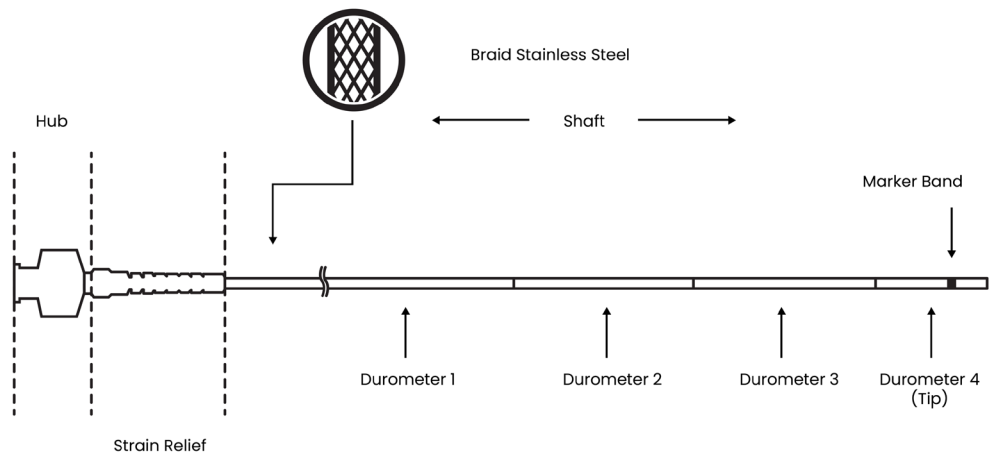


FIGURE 1. Illustration of the DUT.

Experimental Setup and Test Conditions

The DUT claim a shelf life of two years when they are stored in temperature-room conditions (from 20 °C up to 25 °C). Thus, the ADDT was based on thermal stress to obtain the tensile strength degradation data. The thermal stress was conducted in calibrated ovens with a constant aging temperature of 50 °C, 60 °C, 70 °C and 80 °C. The temperatures were defined with increments of 10 °C to adhere to SDOs, such as the test schemes defined in ASTM F 1980-7 and AAMI TIR17. The first accelerated temperature was defined as 50 °C to increase the aging rate, which would be less if the

initial temperature was set at a lower value. Furthermore, maximum test temperature is suggested to be 60 °C [2] if the aging test is based on the van't Hoff's observation, as non-linear effects may be expected in the polymeric systems. Based on this, it is considered to extend the temperature beyond 60 °C to two more increments as 70 °C and 80 °C, in the aims of explore this non-linearity of the temperature effect. It should be noted that test temperatures below 60 °C are recommended given that the van't Hoff's observation gives an empirical estimation that tends to be linear across the temperature ratios in (1).

There were six tensile strength measurements obtained from the DUTs from 15 days up to 75 days (15, 30, ..., 75) at the four different levels of temperature. In addition, the experiment included 6 units that were not subjected to the thermal stress at the beginning of the experiment. In total, 144 units were subjected to the thermal stress conditions and tested according to the time schedule. Figure 2 represents a schematic of the experimental set-up.

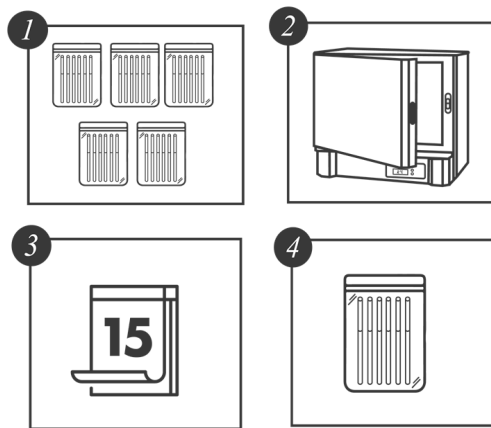


FIGURE 2. Accelerated Degradation Destructive Test Experimental Set-up. Five groups of six catheters each (1) per temperature were placed in the oven (2). Every 15 days, a group was withdrawn (3 and 4) and tested.

The tensile strength testing was performed according to the methodology described on Annex B of the ISO 10555-1:2013. This standard specifies the general requirements for intravascular catheters. Annex B describes the method for determining peak tensile force. Table 1 was used to select the test conditions; for a gauge length of the test piece of 10 mm, a test speed of 200 mm/min is obligatory. Using a calibrated Chatillon force measurement system, the tensile force was applied to the catheter shaft and distal tip bond until the test piece separates into two or more pieces. The peak tensile force in N reached by the tensile testing of the DUT was recorded. Prior to performing the tensile strength test, the DUT were conditioned in an aqueous medium at 37 °C ± 2 °C for a period of 2 hours, which represents the expected clinical conditions for

TABLE 1. Accelerated degradation test plan.

Temperature (°C)	Days						
	0	15	30	45	60	75	
--	24	0	0	0	0	0	24
50	0	6	6	6	6	6	30
60	0	6	6	6	6	6	30
70	0	6	6	6	6	6	30
80	0	6	6	6	6	6	30
Totals	24	24	24	24	24	24	144

the devices. Immediately after conditioning the tensile strength test were performed [26]. Figure 3 represents the test conditions.

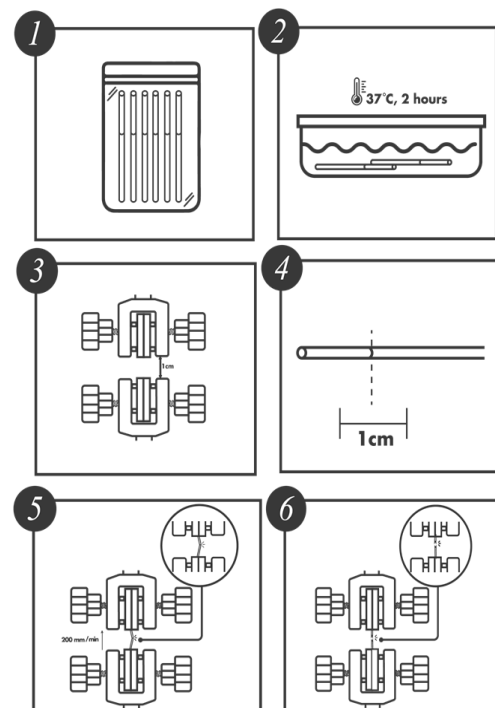


FIGURE 3. Accelerated Degradation Destructive Test Conditions. A group of catheters (1) is taken and conditioning in an aqueous medium at 37 °C ± 2 °C for a period of 2 hours (2) to reflect the expected clinical conditions. A gauge length in the Chatillon and test piece is measurement at 10 mm (3 and 4). The test piece is placed between the Chatillon's clamps and a test speed of 200 mm/min is programmed. The upper clamp is raising (5) until the test piece separates into two or more pieces (6).

Test Results

The degradation data obtained from the tensile strength tests are shown from Fig. 3 to Fig.6 for the thermal stress levels of 50 °C, 60 °C, 70 °C, and 80 °C respectively. From these figures, it can be observed that the tensile strength increases and decreases over time. For this reason, we adopt a Wiener process to character-

ize the degradation evolution of the DUT. Furthermore, it can be noted that in all temperature levels a set of six catheters were tested to measure their tensile strength with no accelerated aging, i.e., these catheters were tested at a room temperature condition of 23 °C. It can be noted that at room temperature, the tensile strength is between 60 and 80 N in all temperature levels. This

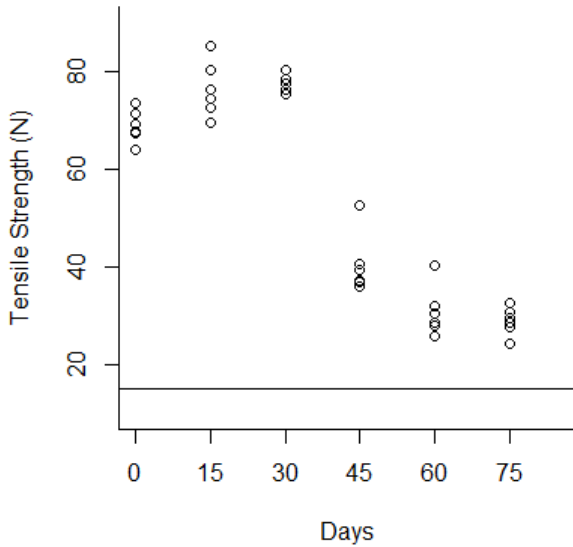


FIGURE 4. Behavior of the tensile strength degradation at 50 °C. The horizontal line at 15 N is the degradation critical level.

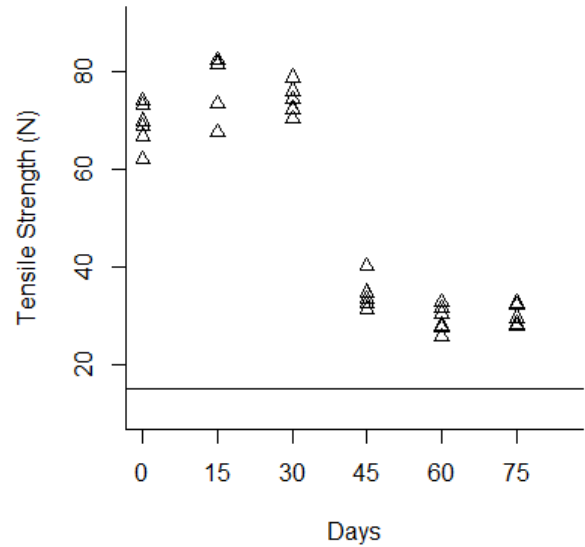


FIGURE 5. Behavior of the tensile strength degradation at 60 °C. The horizontal line at 15 N is the degradation critical level.

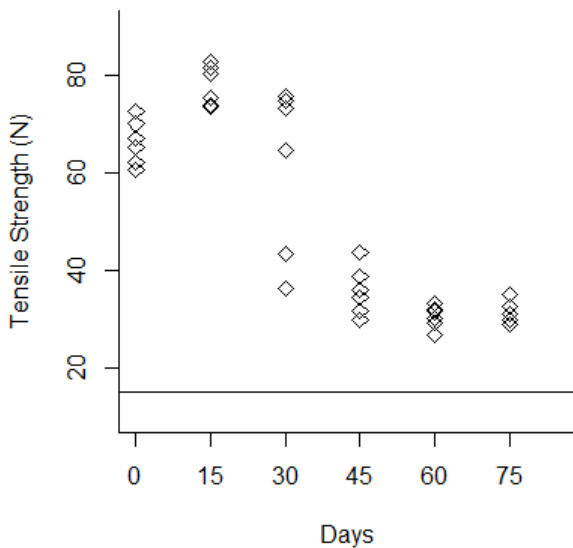


FIGURE 6. Behavior of the tensile strength degradation at 70 °C. The horizontal line at 15 N is the degradation critical level.

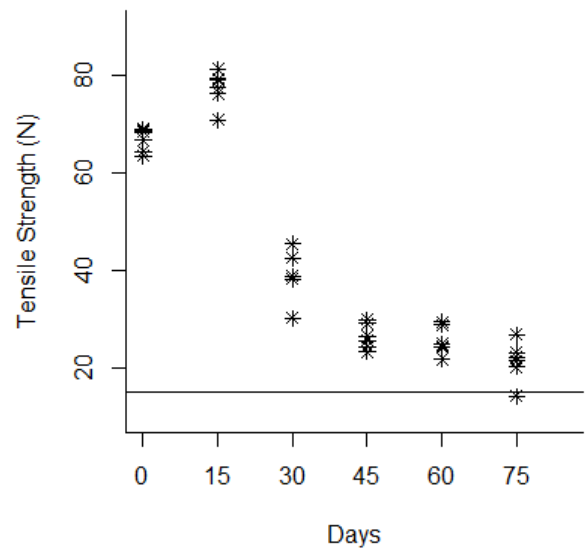


FIGURE 7. Behavior of the tensile strength degradation at 80 °C. The horizontal line at 15 N is the degradation critical level.

variation is expected according to the specifications of the product. Moreover, in all temperature levels, it can be noted that the higher tensile strength is observed at 15 days of temperature aging. Then, from day 30 to day 75, the tensile strength diminishes, as may be expected given the high temperature exposure. Specifically in day 30, it can be noted that at 50 °C the six DUT are overlapped at a tensile strength of 80 N approximately. However, from temperature 60 °C to 80 °C it can be noted that the strengths of the six DUT are more disperse and tend to be lower, this indeed is also due to effect of the higher temperature levels. Similar behaviors can be noted at days 45 and 60, where the tensile strength tends to be lower as the temperature increases. It should be noted that the distal tip is a polymer that is bonded to the catheter shaft through thermal fusion. Although, it is clear that the temperature affects the strength of the polymer bond, it appears that the tensile strength increases at 15 days of temperature exposure in all temperature levels, this may be due to the effect of the temperature on the polymeric bond.

According to ISO 10555-1: 2013, a failure occurs when the tensile strength of the DUT reaches a critical level below 15 N [26]. Another difference of behaviors can be noted based on this critical level. Specifically at 75 days of exposure, it can be noted that from temperatures 50 °C to 70 °C none of the six DUT tensile strengths approaches to the critical level. However, the tensile strength for one DUT for the temperature level of 80 °C is below the critical level of 15 N, and the tensile strengths for the rest of the devices are close to this critical level.

Theory and Modeling

In this section, the used methodology in this study is described as the Wiener process with the drift parameter being considered as a function of the thermal stress level, in this case, the Arrhenius function, along with the parameter estimation method using maximum likelihood (MLE). In addition, the degradation

model formulation allows performing the estimated times to failure and an accelerated aging factor in each thermal stress level.

Wiener Process and Arrhenius Relationship

The appropriate model for non-monotone degradation process as can be noted in Figures 3 to 6, is a Wiener process, which is defined as in Equation (2).

$$X(t) = \alpha t + \sigma B(t) \quad (2)$$

Where α is a drift parameter, the parameter σ is known as the diffusion, and $B(t)$ is the Standard Wiener process. It is well known that the drift parameter α describes the rate of the degradation process. In this paper, it is represented as a function of the thermal stress level, the diffusion parameter σ represents the common degradation characteristics to all units in a population [7]. Thus, if an ADDT is considered the degradation measurements $X_{ik}(t_j)$ of i th unit $i, i= 1, \dots, n$ at the corresponding time $t_j, j= 1, \dots, m$ for thermal stress level $k, k= 1, \dots, r$ are obtained. Per the independent increment property of the Wiener process, then $\Delta X_{ik}(t_j) = X_{ik}(t_j) - X_{ik}(t_{j-1})$ are normally distributed $\Delta X_{ik}(t_j) \sim f(\alpha \Delta t_{ijk}, \sigma \sqrt{\Delta t_{ijk}})$, thus the probability density function (PDF) $f(\alpha \Delta t_{ijk}, \sigma \sqrt{\Delta t_{ijk}})$ has the form as in Equation (3).

$$f_x(\Delta X_{ik}(t_j)) = \frac{1}{\sqrt{2\pi\sigma^2\Delta t_{ijk}}} e^{-\frac{(\Delta X_{ik}(t_j) - \alpha \Delta t_{ijk})^2}{2\sigma^2\Delta t_{ijk}}} \quad (3)$$

In Equation (3) α is the Arrhenius function given that ADDT uses a thermal stress. Arrhenius function is described as in Equation (4).

$$k = A \exp\left(-\frac{Ea}{RT}\right) \quad (4)$$

Where k is the reaction rate constant; A is frequency factor (a constant to be estimated); Ea is the Energy of activation (KJ/mol); R is ideal gas constant (8.314 KJ/mol); and T is reaction temperature (°K). So that, (4) can be denoted as in Equation (5).

$$\alpha(T_k) = \beta_1 \exp\left(-\frac{\beta_2}{T_k}\right) \quad (5)$$

Where $A = \beta_1$, and $Ea/R = \beta_2$, for each thermal stress level T_k .

Parameters Estimation

For the PDF of the Wiener process in (3), there is a set of parameters denoted as $\theta = (\beta_1, \beta_2, \sigma)$ that need to be estimated. MLE was the parameter estimation method selected to obtain the model parameters in terms of the available degradation data.

Based on Equation (3), then the log-likelihood function for n test units, m measurements, and k stress levels can be denoted as in Equation (6).

$$\ln L(\hat{\sigma}, \hat{\beta}_1, \hat{\beta}_2) = \sum_{k=1}^r \sum_{i=1}^n \sum_{j=1}^m \left[-\frac{1}{2} \ln(2\pi \Delta t_{ijk}) - \ln \sigma - \frac{(\Delta X(t_{ijk}) - \beta_1 \exp(-\frac{\beta_2}{T_k}) \Delta t_{ijk})^2}{2 \sigma^2 \Delta t_{ijk}} \right] \quad (6)$$

The first partial derivatives of Equation (6) with respect to the unknown parameters θ are given in Equations (7), (8), and (9) for β_1, β_2, σ respectively.

$$\frac{\partial \ln L(\hat{\sigma}, \hat{\beta}_1, \hat{\beta}_2)}{\partial \hat{\beta}_1} = \sum_{k=1}^r \sum_{i=1}^n \sum_{j=1}^m \left[\frac{\left\{ \Delta X(t_{ijk}) - \beta_1 \exp\left(-\frac{\beta_2}{T_k}\right) \Delta t_{ijk} \right\} \left(\exp\left(-\frac{\beta_2}{T_k}\right) \right)}{\sigma^2} \right] \quad (7)$$

$$\frac{\partial \ln L(\hat{\sigma}, \hat{\beta}_1, \hat{\beta}_2)}{\partial \hat{\beta}_2} = \sum_{k=1}^r \sum_{i=1}^n \sum_{j=1}^m \left[\frac{\left\{ \Delta X(t_{ijk}) - \beta_1 \exp\left(-\frac{\beta_2}{T_k}\right) \Delta t_{ijk} \right\} \left(\frac{\beta_1}{T_k} \exp\left(-\frac{\beta_2}{T_k}\right) \right)}{\sigma^2} \right] \quad (8)$$

$$\frac{\partial \log L(\hat{\sigma}, \hat{\beta}_1, \hat{\beta}_2)}{\partial \hat{\sigma}} = \sum_{k=1}^r \sum_{i=1}^n \sum_{j=1}^m \left[-\frac{1}{\sigma} + \frac{\left(\Delta X(t_{ijk}) - \beta_1 \exp\left(-\frac{\beta_2}{T_k}\right) \Delta t_{ijk} \right)^2}{\sigma^3 \Delta t_{ijk}} \right] \quad (9)$$

Then, the MLE of θ can be obtained by solving and maximizing the equations presented in Equations (7), (8), and (9). However, this calculation requires an iterative procedure, in this paper we considered the Newton-Raphson method, so that the Hessian or matrix of second partial derivatives of the log-likelihood function in Equation (6) is required. Let H denote the Hessian which is described in (10).

$$H(\theta) = \begin{bmatrix} \frac{\partial^2 \ln L}{\partial \beta_1^2} & \frac{\partial^2 \ln L}{\partial \beta_1 \partial \beta_2} & \frac{\partial^2 \ln L}{\partial \beta_1 \partial \sigma} \\ \frac{\partial^2 \ln L}{\partial \beta_1 \partial \beta_2} & \frac{\partial^2 \ln L}{\partial \beta_2^2} & \frac{\partial^2 \ln L}{\partial \beta_2 \partial \sigma} \\ \frac{\partial^2 \ln L}{\partial \beta_1 \partial \sigma} & \frac{\partial^2 \ln L}{\partial \beta_2 \partial \sigma} & \frac{\partial^2 \ln L}{\partial \sigma^2} \end{bmatrix} \quad (10)$$

The second partial derivatives of Equation (6) with respect to the unknown parameters that conform the Hessian in (10) are given in Equations (11), (12), (13), (14), (15), and (16) for $\beta_1, \beta_2, \sigma, \beta_1 \beta_2, \beta_1 \sigma, \beta_2 \sigma$ respectively.

$$\frac{\partial^2 l(\sigma, \beta_1, \beta_2)}{\partial \beta_1^2} = \sum_{k=1}^r \sum_{i=1}^n \sum_{j=1}^m \left\{ \frac{-\exp\left(-\frac{2\beta_2}{T_k}\right) \Delta t_{ijk}}{\sigma^2} \right\} \quad (11)$$

$$\frac{\partial^2 l(\sigma, \beta_1, \beta_2)}{\partial \beta_2^2} = -\sum_{k=1}^r \sum_{i=1}^n \sum_{j=1}^m \left\{ \frac{-\left(\frac{\Delta X_{ijk} \beta_1}{T_k^2}\right) \exp\left(-\frac{\beta_2}{T_k}\right) + \left(\frac{2\Delta t_{ijk} \beta_1^2}{T_k^2}\right) \exp\left(-\frac{2\beta_2}{T_k}\right)}{\sigma^2} \right\} \quad (12)$$

$$\frac{\partial^2 l(\sigma, \beta_1, \beta_2)}{\partial \sigma^2} = \sum_{k=1}^r \sum_{i=1}^n \sum_{j=1}^m \frac{1}{\sigma^2} - \frac{3 \left\{ \Delta X_{ijk} - \beta_1 \exp\left(-\frac{\beta_2}{T_k}\right) \Delta t_{ijk} \right\}^2}{\sigma^4 \Delta t_{ijk}} \quad (13)$$

$$\frac{\partial^2 l(\sigma, \beta_1, \beta_2)}{\partial \beta_1 \partial \beta_2} = \sum_{k=1}^r \sum_{i=1}^n \sum_{j=1}^m \left\{ -\frac{\Delta X_{ijk}}{T_k} \exp\left(-\frac{\beta_2}{T_k}\right) + \frac{2\beta_1 \Delta t_{ijk}}{T_k} \exp\left(-\frac{2\beta_2}{T_k}\right) \right\} \quad (14)$$

$$\frac{\partial^2 l(\sigma, \beta_1, \beta_2)}{\partial \beta_1 \partial \sigma} = -2 \sum_{k=1}^r \sum_{i=1}^n \sum_{j=1}^m \left\{ \frac{\Delta X_{ijk} \exp\left(-\frac{\beta_2}{T_k}\right) - \beta_1 \Delta t_{ijk} \exp\left(-\frac{2\beta_2}{T_k}\right)}{\sigma^3} \right\} \quad (15)$$

$$2 \frac{\frac{\partial^2 l(\sigma, \beta_1, \beta_2)}{\partial \beta_2 \partial \sigma}}{\sigma^3} = \frac{\left\{ \left(\frac{\Delta X_{ijk} \beta_1}{T_k} \right) \exp\left(-\frac{\beta_2}{T_k}\right) - \left(\frac{\Delta t_{ijk} \beta_1^2}{T_k} \right) \exp\left(-\frac{2\beta_2}{T_k}\right) \right\}}{\sigma^3} \quad (16)$$

First-Passage Time (Time to Failure)

The failure of the DUT will occur if the degradation trajectory given for the tensile strength reaches certain critical degradation level, namely, when the tensile force is below of 15 N according to ISO 10555-1: 2013. For this given critical level indicated as ω , the lifetime T_ω of the DUT is then defined as the first instant at which the trajectory $X(t)_{t \geq 0}$ exceeds the level $\omega = 15 \text{ N}$ [26] [27]. On the other hand, as the degradation process is described by a Wiener process as in Equation (3), then the first-passage time T_ω follows an Inverse Gaussian distribution $T_\omega \sim f(t_\omega | \mu = \omega/\hat{\alpha}_k, \lambda = \omega^2/\sigma^2)$ with cumulative distribution function (CDF) described as $F(t_\omega) = 1 - R(t_\omega)$, where $R(t_\omega)$ is defined in Equation (17).

$$1 - \Phi \left[\sqrt{\frac{1}{\sigma_t^2}} (\alpha t - \omega) \right] + \exp \left\{ \frac{2\alpha\omega}{\sigma^2} \right\} \times \Phi \left[-\sqrt{\frac{1}{\sigma_t^2}} (\alpha t + \omega) \right] \quad (17)$$

Acceleration Factor

The acceleration factor is a calculated ratio of time to achieve the same level of physical property change at a stress accelerated and the use level condition (ASTM F1980, 2016). The acceleration factor denoted as L between a use level and a greater level of stress can be described as in Equation (18).

$$L = \frac{L_{use}}{L_{Accelerated}} \quad (18)$$

For the Arrhenius function in Equation (5), the acceleration factor in Equation (18) can be described as in Equation (19).

$$L_k = \frac{\hat{\beta}_1 \exp\left(-\frac{\hat{\beta}_2}{T_u}\right)}{\hat{\beta}_1 \exp\left(-\frac{\hat{\beta}_2}{T_k}\right)} \quad (19)$$

Where L_k is given for each thermal stress level T_k . Simplifying the acceleration factor in Equation (19), can be calculated as in Equation (20).

$$L_k = \exp\left(-\frac{\hat{\beta}_2}{T_u} + \frac{\hat{\beta}_2}{T_k}\right) \quad (20)$$

RESULTS AND DISCUSSIONS

In this section, the degradation modeling framework and the parameter estimates are presented to calculate the first passage time (times to failure) distribution, and acceleration factor using them as a reliability estimation approach.

Parameter Estimation

The parameters of interest $\theta = (\beta_1, \beta_2, \sigma)$ were estimated via MLE. The *maxLik* function in the R software was used to solve and maximize the log-likelihood function in (6) [28]. The code presented in Appendix A was considered and the obtained estimations for the parameters are presented in Table 2. By obtaining $\hat{\theta}$, as previously discussed, the first passage time (time to failure) distribution and the acceleration factor can be calculated for each thermal stress level T_k .

TABLE 2. Estimation of parameters for the Wiener process.

Parameter	Estimate
α	4.3544
β_1	-1.4980
β_2	349.3925

Estimated First-Passage Time

Once the parameters of interest of the Wiener process, and the Arrhenius function were estimated from the degradation data of the DUTs, the first-passage time distributions for each thermal stress level were calculated. The *divGauss* function in the R software was used to characterize the PDF in (17), while *pinvGauss* function was used to characterize the cumulative distribution function (CDF) and reliability function $R(t)$ [28]. The IG distribution mean $\hat{\mu}_k$, and scale $\hat{\lambda}$

estimated are presented in Table 3. It can be easily found that the time to failure mean ($\hat{\mu}$) expressed in days becomes smaller as the thermal stress level increases. For 50 °C, the time to failure mean is ~104 days while for 80 °C is ~95 days. This result is related to the molecular weight that gives to polymers their stiffness. The higher the molecular weight, the higher stiffness, and higher tensile strength. The molecular weight and stiffness vary for each polymer being the

TABLE 3. First passage time distributions parameters for the different stress levels.

Temperature (°C)	$\hat{\mu}_k$	$\hat{\lambda}$
50	103.79	146.69
60	100.48	
70	97.45	
80	94.68	

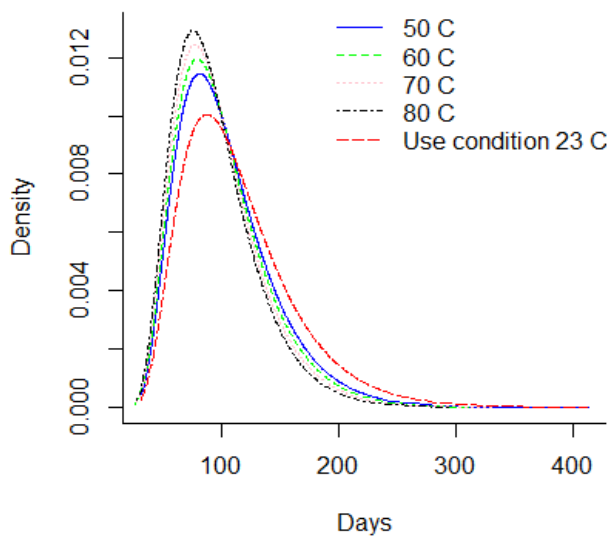


FIGURE 8. The PDF of all thermal stress conditions and use condition.

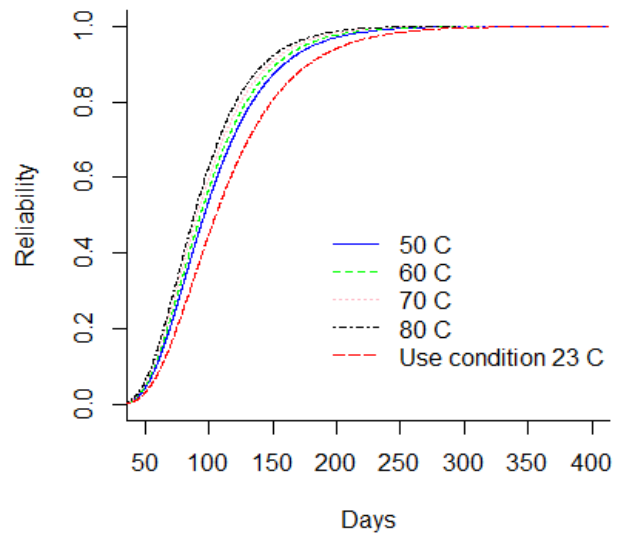


FIGURE 9. The CDF of all thermal stress conditions and use condition.

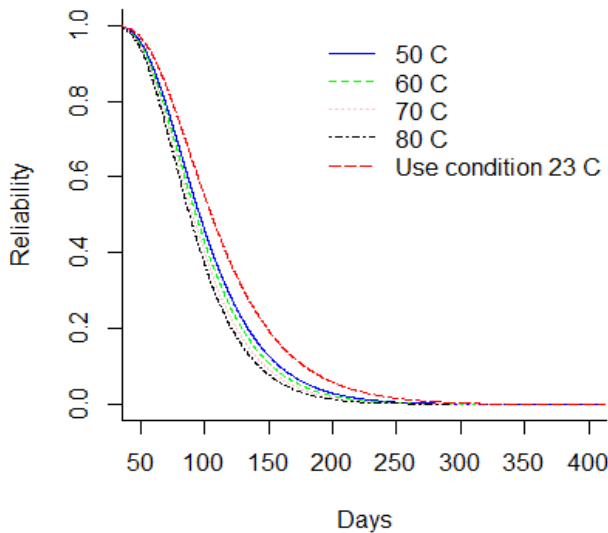


FIGURE 10. The R(t) function of all thermal stress conditions and use condition.

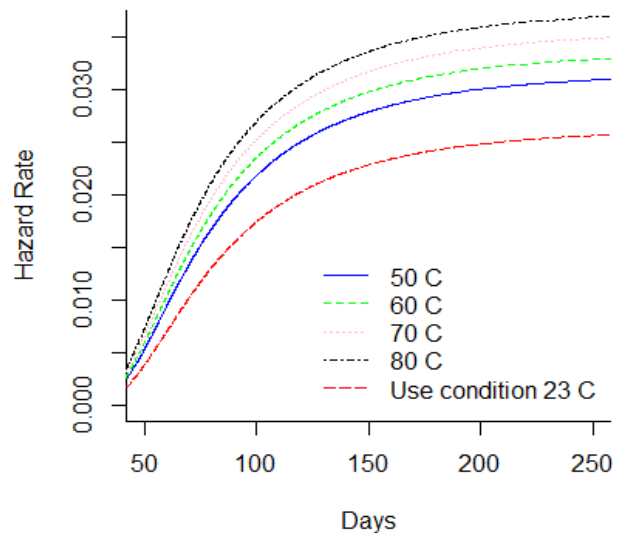


FIGURE 11. The H(t) function of all thermal stress conditions and use condition.

polymer of the distal tip with the lowest stiffness and molecular weight, thus lowest tensile strength. Additionally, a difference of three days for $\hat{\mu}_k$ is noted among all temperatures tested, which means that for 10°C of temperature increase, the time to failure mean increases three days. The PDF, CDF, reliability function $R(t)$, and hazard function $h(t)$ of the DUT for all thermal stress conditions and use condition are depicted in Figure 8 up to Figure 11 respectively.

Considering, a storage or use condition temperature of 23 °C, it can be observed from Figure 8 that the PDF is lower in comparison to greater thermal stress level. Figure 9 and Figure 10 showed the CDF and their function of complement, which is the reliability function $R(t)$. It is noted that the reliability function $R(t)$ is greater for the DUT that are storage at use condition temperature in comparison to the DUT storage at 80°C. Also, it is noted that the reliability of the DUT storage at use condition differs from the shelf life claimed in the labeling. Otherwise, the hazard function $h(t)$ in Figure 11 is lower for the DUT storage at condition temperature in comparison to DUT storage at 80 °C. Additionally, from Figure 10, it can be noted that the reliability of the DUTs rapidly decreases from day 60 to day 250 in all temperature levels. On the other hand, from Figure 11, it can be noted that the hazard rate rapidly increases until 150 days approximately and the stabilizes from then on. This behavior suggests that the probability of instant failure is low at 0 days of exposure to the thermal stress, then the probability increases and stabilizes as more days of thermal exposure are considered.

It should be noted that the van't Hoff's observation is an empirical method that has been deemed as conservative [2]. Furthermore, this method is used as an acceleration factor to estimate the time that is needed to subject a DUT under a thermal stress in the aims of simulate certain shelf life. Therefore, the aging test results in a reliability demonstration test, that consid-

ers the estimated time to subject the DUT under the accelerated thermal stress to finally test the DUT and demonstrate that the DUT has a successful performance, i.e., the tensile strength is higher than 15 N. Indeed, the ADDT presented in this study differs from this approach, given that it presents the possibility of modeling the behavior of the characteristic of interest under a certain stress factor, such that it is possible to determine a failure for a defined critical value of the characteristic under a determined stress level. This modeling of the evolution of the characteristic of interest complements the reliability estimation of the DUT beyond a reliability demonstration plan.

Estimated Acceleration Factors

The parameters of interest of the Arrhenius function denoted as β_1 and β_2 were estimated from the degradation data of the DUT. These parameters were used to calculate the acceleration factor for each thermal stress level based on the function in (19). The acceleration factor estimated is presented in Table 4.

TABLE 4. Estimated acceleration actor for each temperature.

Temperature (°C)	L_k
50	1.10
60	1.14
70	1.17
80	1.21

From Table 4 it can be easily found that the acceleration factor becomes smaller as the thermal stress decreases. For 50 °C, the acceleration factor is 1.10 while for 80 °C is 1.21. That means that the ratio of time to achieve the same level of change in the tensile strength tends to be one, as the accelerated temperature approaches to the temperature of the normal use condition. Otherwise, a higher acceleration factor compensates for the effect of thermal stress to estimate the normal use condition. These acceleration factors are

smaller compared to the ones that can be estimated based on the van't Hoff's observation. As previously discussed, the van't Hoff AAF tends to establish conservative estimations. Based on the function in (1) and the estimated acceleration factors in Table 4, the Q_{10} that must be considered for the characteristic studied in this paper results in $Q_{10} = 1.03$. This differs from the $Q_{10} = 2$ empirical value which may result in early failure of the DUT, even before their expiration date.

CONCLUSIONS

This paper presents an ADDT as an alternative to the accelerated-aging policies based on standards and guidelines.

Many accelerated aging methodologies are available to evaluate the reliability of the medical devices during their design and development. However, currently, there is not an official method. ADDT performed in this study can be used as a helpful custom method based on a critical performance characteristic of the medical device specifically intravascular catheters, under the assumption that the tensile strength follows a Wiener process and the constant-stress loading used is the temperature. It is noted that the proposed method can determine the lifetime distribution in function of time and thermal stress levels to provide data that support the shelf life, and the storage ambient conditions claimed in the medical device labeling. However, the results to support the shelf life found in this study differs from the results obtained from the traditional method of accelerated aging $Q_{10} = 2$. Therefore, real-time aging data continue to be necessary to validate the shelf life.

Future work could tackle several topics, one of them is to estimate the Ea as a random parameter. The constant activation energy and constant reactant concentrations is an assumption that has been used in this study. This assumption may be evaluated differently, as a parameter to be estimated to provide a highly accurate estimate of real performance. Another topic, consist in consider the unit-to-unit heterogeneity, in theory, the intravascular catheters use the same materials and manufacturing process, however, in the practice there are differences, so that, the degradation rates for the individual system are different. For this reason, the heterogeneity among the units should be incorporated into the Wiener process in the diffusion parameter. Finally, as a validation process it may be possible to test intravascular catheters under a certain condition until failure in the aims of confirm the MTTF estimation presented in this paper. Finally, an important topic for future research may be to subject an efficient sample size of DUTs to validate the estimated MTTFs for every temperature level. Although, it must be considered that the accelerated test is destructive with constant stress levels, which means that the equipment's must be used for large periods.

AUTHOR CONTRIBUTIONS

K.E.H and L.A.R.P. conceptualized the project, developed the methodology, performed the formal and the statistical analysis, designed specialized software and wrote the manuscript. K.E.H. performed the experiments and carried out the final tests on the devices. R.R.L. and L.C.M.G. oversaw the development of the methodology, reviewed and validated the final version of the manuscript. All authors reviewed and approved the final version of the manuscript.

REFERENCES

- [1] Hukins DWL, Mahomed A, Kukureka SN. Accelerated aging for testing polymeric biomaterials and medical devices. *Med Eng Phys* [Internet]. 2008;30(10):1270-1274. Available from: <https://doi.org/10.1016/j.medengphy.2008.06.001>
- [2] Lambert BJ, Tang F-W. Rationale for practical medical device accelerated aging programs in AAMI TIR 17. *Radiat Phys Chem* [Internet]. 2000;57(3-6):349-353. Available from: [https://doi.org/10.1016/S0969-806X\(99\)00403-X](https://doi.org/10.1016/S0969-806X(99)00403-X)
- [3] Clark, GS. Shelf Life of Medical Devices [Internet]. Division of Small Manufacturers Assistance, Office of Training and Assistance, Center for Devices and Radiological Health, Food and Drug Administration; 1991. 31p. Available from: <https://www.fda.gov/media/72487/download>
- [4] Hemmerich KJ. General aging theory and simplified protocol for accelerated aging of medical devices. *Met Plast Biomater*. 1998;5:16-23.
- [5] ASTM International. ASTM F1980-07(2011) Standard Guide for Accelerated Aging of Sterile Barrier Systems for Medical Devices. ASTM International [Internet]; 2016. Available from: <https://doi.org/10.1520/F1980-07R11>
- [6] Sawant M, Christou A. Failure modes and effects criticality analysis and accelerated life testing of LEDs for medical applications. *Solid State Electron* [Internet]. 2012;78:39-45. Available from: <https://doi.org/10.1016/j.sse.2012.05.042>
- [7] Pan D, Lu S, Liu Y, Yang W, et al. Degradation Data Analysis Using a Wiener Degradation Model with Three-Source Uncertainties. *IEEE Access* [Internet]. 2019;7:37896-37907. Available from: <https://doi.org/10.1109/ACCESS.2019.2906325>
- [8] Yang G. *Life Cycle Reliability Engineering* [Internet]. Hoboken: John Wiley & Sons, Inc; 2007. 517p. Available from: <http://dx.doi.org/10.1002/9780470117880>
- [9] Lim H, Yum B-J. Optimal design of accelerated degradation tests based on Wiener process models. *J Appl Stat* [Internet]. 2011;38(2):309-325. Available from: <https://doi.org/10.1080/02664760903406488>
- [10] Rodríguez-Picón LA, Pérez-Domínguez L, Mejía J, Pérez-Olguín JJ, et al. A Deconvolution Approach for Degradation Modeling with Measurement Error. *IEEE Access* [Internet]. 2019;7:143899-143911. Available from: <http://dx.doi.org/10.1109/access.2019.2945566>
- [11] Rodríguez-Picón LA, Rodríguez-Picón AP, Alvarado-Iniesta A. Degradation modeling of 2 fatigue-crack growth characteristics based on inverse Gaussian processes: A case study. *Appl Stoch Model Bus Ind* [Internet]. 2019;35(3):504-521. Available from: <http://dx.doi.org/10.1002/asmb.2329>
- [12] Rodríguez-Picón LA, Flores-Ochoa VH, Méndez-González LC, Rodríguez-Medina MA. Bivariate degradation modelling with marginal heterogeneous stochastic processes. *J Stat Comput Simul* [Internet]. 2017;87(11):2207-2226. Available from: <http://dx.doi.org/10.1080/00949655.2017.1324858>
- [13] Li T, Pei H, Pang Z, Si X, et al. A Sequential Bayesian Updated Wiener Process Model for Remaining Useful Life Prediction. *IEEE Access* [Internet]. 2020;8:5471-5480. Available from: <http://dx.doi.org/10.1109/ACCESS.2019.2962502>
- [14] Lyu Y, Zhang Y, Chen K, Chen C, et al. Optimal Multi-Objective Burn-In Policy Based on Time-Transformed Wiener Degradation Process. *IEEE Access* [Internet]. 2019;7:73529-73539. Available from: <http://dx.doi.org/10.1109/ACCESS.2019.2918510>
- [15] Escobar LA, Meeker WQ, Kugler DL, Kramer LL. Accelerated Destructive Degradation Tests: Data, Models, and Analysis. Series on Quality, Reliability and Engineering Statistics [Internet]. In: Lindvist BH, Doksum KA (eds). *Mathematical and Statistical Methods in Reliability*. River Edge: World Scientific Publishing Company; 2003. 319-337p. Available from: http://dx.doi.org/10.1142/9789812795250_0021
- [16] Tsai C-C, Tseng S-T, Balakrishnan N, Lin C-T. Optimal Design for Accelerated Destructive Degradation Tests. *Qual Technol Quant Manag* [Internet]. 2013;10(3):263-276. Available from: <http://dx.doi.org/10.1080/16843703.2013.11673413>
- [17] Shi Y, Meeker WQ. Bayesian Methods for Accelerated Destructive Degradation Test Planning. *IEEE Trans Reliab* [Internet]. 2012;61(1):245-253. Available from: <http://dx.doi.org/10.1109/TR.2011.2170115>
- [18] Shi Y, Escobar LA, Meeker WQ. Accelerated Destructive Degradation Test Planning. *Technometrics* [Internet]. 2009;51(1):1-13. Available from: <http://dx.doi.org/10.1198/TECH.2009.0001>
- [19] Food and Drug Administration. CFR - Code of Federal Regulations Title 21. Food and Drug Administration [Internet]. 2019. Available from: <https://www.fda.gov/medical-devices/medical-device-databases/code-federal-regulations-title-21-food-and-drugs>
- [20] Food and Drug Administration. Guidance on Premarket Notification [510(k)] Submission for Short-Term and Long-Term Intravascular Catheters. Food and Drug Administration [Internet]. 1995. Available from: <https://www.fda.gov/media/72722/download>
- [21] Food and Drug Administration. Coronary and Peripheral Arterial Diagnostic Catheters - Guidance for Industry and FDA Staff. Food and Drug Administration [Internet]. 2003. Available from: <https://www.fda.gov/media/71373/download>
- [22] Food and Drug Administration. Peripheral Percutaneous Transluminal Angioplasty (PTA) and Specialty Catheters - Premarket Notification (510(k)) Submissions. Food and Drug Administration [Internet]. 2020. Available from: <https://www.fda.gov/media/134016/download>
- [23] Food and Drug Administration. MDR - Medical Device Recalls. Food and Drug Administration [Internet]. 2020. Available from: <https://www.accessdata.fda.gov/scripts/cdrh/cfdocs/cfRES/res.cfm>
- [24] Food and Drug Administration. MAUDE - Manufacturer and User Facility Device Experience. Food and Drug Administration [Internet]. 2020. Available from: <https://www.accessdata.fda.gov/scripts/cdrh/cfdocs/cfMAUDE/search.CFM>
- [25] Lanzer P. *Mastering Endovascular Techniques: A Guide to Excellence*. Baltimore: Lippincott Williams & Wilkins; 2006. 480p.
- [26] International Organization Standardisation (ISO). ISO 10555-1: Intravascular catheters – Sterile and single-use catheters – Part 1: General requirements. Geneva, Switzerland: International Organization for Standardisation. 2013. 24p.
- [27] Kahle W, Mercier S, Paroissin C. *Degradation Processes in Reliability* [Internet]. New Jersey: John Wiley & Sons; 2016. 211p. Available from: <http://dx.doi.org/10.1002/9781119307488>
- [28] GNU. The R Project for Statistical Computing R [Internet]. 2016. Available from: <https://www.R-project.org/>

APPENDIX A. Estimation code

```

#Loglikelihood function
loglik<-function(param){
a<-param[1]
b<-param[2]
s<-param[3]
ll<- -((r*n*m/2)*log(2*pi))-(0.5*sum(log(t)))-
(r*n*m*log(s))-sum(((y-(a*t*exp(-b/T)))^2)/(2*t*(s^2)))
ll }

#Gradient
loglikGrad <- function(param) {
a<-param[1]
b<-param[2]
s<-param[3]
loglikGradValues <- numeric(3)
loglikGradValues[1] <-
sum(((y-(a*t*exp(-b/T))) * exp(-b/T))/(s^2))
loglikGradValues[2] <- -sum(((y-(a*t*exp(-b/T))) *
(a/T) * exp(-b/T) ) / (s^2) )
loglikGradValues[3] <- -((r*n*m)/s) + sum(((y- (a*t*exp(-b/T)))^2)/ (t*(s^3)))
return(loglikGradValues) }

#Hessian
loglikHess <- function(param) {
a <- param[1]
b <- param[2]
s <- param[3]
loglikHessValues <- matrix(0, nrow = 3, ncol = 3)
loglikHessValues[1, 1] <- sum((-t*exp(-((2*b)/T)))/
(s^2))
loglikHessValues[1, 2] <-
sum((((2*a*t)/T)*exp(-((2*b)/T))-(y/T)*exp(-b/T)) /
(s^2))
loglikHessValues[1, 3] <- -2*sum(
((y-(a*t*exp(-b/T))) * exp(-b/T) ) / (s^3) )
loglikHessValues[2, 1] <- loglikHessValues[1, 2]
loglikHessValues[2, 2] <- -sum( ((2*t*(a^2))/
(T^2)*exp(-((2*b)/T)))-((y*a)/T)*exp(-b/T))/(s^2))
loglikHessValues[2, 3] <- 2*sum( ((y-(a*t*exp(-b/T))) *
(a/T) * exp(-b/T) ) / (s^3) )
loglikHessValues[3, 1] <- loglikHessValues[1, 3]
loglikHessValues[3, 2] <- loglikHessValues[2, 3]
loglikHessValues[3, 3] <- ((r*n*m)/(s^2))- sum((3*((y -
(a*t*exp(-b/T) ) )^2))/ (t*(s^4) ) )
return(loglikHessValues)}

mleHess<- maxLik(logLik = loglik,loglikGrad, log-
likHess, start = c(a=1,b=100,s=4),method="NR")
summary(mleHess)

```

dx.doi.org/10.17488/RMIB.43.2.3

E-LOCATION ID: 1254

Comparison of Accuracy of Color Spaces in Cell Features Classification in Images of Leukemia types ALL and MM

Comparación de Precisión de Espacios de Color en la Clasificación de Características de Células en Imágenes de Leucemia tipos ALL y MM

Cinthia Espinoza-Del Angel , Aurora Femat-Diaz  

Universidad Autónoma de Querétaro

ABSTRACT

This study presents a methodology for identifying the color space that provides the best performance in an image processing application. When measurements are performed without selecting the appropriate color model, the accuracy of the results is considerably altered. It is significant in computation, mainly when a diagnostic is based on stained cell microscopy images. This work shows how the proper selection of the color model provides better characterization in two types of cancer, acute lymphoid leukemia, and multiple myeloma. The methodology uses images from a public database. First, the nuclei are segmented, and then statistical moments are calculated for class identification. After, a principal component analysis is performed to reduce the extracted features and identify the most significant ones. At last, the predictive model is evaluated using the k-nearest neighbor algorithm and a confusion matrix. For the images used, the results showed that the CIE L*a*b color space best characterized the analyzed cancer types with an average accuracy of 95.52%. With an accuracy of 91.81%, RGB and CMY spaces followed. HSI and HSV spaces had an accuracy of 87.86% and 89.39%, respectively, and the worst performer was grayscale with an accuracy of 55.56%.

KEYWORDS: PCA, Statistical moments, Color spaces, Leukemia images

RESUMEN

Este estudio presenta una metodología para identificar el espacio de color que proporciona el mejor rendimiento en una aplicación de procesamiento de imágenes. Cuando las mediciones se realizan sin seleccionar el modelo de color adecuado, la precisión de los resultados se altera considerablemente. Esto es significativo en el procesamiento, principalmente cuando el diagnóstico se basa en imágenes de microscopía de células teñidas. Este trabajo muestra cómo la selección adecuada del modelo de color proporciona una mejor caracterización en dos tipos de cáncer, la leucemia linfocítica aguda y el mieloma múltiple. La metodología utiliza imágenes de una base de datos pública. Primero, se segmentan los núcleos y luego se calculan los momentos estadísticos para la identificación de clases. Posteriormente, se realiza un análisis de componentes principales para reducir las características extraídas e identificar las más significativas. Por último, el modelo predictivo se evalúa utilizando el algoritmo k-vecinos más cercanos y una matriz de confusión. Para las imágenes utilizadas, los resultados mostraron que el espacio de color CIE L*a*b caracterizó mejor los tipos de cáncer analizados con una precisión promedio del 95,52%. Con una precisión del 91,81%, siguieron los espacios RGB y CMY. Los espacios HSI y HSV tuvieron una precisión del 87,86% y el 89,39%, respectivamente, y el peor desempeño fue la escala de grises con una precisión del 55,56%.

PALABRAS CLAVE: PCA, Momentos estadísticos, Espacios de color, Imágenes de leucemia

Corresponding author

TO: Aurora Femat-Diaz

INSTITUTION: Universidad Autónoma de Querétaro

ADDRESS: Facultad de Ingeniería, Universidad Autónoma de Querétaro, Cerro de las Campanas S/N, Col. Las Campanas, Centro, C. P. 76010, Santiago de Querétaro, Querétaro, México

CORREO ELECTRÓNICO: afemat@uaq.mx

Received:

11 March 2022

Accepted:

9 May 2022

INTRODUCTION

Leukemia is a blood disease distinguished by the abnormal production of white blood cells [1]. Its diagnosis uses a blood smear where the presence of myeloblasts or lymphoblasts is determined [2] [3]. This examination is usually a time-consuming manual process and requires microscopist expertise [4] [5] [6]. Recently, image processing techniques with machine learning have been used, which integrate image processing and segmentation, feature extraction and selection, and a classification algorithm [7] [8]. The most critical steps are segmentation and selection of significant features [9] [10] [11].

During microscopic analysis, cells are stained to provide visibility and contrast [12]. The segmentation stage separates the cells from the rest of the image from the acquired color. Among the techniques that have been applied to segment are K means [13] [14] [15] [16] [17] [18], Fuzzy c-means [19], Triangle thresholding [20] [21] [22], and Otsu thresholding [9] [23] [24] [25] [26], which are usually accompanied by the Watershed algorithm to divide adjacent or overlapping cells [27] [28].

From the nucleus or cytoplasm, parameters are calculated that help to identify cancer types. Several features can be analyzed, including geometric, statistical, and texture [21] [26] [29]. The number of parameters used should be limited using a reduction algorithm to improve the efficiency of classification model [30] [31].

Some methods to decrease the number of characteristics are Univariate feature selection (k-Best) [32], Social Spider Optimization Algorithm (SSOA) [33], Genetic Algorithm (GA) [25], Statistically Enhanced Salp Swarm Algorithm (SESSA) [34], Linear Discriminant Analysis (LDA) [35] and Principal Component Analysis (PCA) [35] [36] [37]. The latter is a statistical technique that reduces the dimension of a data set and generates a new set of uncorrelated variables. These are called principal components (PC), and their relationship preserves the maximum variation from the original data set [38] [39].

On the other hand, color models are used to define the way to represent the tones mathematically. The color spaces RGB [9] [26], CMYK [16] [20] [35], HSI [23] [40], HSV [19] [24], and CIE L*a*b [14] [41], and grayscale [25] [42] [43] have been used for this type of application. Studies have identified that RGB is not ideal for the segmentation of these cells, while HSI, HSV, and CMY perform better [44] [45]. In a group of images where the capture brightness effect varies, the use of HSV space may be the most appropriate because it separates the image intensity from the color information [17] [19].

In feature extraction, statistical and color properties have been obtained from various spaces such as, RGB [21] [30], HSV [13] [19] [46], HSI [35] and CIE L*a*b [14]. Of these, RGB and HSV spaces are the most widely used, but the use of these representations has not been justified [14] [21] [33] [47]. Although statistical and color features are an important source of information, no studies have yet been performed to compare the accuracy of color space using these characteristics in cell sorting with staining.

This paper proposes to use a principal component analysis with statistical descriptors as input variables to determine the color space that best represents the information of a set of images. This process is analyzed by using the k nearest neighbors (kNN) algorithm and a confusion matrix to determine the accuracy of the predictive model. The objective of the study is to propose a tool to image processing methodologies to identify the model that best represents the content of the region of interest (ROI). In particular, it is applied to identify two types of cancer, acute lymphoid leukemia (ALL) and multiple myeloma (MM).

MATERIAL AND METHODS

Image Dataset Definition

The set of images used in this work is a collection of microscopic bone marrow images of patients diagnosed with B-lineage acute lymphoid leukemia and

multiple myeloma, published in The Cancer Imaging Archive (TCIA) by Gupta, A. and Gupta, R. [48]. They have a resolution of 2560x1920 pixels, were captured using a Nikon Eclipse-200 microscope at 1000x magnification, and slides were stained with Jenner-Giemsa stain. This study used 60 samples, 30 ALL and 30 MM.

Nucleus Segmentation of Leukemia Cells

Based on studies by Jagadev and Virani [17], Mirmohammadi *et al.* [19], and Rahman and Hasan [21], the image segmentation was performed using the HSV space, considering that it separates the intensity of the image from the color information, and the images of the database do not have uniform brightness. For the segmentation process, first, the intensity of the images was

adjusted to a range of 0.1 to 0.7 using the value channel (V) to decrease the capture luminance effect [19]. The ROI was defined with a threshold value in the Hue (H) and Saturation (S) components. After a binary segmentation, the holes were filled using a morphological closure with disk shape structure element of radius 4 [49]. The watershed algorithm was used to the resulting image to separate the overlapping nuclei. Subsequently, objects with an area of fewer than 17500 pixels and elements with an eccentricity greater than 0.80 and solidity less than 0.65 were removed [14] [21] [50]. The ROI was established from the original images using the binary mask. A total of 484 blast cell nuclei, 168 ALL and 316 MM, were then extracted. The segmentation results for two sample images are visualized in Figure 1.

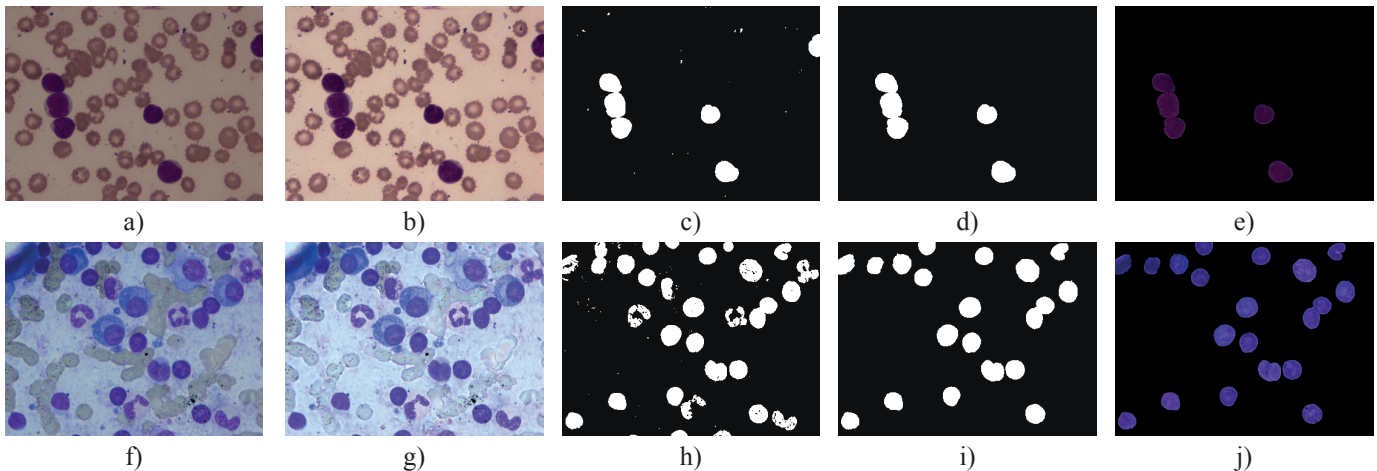


FIGURE 1. Steps of Leukemic Cell Segmentation. ALL original image is shown in a).

ALL Image enhancement in b). ALL binary mask in c). ALL filtering and watershed segmentation in d).

ALL segmentation result in e). MM original image in f). MM Image enhancement in g). MM binary mask in h).

MM filtering and watershed segmentation in i). MM segmentation result j).

Feature Extraction

Mean, variance, standard deviation, skewness, kurtosis, entropy, and energy, were calculated for each nucleus from an image for each color space channel and grayscale. Equations 1 to 7 show the definition of each one of these parameters, where Z represents the intensity as a random variable, $p(Z)$, $i= 0, 1, 2, \dots, L-1$ is the probability of occurrence of the value Z_i and L is the number of different possible values

[51]. For each leukemia cell, a total of 21 features were obtained in each color space and 7 for grayscale.

$$mean = \sum_{i=0}^{L-1} Z_i p(Z_i) \quad (1)$$

$$Variance = \sum_{i=0}^{L-1} (Z_i - m)^n p(Z_i) \quad (2)$$

$$SD = \sqrt{\sum_{i=0}^{L-1} (Z_i - m)^n p(Z_i)} \quad (3)$$

$$Skewness = \sum_{i=0}^{L-1} (Z_i - m)^3 p(Z_i) \quad (4)$$

$$Kurtosis = \sum_{i=0}^{L-1} [(Z_i - m)^4 p(Z_i)]^{-3} \quad (5)$$

$$Entropy = - \sum_{i=0}^{L-1} p(Z_i) \log_2 p(z_i) \quad (6)$$

$$Energy = \sum_{i=0}^{L-1} p^2(Z_i) \quad (7)$$

Feature Selection

The most significant features of each color space were identified using principal component analysis. First, the number of statistical descriptors in the dataset was

reduced using the “statistics” and “FactoRMine” libraries of Rstudio software [52] [53]. For this, we first checked for a low partial correlation value between each pair of features, using the Kaiser-Meyer-Olkin (KMO) coefficient. If for any of these pairs, *mean-variance*, *mean-standard deviation*, *mean-skewness*, etc., the KMO coefficient is less than 0.5, the value indicates that it is not appropriate to use PCA in that model. Then Bartlett's test of sphericity (BTS) with a significance level of $p < 0.05$ is used to estimate the correlation between variables.

PCA for each color model was performed based on an initial data table represented by a matrix of 484 rows, containing 168 observations of ALL and 316 MM type cells. The measurement result for each statistical descriptor is shown by columns (21 characteristics for the RGB, CMY, HSV, HSI, and CIE L *a*b color spaces and 7 for grayscale). Table 1 shows an example of this for the RGB model components.

TABLE 1. Data matrix for RGB for an example image. Mean (M), variance (V), standard deviation (SD), Skewness (S), energy (Er) and entropy (Et). The initial of RGB channels was added to each descriptor.

Sample	MR	VR	SDR	SR	KR	ErR	EtR	MG	...	EtG	MB	...	EtB
ALL_1_1	85.26	266.19	16.32	-0.22	0.71	0.02	0.74	42.10	...	0.59	103.07	...	0.62
ALL_1_2	85.09	253.95	15.94	-0.48	0.07	0.02	0.74	42.70	...	0.59	105.67	...	0.63
ALL_1_3	88.99	69.71	8.35	0.31	0.13	0.03	0.63	42.63	...	0.56	106.09	...	0.55
⋮	⋮
⋮	⋮
MM_30_10	143.32	99.41	9.97	1.33	3.03	0.03	0.65	65.77	...	0.65	120.03	...	0.52
MM_30_11	97.95	337.36	18.37	0.93	2.23	0.02	0.77	43.93	...	0.60	106.36	...	0.61
MM_30_12	122.91	138.44	11.77	0.42	0.08	0.02	0.70	57.04	...	0.67	115.60	...	0.54

Each table column is standardized to an average of 0 and a standard deviation of 1 using Equation 8, where X_j is the value to be standardized, X_{js} represents the standardized value and, μ_x and σ_x are the average and the standard deviation of the column.

$$X_{js} = \frac{X_j - \mu_x}{\sigma_x} \quad (8)$$

A covariance matrix was calculated using the standardized values for each table to estimate the correlation and dependence between variables. Equation 9 was used to evaluate covariances between each pair of characteristics. Where σ_{jk} is the covariance between the two variables, X_j and X_k represent the standardized value of variables j and k , μ_j and μ_k are the column averages of variables j and k , and n is the total data per

column. The correlation coefficient of the covariances was determined by Equation 10. It is obtained by dividing the covariance by the standard deviations of X_j and X_k represented by σ_j and σ_k .

$$\sigma_{jk} = \frac{1}{n} \sum_{i=1}^n (X_j - \mu_j)(X_k - \mu_k) \quad (9)$$

$$\sigma_{jk} = \frac{\frac{1}{n} \sum_{i=1}^n (X_j - \mu_j)(X_k - \mu_k)}{\sigma_j \sigma_k} \quad (10)$$

The covariance matrix C is represented as in Equation 11, where $Cov_{(i,j)}$ is the covariance between the elements in row i and column j . This matrix is decomposed into its eigenvalues and eigenvectors to determine the principal components. By solving Equation 12, the eigenvalues λ_k are obtained and for each of them, its eigenvector V_k is determined using Equation 13, where I is the identity matrix. The eigenvectors correspond to the principal components, and the eigenvalues define the magnitude of the variance of the new set of variables. Finally, the eigenvectors are sorted in descending order to select the components that retain at least 80% of the information from the original data set.

$$C = \begin{bmatrix} \sigma_{1,1} & Cov_{1,2} & \dots & Cov_{1,m} \\ Cov_{2,1} & \sigma_{2,2} & \dots & Cov_{2,m} \\ \vdots & \vdots & \ddots & \vdots \\ Cov_{n,1} & Cov_{n,2} & \dots & \sigma_{n,m} \end{bmatrix} \quad (11)$$

$$\det(\lambda I - C) = 0 \quad (12)$$

$$(\lambda_k I - C) * V_k = 0 \quad (13)$$

ALL and MM Classification

The ALL and MM cancer types were classified using the principal components or new variables. For this purpose, the k nearest neighbor algorithm was employed using the Rstudio software^[54]. Data was randomly divided into two sets. 80% of them were used as training data and the remaining 20% as test data.

In the training phase, the kNN algorithm stores the set of input variables to establish a relationship between them and the conditions to be classified, calculating a distance between the rows of training data and the test set data. It was determined as a function of the Euclidean distance (ED) using Equation 14, where A and B represent the principal component vectors $A = (x_1, x_2, x_3, x_4, \dots, x_m)$, $B = (y_1, y_2, y_3, y_4, \dots, y_m)$, and m , the dimensionality of the feature space.

$$ED(A, B) = \sqrt{\sum_{i=1}^m (x_i - y_i)^2} \quad (14)$$

The resulting vector was ordered from smallest to largest so that the smallest distance is considered the k nearest neighbor.

Subsequently, a number for k was defined to determine the nearest neighbors to include in the voting process using Equation 15. N represents the total data in the training set. The operation resulted in a $k = 17$.

$$k = \sqrt{N} \quad (15)$$

Finally, to determine the performance of the kNN classifier, the confusion matrix was applied. The metric provided is the accuracy and is defined by Equation 16. Where TP is the true positives, FN is the false negatives, FP indicates the number of false positives, and TN is the number of true negatives.

$$Accuracy = \frac{TP + TN}{TP + TN + FP + FN} \quad (16)$$

Statistical Analysis











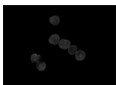

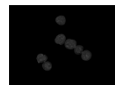



Lastly, differences of accuracy between color and grayscale spaces were analyzed using a one-way analysis of variance (ANOVA) and Tukey's posthoc test. The sample size was calculated using statistical power analysis. A significance level of 0.05 was established,

with a power of 0.8 and an effect size of 0.25. The study determined a sample size of 35. The normality of the residuals was assessed by performing the Shapiro Wilks test, and Bartlett's test demonstrated the homogeneity of variances. For each analysis, was used a significance level of $p < 0.05$.

RESULTS AND DISCUSSION

This section shows the results of the comparison between color spaces and grayscale. Table 2 shows an example of channel decomposition and grayscale conversion of an example image.

TABLE 2. Channel division of color representations. Channel 1, Channel 2 and Channel 3 correspond to the color band of each color space.

Color System	Channel 1	Channel 2	Channel 3
Grayscale			
RGB			
CMY			
HSI			
CIE L*a*b			
HSV			

As presented in Table 1, KMO coefficient was calculated; in all cases, the value was greater than 0.5. Bartlett's test was performed considering the parameters of all images as input, presenting for each color space a significant p-value less than $\alpha = 0.05$. Thus, the application of the PCA is adequate. The results of these tests are shown in Table 3.

TABLE 3. Results for Kaiser-Meyer-Olkin measure of sampling adequacy (KMO) and Bartlett's test of sphericity (BTS). Chi-square (χ^2), degrees of freedom (df), p value (p), statistic (stat) and grayscale (GS).

Test	Stat	GS	RGB	CMY	HSI	L*a*b	HSV
KMO		0.61	0.72	0.72	0.68	0.71	0.62
	χ^2	5779	20621	20621	20728	20133	18346
BTS	df	21	210	210	210	210	210
	p	<0.05	<0.05	<0.05	<0.05	<0.05	<0.05

The summary of the PCA is shown in Table 4. The principal components were selected according to the total variance method, retaining at least 80% of the information of the original set of variables. In RGB, CMY, CIE L*a*b, and HSI spaces, 4 PCs were taken; in HSV, 5 PCs; and in grayscale, 2 PCs.

TABLE 4. Principal component analysis summary. The percentage of cumulative variance (Cum. Var) retained by the PC's are highlighted in blue. Principal component (PC), eigenvalue (λ), variance (Var).

Color System	PC	λ	Var (%)	Cum. Var (%)
Grayscale	1	3.49	49.9	49.9
	2	2.73	38.9	88.8
RGB	1	8.02	38.2	38.2
	2	5.95	28.3	66.5
	3	1.72	8.21	74.7
	4	1.46	6.94	81.7
CMY	1	8.02	38.2	38.2
	2	5.95	28.3	66.5
	3	1.72	8.21	74.7
	4	1.46	6.94	81.7
HSI	1	6.42	30.6	30.6
	2	5.18	24.7	55.2
	3	4.00	19	74.3
	4	1.85	8.82	83.1
CIE	1	7.53	35.9	35.9
	2	6.00	28.6	64.5
	3	2.04	9.71	74.2
	4	1.49	7.11	81.3
HSV	1	5.82	27.7	27.7
	2	4.51	21.5	49.2
	3	3.11	14.8	64.0
	4	1.96	9.36	73.3
	5	1.83	8.71	82.0

The results show that grayscale retains more information in its first two components than the color spaces (see Table 4 data highlighted in blue). The CIE L*a*b space has the highest information loss of 81.3%.

A two-dimensional PCA space was projected for each color model considering the first two components with the highest contribution, as shown in Figure 2. The upper and right coordinates (abscissa and ordinate axis for PC1 and PC2 loadings) show the degree of contribution to the principal components. In these graphs, the black vectors called loadings represent the statistical descriptors. Charge vectors range is from -1 to 1. Charges close to |1| indicate that the variable strongly influences the principal component; those close to 0 denote a weak influence.

A coefficient greater than |0.5| is considered significant to define a PC. For example, for Figure 1a corresponding to grayscale PCA, the *mean* (M), *skewness* (S), *kurtosis* (K), and *energy* (Er) contribute most to PC1. *Variance* (V), *standard deviation* (SD), *energy* (Er) and *entropy* (Et) contribute most to PC2.

The angle between loadings is their correlation. Vectors with equal directions are positively correlated, and those with opposite directions are negatively correlated. If they present an angle of 90°, there is no correlation. The vertical and horizontal axes show the percentage of variability explained by the principal components. The points on the graph are the channel measurements of the color models. Cancer types are grouped in concentration ellipses, ALL cells in blue and MM cells in orange.

As shown in Figure 2, vector loadings differ between color representations, yet it is possible to establish a reliable prediction model because the loadings are significant. Although the clusters of the two cancers overlap at some points in the two-dimensional PCA

space, a clear separation is visualized between the ALL and MM descriptors (Figure 2a to Figure 2f). The precision results when evaluating the predictive model using kNN are shown in Table 5. Each of the 35 samples was studied using a different random data set.

TABLE 5. kNN Accuracy results for each color model. Data are in percentage. Grayscale (GS). Average (μ).

No.	GS	RGB	CMY	HSI	L*a*b	HSV
1	86.6	89.7	89.7	87.6	95.9	92.8
2	87.6	91.8	91.8	93.8	100.0	92.8
3	86.6	90.7	90.7	84.5	93.8	86.6
4	85.6	89.7	89.7	86.6	95.9	86.6
5	88.7	95.9	95.9	93.8	96.9	93.8
6	84.5	93.8	93.8	88.7	97.9	89.7
7	84.5	88.7	88.7	80.4	96.9	86.6
:	:	:	:	:	:	:
34	78.4	92.8	92.8	89.7	95.9	87.6
35	88.7	91.8	91.8	87.6	93.8	85.6
μ	84.7	91.8	91.8	87.9	95.5	89.4

A one-way ANOVA was then applied to compare the performance of each color model statistically. First, the normality of the residuals was tested using the Shapiro-Wilks test; the p-value = 0.0947 showed that they did follow normal behavior. Bartlett's test determined compliance with homogeneity of variance between treatments with a p-value of 0.2215, suggesting no evidence of statistically significant variation between color representations for ANOVA.

The variance analysis revealed a significant difference between the color models with a p-value less than 0.05 (See Table 6).

TABLE 6. One-way ANOVA results. Sum of squares (SS), mean square (MS).

Source	Df	SS	MS	F value	p-value
Model	5	2436	487.2	54.12	<2e-16
Error	204	1836	9.0		

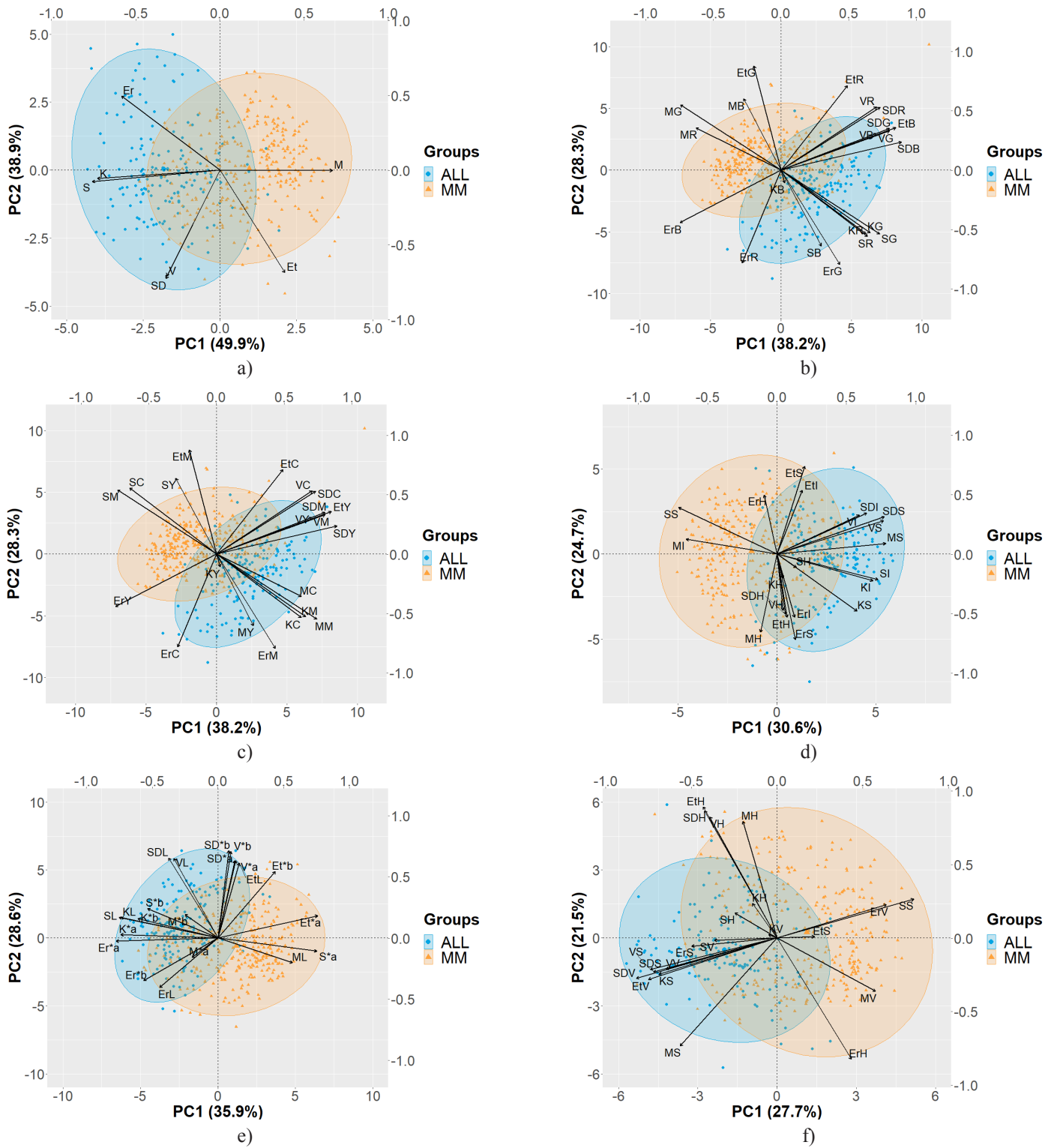


FIGURE 2. PCA biplot for components 1 and 2. Grayscale is shown in a), RGB in b), CMY in c), HSI in d), CIE L*a*b in e), and HSV in f). Ellipses represent a concentration of the scores for each group set with 95% confidence boundaries. *Mean (M), variance (V), standard deviation (SD), Skewness (S), energy (Er) and entropy (Et).*

In Figure 3, the distribution of color representations exhibits a normal distribution; outliers are minimal. The whiskers in the box represent the boundaries of the precision samples drawn for each group. The red dot indicates the mean accuracy of color representation. In grayscale was 84.7; in RGB, 91.8; in CMY, 91.8; in HSI, 87.9; in HSV, 89.4; and in CIE L*a*b, 95.5. The predictive model given by the characteristics of the CIE L*a*b color space obtained the highest accuracy, followed by the RGB and CMY spaces. Grayscale was the worst performer.

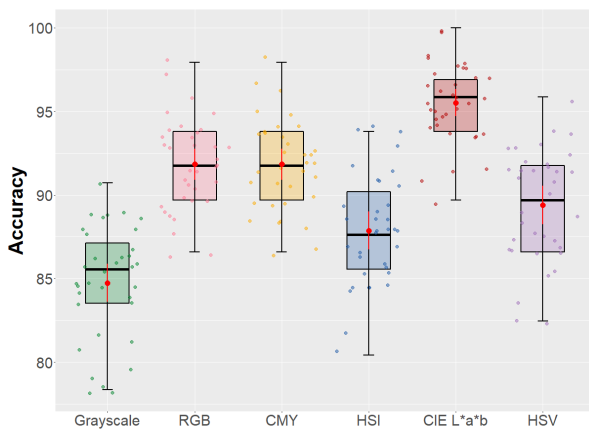


FIGURE 3. Anova results for each color model.

The pairwise comparisons of means of the color models obtained by Tukey's test can be seen in Figure 4.

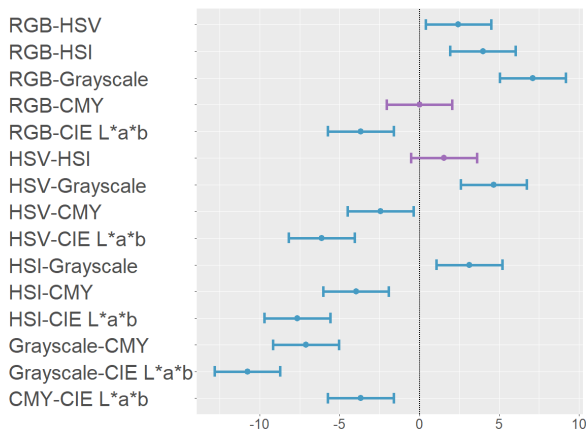


FIGURE 4. Tukey post hoc test pairwise comparison plot. Extended lines in blue color show statistically significant differences between the pairs of means, and extended lines in purple indicate that there is no statistical difference between the means.

In the graph, the extended lines show the 95% confidence intervals. Those crossing the 0 points indicate that there is no statistically significant difference between the pairs of means. The analysis revealed that there is no inequality between RGB and CMY spaces (p -value = 1.00); and HSI and HSV spaces (p -value = 0.27408).

CONCLUSIONS

The use of machine learning and image processing methods play an important role in image analysis for prognosis and early detection of blood cancer. Research for leukemia image classification techniques has used color characteristics from RGB and HSV spaces [21] [30] [13] [19] [46], but other color models are rarely used.

This article presents a methodology to compare the accuracy of different color models to represent the characteristics of leukemia cells. Of the color spaces analyzed, the CIE L*a*b best described the two cancer types, ALL and MM, using color moments with an average accuracy of 95.52%.

Compared to reference articles, the accuracy obtained in this study was superior to that of [36], which used RGB and grayscale space color and texture features. The PCA and the KNN and SVM classifiers were used, obtaining an accuracy of 91.45% and 92.63%, respectively.

Likewise, a better performance was obtained than [30], which used the color characteristics of the RGB space and compared six classifiers; KNN (80.7%), tree classifier (75.8%), ANN (83.5%), logistic regression (82.4%), random forest (81.0%) and SVM (73.6%). The method proposed was similar to the studies [14] [19] in which the SVM classifier was used. In [14], the color characteristics of the RGB, HSV, and CIE L*a*b spaces were used, reaching an accuracy of 95.28%, and in [19], texture characteristics of the grayscale were used, achieving an accuracy of 95%. The presented method has provided novel information on how color spaces can

influence the selection of features for image analysis of leukemic cells. Future research could extend the classification approach by considering other cancer types or subtypes, using other classifiers, or selecting different feature selection methods.

AUTHOR CONTRIBUTIONS

C.E.-D.A. and A.F.-D. Conceptualized the project, developed aims and goals, participated in software development. C.E.-D.A. Collected data and performed data curation and carried out the statistical analyses, programming, and code implementation; designed and developed the methodology, performed experiments, verified the reproducibility of the results, and oversaw the presentation and visualization of data, contributed to writing the draft and final version of the manuscript, edited critical reviews and responses to reviewer comments. A.F.-D. Provided study materials, literature and computer resources and tools for image processing, provided and work with the leukemia imaging database, oversaw the writing of the

manuscript, carried out techniques of software image processing to analyze data, developed and designed the methodology, validated the results of the investigation, obtained funding. Both authors reviewed and approved the final version of the manuscript.

ACKNOWLEDGMENTS

The authors would like to thank to the Consejo Nacional de Ciencia y Tecnología (CONACYT) for financing this work through the “Programa Nacional de Posgrados de Calidad (PNPC)” scholarship 1033981.

ETHICAL STATEMENT

The data used in this work is from public dataset: Gupta A, Gupta R. SN-AM Dataset: White Blood Cancer Dataset of B-ALL and MM for Stain Normalization [Internet]. The Cancer Imaging Archive; 2019. Available from: <https://doi.org/10.7937/tcia.2019.of2w8lrx>.

CONFLICTS OF INTEREST

The authors declare no conflict of interest.

REFERENCES

- [1] McKenzie SB, Williams JL. Clinical Laboratory Hematology. 3rd ed. Boston: Pearson; 2014. 1037p.
- [2] Bozzone DM. The Biology of Cancer: Leukemia. New York, N.Y.: Chelsea House Pub; 2009. 168p.
- [3] Sabath DE. Leukemia. In: Maloy S, Hughes K (eds). Brenner's Encyclopedia of Genetics [Internet]. Academic Press; 2013. 226-227p. Available from: <https://doi.org/10.1016/B978-0-12-374984-0.00862-7>
- [4] Halim NHA, Mashor MY, Hassan R. Automatic Blasts Counting for Acute Leukemia Based on Blood Samples. Int J Res Rev Comput Sci [Internet]. 2011;2(4):971-976. Available from: <https://www.lumenera.com/media/wysiwyg/documents/whitepapers/IJRRCS-Research-Article.pdf>
- [5] Hazra T, Kumar M, Tripathy SS. Automatic Leukemia Detection Using Image Processing Technique. Int J Latest Technol Eng Manag Appl Sci [Internet]. 2017;6(4):42-45. Available from: <https://www.ijtemas.in/DigitalLibrary/Vol.6Issue4/42-45.pdf>
- [6] Putzu L, Caocci G, Di Ruberto C. Leucocyte classification for leukaemia detection using image processing techniques. Artif Intell Med [Internet]. 2014;62(3):179-191. Available from: <https://doi.org/10.1016/j.artmed.2014.09.002>
- [7] Mittal A, Dhalla S, Gupta S, Gupta A. Automated analysis of blood smear images for leukemia detection: a comprehensive review. ACM Comput Surv [Internet]. 2022;1-36. Available from: <https://doi.org/10.1145/3514495>
- [8] Shah A, Naqvi SS, Naveed K, Salem N, et al. Automated Diagnosis of Leukemia: A Comprehensive Review. IEEE Access [Internet]. 2021;9:132097-132124. Available from: <https://doi.org/10.1109/ACCESS.2021.3114059>
- [9] Mohammed ZF, Abdulla AA. Thresholding-based White Blood Cells Segmentation from Microscopic Blood Images. UHD J Sci Technol [Internet]. 2020;4(1):9-17. Available from: <https://doi.org/10.21928/uhdjt.v4n1y2020.pp9-17>
- [10] Alsalem MA, Zaidan AA, Zaidan BB, Hashim M, et al. A review of the automated detection and classification of acute leukaemia: Coherent taxonomy, datasets, validation and performance measurements, motivation, open challenges and recommendations. Comput Methods Programs Biomed [Internet]. 2018;158:93-112. Available from: <https://doi.org/10.1016/j.cmpb.2018.02.005>
- [11] Anilkumar KK, Manoj VJ, Sagi TM. A survey on image segmentation of blood and bone marrow smear images with emphasis to automated detection of Leukemia. Biocybern Biomed Eng [Internet]. 2020;40(4):1406-1420. Available from: <https://doi.org/10.1016/j.bbe.2020.08.010>
- [12] Mughal TI, Goldman JM, Mughal ST. Understanding Leukemias, Lymphomas and Myelomas. 2nd ed. London: CRC Press; 2013. 200p.
- [13] Dese K, Raj H, Ayana G, Yemane T, et al. Accurate Machine-Learning-Based classification of Leukemia from Blood Smear Images. Clin Lymphoma Myeloma Leuk [Internet]. 2021;21(11):903-914. Available from: <https://doi.org/10.1016/j.clml.2021.06.025>
- [14] Saeedizadeh Z, Mehri Dehnavi A, Talebi A, Rabbani H, et al. Automatic recognition of myeloma cells in microscopic images using bottleneck algorithm, modified watershed and SVM classifier. J Microsc [Internet]. 2016;261(1):46-56. Available from: <https://doi.org/10.1111/jmi.12314>
- [15] P R, P SD. Detection of Blood Cancer-Leukemia using K-means Algorithm. In: 2021 5th International Conference on Intelligent Computing and Control Systems (ICICCS) [Internet]. Madurai: IEEE; 2021:838-842. Available from: <https://doi.org/10.1109/ICICCS51141.2021.9432244>
- [16] Soni F, Sahu L, Getnet ME, Reta BY. Supervised Method for Acute Lymphoblastic Leukemia Segmentation and Classification Using Image Processing. In: 2018 2nd International Conference on Trends in Electronics and Informatics (ICOEI) [Internet]. Tirunelveli: IEEE; 2018:1075-1079. Available from: <https://doi.org/10.1109/ICOEI.2018.8553937>
- [17] Jagadev P, Virani HG. Detection of leukemia and its types using image processing and machine learning. In: 2017 International Conference on Trends in Electronics and Informatics (ICEI) [Internet]. Tirunelveli: IEEE; 2017:522-526. Available from: <https://doi.org/10.1109/ICOEI.2017.8300983>
- [18] Kumar P, Udwadia SM. Automatic detection of acute myeloid leukemia from microscopic blood smear image. In: 2017 International Conference on Advances in Computing, Communications and Informatics (ICACCI) [Internet]. Udupi: IEEE; 2017:1803-1807. Available from: <https://doi.org/10.1109/ICACCI.2017.8126106>
- [19] Mirmohammadi P, Ameri M, Shalbfaf A. Recognition of acute lymphoblastic leukemia and lymphocytes cell subtypes in microscopic images using random forest classifier. Phys Eng Sci Med [Internet]. 2021;44(2):433-441. Available from: <https://doi.org/10.1007/s13246-021-00993-5>
- [20] Abdeldaim AM, Sahlol AT, Elhoseny M, Hassanien AE. Computer-Aided Acute Lymphoblastic Leukemia Diagnosis System Based on Image Analysis. In: Hassanien A, Oliva D (eds). Studies in Computational Intelligence [Internet]. Cham: Springer; 2018:730.131-147p. Available from: https://doi.org/10.1007/978-3-319-63754-9_7
- [21] Rahman A, Hasan MM. Automatic Detection of White Blood Cells from Microscopic Images for Malignancy Classification of Acute Lymphoblastic Leukemia. In: 2018 International Conference on Innovation in Engineering and Technology (ICIET) [Internet]. Dhaka: IEEE; 2018:1-6. Available from: <https://doi.org/10.1109/CIET.2018.8660914>
- [22] Shafique S, Tehsin S, Anas S, Masud F. Computer-assisted Acute Lymphoblastic Leukemia detection and diagnosis. In: 2019 2nd International Conference on Communication, Computing and Digital systems (C-CODE) [Internet]. Islamabad: IEEE; 2019:184-189. Available from: <https://doi.org/10.1109/C-CODE.2019.8680972>
- [23] Singhal V, Singh P. Texture Features for the Detection of Acute Lymphoblastic Leukemia. In: Satapathy S, Joshi A, Modi N, Pathak N (eds). Advances in Intelligent Systems and Computing [Internet]. Singapore: Springer; 2016:535-43. Available from: https://doi.org/10.1007/978-981-10-0135-2_52
- [24] Rehman A, Abbas N, Saba T, Rahman SIU, et al. Classification of acute lymphoblastic leukemia using deep learning. Microsc Res Tech [Internet]. 2018;81(11):1310-1317. Available from: <https://doi.org/10.1002/jemt.23139>
- [25] Rawat J, Singh A, HS B, Virmani J, et al. Computer assisted classification framework for prediction of acute lymphoblastic and acute myeloblastic leukemia. Biocybern Biomed Eng [Internet]. 2017;37(4):637-654. Available from: <https://doi.org/10.1016/j.bbe.2017.07.003>

- [26] Muntasa A, Yusuf M. Color-Based Hybrid Modeling to Classify the Acute Lymphoblastic Leukemia. *Int J Intell Eng Syst* [Internet]. 2020;13(4):408-422. Available from: <https://doi.org/10.22266/ijies2020.0831.36>
- [27] Mandal S, Daivajna V, V R. Machine Learning based System for Automatic Detection of Leukemia Cancer Cell. In: 2019 IEEE 16th India Council International Conference (INDICON) [Internet]. New Delhi: IEEE; 2019:1-4. Available from: <https://doi.org/10.1109/INDICON47234.2019.9029034>
- [28] Acharya V, Kumar P. Detection of acute lymphoblastic leukemia using image segmentation and data mining algorithms. *Med Biol Eng Comput* [Internet]. 2019;57(8):1783-1811. Available from: <https://doi.org/10.1007/s11517-019-01984-1>
- [29] Bagasjvara RG, Candradewi I, Hartati S, Harjoko A. Automated detection and classification techniques of Acute leukemia using image processing: A review. In: 2016 2nd International Conference on Science and Technology-Computer (ICST) [Internet]. Yogyakarta: IEEE; 2016:35-43. Available from: <https://doi.org/10.1109/ICSTC.2016.7877344>
- [30] Belhekar A, Gagare K, Bedse R, Bhelkar Y, et al. Leukemia Cancer Detection Using Image Analytics : (Comparative Study). In: 2019 5th International Conference On Computing, Communication, Control And Automation (ICCUBEA) [Internet]. Pune: IEEE; 2019:1-6. Available from: <https://doi.org/10.1109/ICCUBEA47591.2019.9128546>
- [31] Khalid S, Khalil T, Nasreen S. A survey of feature selection and feature extraction techniques in machine learning. In: 2014 Science and Information Conference [Internet]. London: IEEE; 2014:372-378. Available from: <https://doi.org/10.1109/SAI.2014.6918213>
- [32] Kumar D, Jain N, Khurana A, Mittal S, et al. Automatic Detection of White Blood Cancer From Bone Marrow Microscopic Images Using Convolutional Neural Networks. *IEEE Access* [Internet]. 2020;8:142521-142531. Available from: <https://doi.org/10.1109/ACCESS.2020.3012292>
- [33] Sahlol AT, Abdeldaim AM, Hassanien AE. Automatic acute lymphoblastic leukemia classification model using social spider optimization algorithm. *Soft Comput* [Internet]. 2019;23(15):6345-6360. Available from: <https://doi.org/10.1007/s00500-018-3288-5>
- [34] Sahlol AT, Kollmannsberger P, Ewees AA. Efficient Classification of White Blood Cell Leukemia with Improved Swarm Optimization of Deep Features. *Sci Rep* [Internet]. 2020;10(1):2536. Available from: <https://doi.org/10.1038/s41598-020-59215-9>
- [35] Mishra S, Majhi B, Sa PK. Texture feature based classification on microscopic blood smear for acute lymphoblastic leukemia detection. *Biomed Signal Process Control* [Internet]. 2019;47:303-311. Available from: <https://doi.org/10.1016/j.bspc.2018.08.012>
- [36] Pešić I. Segmentation and Classification of Leucocyte Images for Detection of Acute Lymphoblastic Leukemia. In: 2020 7th ETRAN&ICETAN international conference [Internet]. Belgrade: ICETAN; 2020:2-7. Available from: https://www.etrans.rs/2020/ZBORNIK_RADOVA/Radovi_prikazani_na_konferenciji/047_BT11.7.pdf
- [37] Mirmohammadi P, Taghavi A, Ameri A. Automatic Recognition of Acute Lymphoblastic Leukemia Cells from Microscopic Images. *Int J Innov Res Sci Eng* [Internet]. 2017;5(7):8-11. Available from: <https://ijirse.in/docs/2017/Sep%2017/IJIRSE170902.pdf>
- [38] Salih Hasan BM, Abdulazeez AM. A Review of Principal Component Analysis Algorithm for Dimensionality Reduction. *J Soft Comput Data Min* [Internet]. 2021;2(1):20-30. Available from: <https://publisher.uthm.edu.my/ojs/index.php/jscdm/article/view/8032>
- [39] Jolliffe IT. *Principal Component Analysis* [Internet]. New York: Springer; 2002. 488p. Available from: <https://doi.org/10.1007/b98835>
- [40] Harun NH, Bakar JA, Wahab ZA, Osman MK, et al. Color Image Enhancement of Acute Leukemia Cells in Blood Microscopic Image for Leukemia Detection Sample. In: 2020 IEEE 10th Symposium on Computer Applications & Industrial Electronics (ISCAIE) [Internet]. Malaysia: IEEE; 2020:24-9. Available from: <https://doi.org/10.1109/ISCAIE47305.2020.9108810>
- [41] Sukanya CM, Vince P. AML Detection in Blood Microscopic Images Using DRLBP and DRLTP Feature Extraction. *Int J Eng Sci Comput* [Internet]. 2016;6(6):6942-6946. Available from: <https://ijesc.org/upload/16ed93ec7acaf83596e4dc815fc66cad.AML%20Detection%20in%20Blood%20Microscopic%20Images%20Using%20%20DRLBP%20and%20DRLTP%20Feature%20Extraction.pdf>
- [42] Rege MV, Abdulkareem MB, Gaikwad S, Gawli BW. Automatic Leukemia Identification System Using Otsu Image segmentation and MSER Approach for Microscopic Smear Image Database. In: 2018 Second International Conference on Inventive Communication and Computational Technologies (ICICCT) [Internet]. Coimbatore: IEEE; 2018:267-272. Available from: <https://doi.org/10.1109/ICICCT.2018.8473101>
- [43] Bhattacharjee R, Saini LM. Detection of Acute Lymphoblastic Leukemia using watershed transformation technique. In: 2015 International Conference on Signal Processing, Computing and Control (ISPPCC) [Internet]. Wagnaghat: IEEE; 2015:383-386. Available from: <https://doi.org/10.1109/ISPPCC.2015.7375060>
- [44] Shinde S, Sharma N, Bansod P, Singh M, et al. Automated Nucleus Segmentation of Leukemia Blast Cells : Color Spaces Study. In: 2nd International Conference on Data, Engineering and Applications (IDEA) [Internet]. Bhopal: IEEE; 2020:1-5. Available from: <https://doi.org/10.1109/IDEA49133.2020.9170721>
- [45] Nor Hazlyna H, Mashor MY, Mokhtar NR, Aimi Salihah AN, et al. Comparison of acute leukemia Image segmentation using HSI and RGB color space. In: 10th International Conference on Information Science, Signal Processing and their Applications (ISSPA 2010) [Internet]. Kuala Lumpur: IEEE; 2010:749-752. Available from: <https://doi.org/10.1109/ISSPA.2010.5605410>
- [46] Inbarani H H, Azar AT, G J. Leukemia Image Segmentation Using a Hybrid Histogram-Based Soft Covering Rough K-Means Clustering Algorithm. *Electronics* [Internet]. 2020;9(1):188. Available from: <https://doi.org/10.3390/electronics9010188>
- [47] Asadi F, Putra FM, Indah Sakinatunnisa M, Syafria F, et al. Implementation of Backpropagation Neural Network and Blood Cells Imagery Extraction for Acute Leukemia Classification. In: 2017 5th International Conference on Instrumentation, Communications, Information Technology, and Biomedical Engineering (ICICI-BME) [Internet]. Bandung: IEEE; 2017:106-110. Available from: <https://doi.org/10.1109/ICICI-BME.2017.8537755>
- [48] Gupta A, Gupta R. SN-AM Dataset: White Blood Cancer Dataset of B-ALL and MM for Stain Normalization [Data set]. The Cancer Imaging Archive; 2019. Available from: <https://doi.org/10.7937/tcia.2019.of2w8lxx>
- [49] Soille P. *Morphological Image Analysis: Principles and Applications*. 2nd ed. Berlin, Heidelberg: Springer; 2004. 392p.
- [50] Moshavash Z, Danyali H, Helfroush MS. An Automatic and Robust Decision Support System for Accurate Acute Leukemia Diagnosis from Blood Microscopic Images. *J Digit Imaging* [Internet]. 2018;31(5):702-717. Available from: <https://doi.org/10.1007/s10278-018-0074-y>

- [51] Gonzalez RC, Woods RE. Digital Image Processing. 4th ed. New York: Pearson; 2018. 1168p.
- [52] R Core Team, R. A language and environment for statistical computing. R Foundation for Statistical Computing, Vienna [Internet]. 2016. Available from: <https://www.R-project.org/>
- [53] Kassambara A, Mundt F. factoextra: Extract and Visualize the Results of Multivariate Data Analyses [Internet]. 2020. Available from: <https://cran.r-project.org/package=factoextra>
- [54] Venables WN, Ripley BD. Modern Applied Statistics with S [Internet]. 4th ed. New York: Springer; 2002. 516p. Available from: <https://doi.org/10.1007/978-0-387-21706-2>

dx.doi.org/10.17488/RMIB.43.2.4

E-LOCATION ID: 1246

Retinal Lesion Segmentation Using Transfer Learning with an Encoder-Decoder CNN

Segmentación de Lesiones en la Retina Usando Transferencia de Conocimiento con CNN Encoder-Decoder

Rafael Ortiz-Feregrino , Saúl Tovar-Arriaga  , Jesús Carlos Pedraza-Ortega , Andras Takacs 

Universidad Autónoma de Querétaro

ABSTRACT

Deep learning (DL) techniques achieve high performance in the detection of illnesses in retina images, but the majority of models are trained with different databases for solving one specific task. Consequently, there are currently no solutions that can be used for the detection/segmentation of a variety of illnesses in the retina in a single model. This research uses Transfer Learning (TL) to take advantage of previous knowledge generated during model training of illness detection to segment lesions with encoder-decoder Convolutional Neural Networks (CNN), where the encoders are classical models like VGG-16 and ResNet50 or variants with attention modules. This shows that it is possible to use a general methodology using a single fundus image database for the detection/segmentation of a variety of retinal diseases achieving state-of-the-art results. This model could be in practice more valuable since it can be trained with a more realistic database containing a broad spectrum of diseases to detect/segment illnesses without sacrificing performance. TL can help achieve fast convergence if the samples in the main task (Classification) and sub-tasks (Segmentation) are similar. If this requirement is not fulfilled, the parameters start from scratch.

KEYWORDS: Transfer learning, Encoder-decoder, Retinal images, Lesion segmentation, Deep learning

RESUMEN

Las técnicas de *Deep Learning* (DL) han demostrado un buen desempeño en la detección de anomalías en imágenes de retina, pero la mayoría de los modelos son entrenados en diferentes bases de datos para resolver una tarea en específico. Como consecuencia, actualmente no se cuenta con modelos que se puedan usar para la detección/segmentación de varias lesiones o anomalías con un solo modelo. En este artículo, se utiliza *Transfer Learning* (TL) con la cual se aprovecha el conocimiento adquirido para determinar si una imagen de retina tiene o no una lesión. Con este conocimiento se segmenta la imagen utilizando una red neuronal convolucional (CNN), donde los *encoders* o extractores de características son modelos clásicos como VGG-16 y ResNet50 o variantes con módulos de atención. Se demuestra así, que es posible utilizar una metodología general con bases de datos de retina para la detección/segmentación de lesiones en la retina alcanzando resultados como los que se muestran en el estado del arte. Este modelo puede ser entrenado con bases de datos más reales que contengan una gama de enfermedades para detectar/segmentar sin sacrificar rendimiento. TL puede ayudar a conseguir una convergencia rápida del modelo si la base de datos principal (Clasificación) se parece a la base de datos de las tareas secundarias (Segmentación), si esto no se cumple los parámetros básicamente comienzan a ajustarse desde cero.

PALABRAS CLAVE: Transferencia de conocimiento, Codificador-decodificador, Imágenes de retina, Segmentación de lesiones, Aprendizaje profundo

Corresponding author

TO: Saúl Tovar-Arriaga

INSTITUTION: Universidad Autónoma de Querétaro

ADDRESS: Cerro de las Campanas S/N, Col. Las Campanas, Centro, C. P. 76010, Santiago de Querétaro, Querétaro, México

CORREO ELECTRÓNICO: saul.tovar@uaq.mx

Received:

16 February 2022

Accepted:

11 May 2022

INTRODUCTION

The retina plays an essential role in vision since it transforms the received optical signals into electrical and transfers them to the brain. It provides a clear window to blood vessels and other essential parts of the neural tissue^[1]. Since it is an extension of the brain, it could also indicate possible mental health conditions^[1].

Ophthalmologists diagnose retinal diseases by identifying specific signs on retinal images. Such signs could be related to diseases such as diabetes, diabetic retinopathy (DR), macular degeneration, glaucoma, and cardiovascular problems. Some of them are progressive and asymptomatic until advanced states^[2]. Retinal image analysis turned into an essential matter in the medical area. Many kinds of research are being published to provide predictive information about many diseases even before clinical eye disease becomes detectable^{[3][4]}.

Retinal disease detection has been widely studied using artificial intelligence (AI) methods, specifically machine learning (ML). The ML area has constantly grown in recent years because of the rapid increase in the performance of their methods^[5]. They can detect if a retina presents DR and which grade of disease is^[6], or the lesion location in the image by segmentation^[7]^[8]. Most approaches train the algorithms from scratch, meaning the model must learn the parameters without a reference.

This work presents a methodology using transfer learning (TL) to segment different lesions using prior knowledge of what a lesion looks like in the retinal image using an encoder-decoder network and a variant of a traditional convolutional neural network (CNN)^[9]. The model's output is an image highlighting the target pixels (commonly referred to as segmentation). The proposed method uses the knowledge learned with a simple classification, whether an image has or not a lesion. Then, applying TL^[10], a new model segmented three injuries: exudates, hemorrhages, or microaneurysm.

This process reduces the training time significantly, and the pre-trained model is less susceptible to overfitting. It could be implemented in different tasks, for example, a classification of the anatomical parts or segmentation of different diseases like DR with retinal images.

Contribution

1. The methodology helps to have a generalized model before focusing on a specific lesion or disease.
2. Using a pre-trained model as an encoder in segmentation tasks with similar datasets reduces the training time and helps avoid overfitting.

Background

Retinal analysis is an area of much interest. It is not only used to know whether an eye has or not a disease but to segment areas of interest such as the optic disc, fovea area, veins, and arteries^{[11][12][13]}. Those tasks have been evaluated with classical ML algorithms like support vector machines^[14], or with more classic methods like mathematical morphological algorithms and naive Bayesian for image segmentation^[15]. Classical algorithms have attractive advantages because the models do not need many examples to perform well, which is a significant advantage since datasets are typically small.

Deep learning (DL) has been the preferred method to detect, classify, and segment medical images because of its power to generalize data; the only inconvenience is the need for many examples for model training. Lately, researchers have found new methods to confront this problem. Contributions like^[16] generate patches of the images to increase the number of examples of retina datasets. Another example implements the superpixel algorithm to generate patches^[17].

Most researchers focus on classifying a specific lesion^{[7][18][19][20]}. Others use pre-trained models of different datasets before starting the parameters fine-tuning. It

may help, but in many cases, the fine-tuning dataset is not similar to the pre-trained one, making it almost the same as if the training started from scratch [21]. Many researchers widely used datasets like IDRiD, Drive, CHASE-B, MESSIDOR, KAGGLE, and the papers focus are almost the same, detecting lesions [4] [22] [23] [24], classifying DR [6], or segmenting some anatomical parts [25], or injuries [26]. Nevertheless, the models are trained from scratch or using different pre-trained parameters in a different original dataset like IMAGENET.

Different DL models' effort is to improve the metrics related to the task [22], but not many works try to improve the methodology to avoid starting it from scratch. Works like [27] [28] try to identify a relationship between the vessels caliber and cardiovascular risk problems; an example of exudates segmentation using variants of the classical UNET model [21], with almost the same idea [29], take the dataset and train a model from scratch to segment microaneurysms or some other lesions [24], that classify their presence or absence. All the models achieve high performance, but they will not achieve good results if we try to generalize for different lesions for a specific task.

Most researchers focused on segmenting anatomical areas such as the optic disk, macula [11], veins, and artery [30], training DL models from scratch. Other authors use TL with pre-trained models in a completely different dataset [8] that helps start, but the parameters need to fit the new dataset.

MATERIALS AND METHODS

This methodology consists of two principal stages: stage 1 trains DL models to classify whether or not a retinal image has a lesion, and in stage 2, the objective is to segment a specific lesion employing the knowledge obtained in stage 1 using an encoder-decoder model. The proposed encoder-decoder model has the classifier model's feature extractor as its encoder, and therefore only training the decoder parameters to seg-

ment retinal lesions such as exudates, hemorrhages, or microaneurysms. However, this central idea could be applied to other diseases or segment anatomical parts.

Preprocessing data

As we can see in Figure 1, the proposed methodology starts with image preprocessing, which increases the contrast and luminosity by equalizing the original images using CLAHE [31]. This treatment improves the contrast of some structures like red dots, vessels, and microaneurysms that are difficult to visualize. Then, a data augmentation process is applied to generate two new images of each example consisting of rotations, image slides, or zoom.

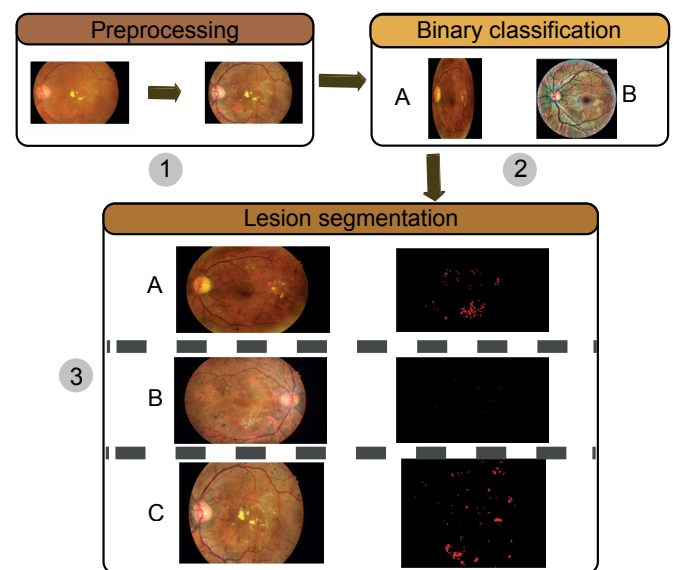


FIGURE 1. Methodology: 1) Preprocessing, 2) binary classification, where A is an image with a lesion and B is a healthy image, and 3) segmentation of injuries (A: exudates, B: microaneurysm, and C: hemorrhages).

The data sets used in stage 1 are the Messidor 1 [32], with 1054 images and Kaggle [33], with 36000. These data sets contain retinal images to classify DR grades. Our study uses them only to identify if an image has an injury, being a binary classification. We obtain 100046 training images and 11116 validation images by applying the preprocessing step.

The datasets used in stage 2 are 48 IDRiD [34] and 30 E-Optha [35], images. These datasets have exudates, hemorrhages, and microaneurysm annotations to execute a pixel-to-pixel classification. This stage uses patches of (160, 160, 3) to train the encoder-decoder model, which means that original images are divided in order to increase the number of examples to 36840 images. Figure 2 shows the two different sets of images used in stage 2.

Stage 1

As previously described, the main objective of stage 1 is to generate the knowledge to identify whether the mentioned lesions appear or not in the image; it does not matter where they are located. The models used for classification are shown in Figure 3. These models are the VGG-16 [36], ResNet50 [37], VGG-16 CBAM and ResNet50 CBAM. The last two models include CBAM [38], which pays attention to the channel and spatial axes. The models contain L2 regularizers [39], batch normalization layers [40], and dropouts [41], to prevent overfitting. The feature extractor of these models is used as an encoder in stage 2. The model's input is a tensor of shape (1, 480, 480, 3).

Stage 2

In stage 1, our models classify only whether an image has a lesion or not. However, now we want to know the lesion position in the image. The segmentation task

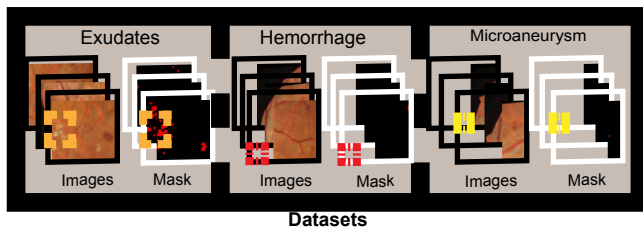


FIGURE 2. Three different datasets are used in stage 2. Each dataset has the original images patches and their mask.

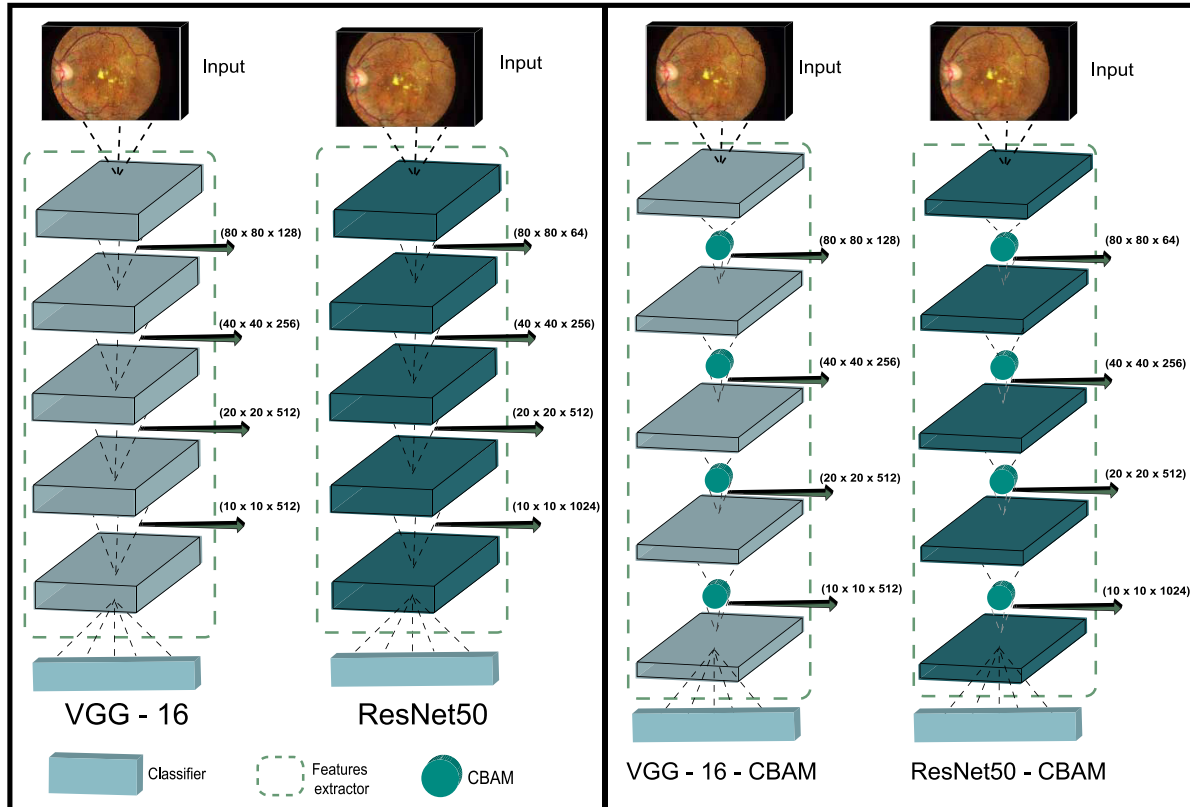


FIGURE 3. The four models were trained with the same hyperparameters: Adam optimizer, dropout, batch normalization, loss function, and activation functions.

consists of locating the required object pixels in the image. For this, we use an encoder-decoder model, the most classical architecture for image segmentation using DL. The segmentation model is not generated from scratch; it uses the feature extractor of the classifier model of stage 1 as the encoder. Typically, the proposed models in the literature are trained with random knowledge parameters meaning that the

model must learn what feature extractor maps are helpful to classify the images correctly; it takes more training time and could be more challenging to achieve good results.

The segmentation models, shown in Figure 4, are trained to segment a specific lesion, but not all the parameters are trained.

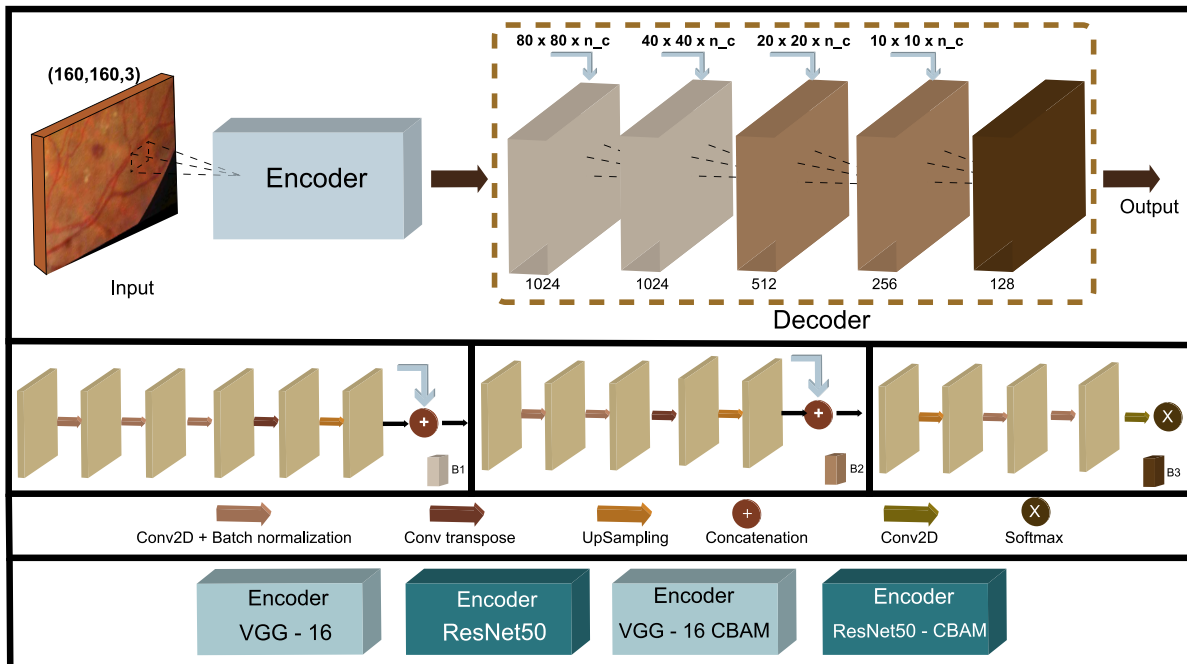


FIGURE 4. The proposed encoder-decoder model to segment the patch images consists of the feature extractor of the classifiers models as the encoder, with a residual operation at the end of each block.

As we mentioned earlier, in stage 1, the encoder generates the knowledge to identify how a lesion looks, so it is unnecessary to train the encoder parameters again, so we freeze them. The decoder parameters are trained to separately identify exudates, hemorrhages, and microaneurysms. We use three different datasets, one for each injury.

Software and Hardware

The models presented in this work were implemented in python 3 with TensorFlow and Keras libraries. OpenCV was used in the preprocessing part.

The classification and segmentation stages were trained in Colab with a GPU accelerator. The code is available in <https://github.com/MetaDown/RMIB-TL>.

RESULTS AND DISCUSSION

We divide the results into two parts: the binary classification model and the segmentation task. The second part has three different metrics for each injury (exudates, hemorrhages, and microaneurysm).

The classifier model obtains the metrics shown in Table 1.

TABLE 1. Binary classification results, showing whether an image has a lesion or not.

Model	Accuracy	Recall	Precision	Training time
VGG-16	87%	92%	80%	24 hrs.
VGG-16 CBAM	89%	81%	98%	26 hrs.
RESNET 50	86.6%	80.3%	90%	16 hrs.
RESNET 50 CBAM	87.1%	82%	90.02%	18 hrs.

This model does not pretend to achieve the best performance; the main task is to generate the knowledge to generalize how a lesion looks in the retinal images.

The classifier model can detect if an image has or does not have a lesion, and it pays attention to the lesion's shape, color, or composition. The knowledge is transferred to the segmentation model to classify pixel by pixel, and then the output is rebuilt to get the original image shape. Figure 5 compares the model segmentation with the ground truth and the original input image to have a better idea of the results; the metrics could show high performance, but it is challenging to observe the actual result due to most of the image being black.

Table 2 shows the performance of the four models, which have similar values, but the sensibility is the lower value of all. The accuracy or AUC metric could be

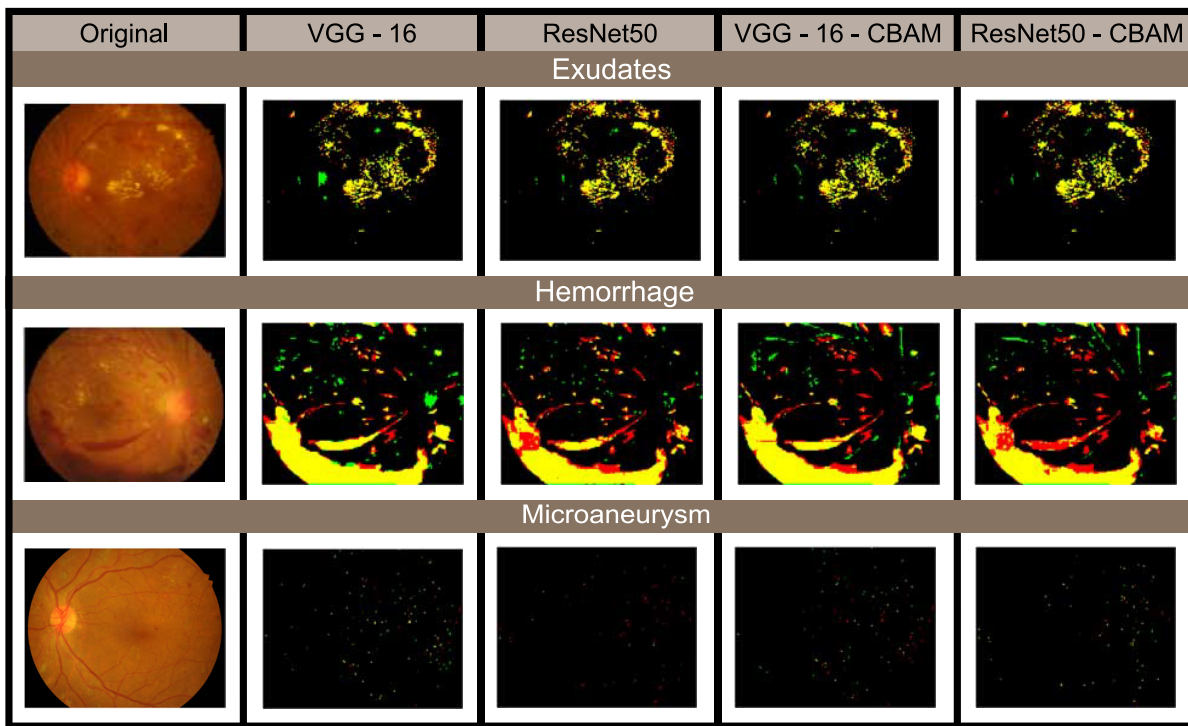


FIGURE 5. Exudates, hemorrhages, and microaneurysms segmentation results. Red pixels are false negatives, green pixels are false positives, yellow pixels represent true positives, and black pixels are true negatives.

misleading due to most of the pixels being black (No lesion presented). If we only pay attention to the accuracy or AUC metric, we are committing a mistake due to the pixel imbalance. We decide to compare the predictions directly with the ground truth to have a com-

plete idea of the model performance, as shown in figure 5. Microaneurysms are the most challenging lesions to segment; their shape and color could confuse other anatomical landmarks and other injuries. Metrics presented in other microaneurysms segmen-

TABLE 2. Metrics results with the validation data.

Author	Accuracy/ AUC/ F1 SCORE	Sensitivity	Specificity
Exudates			
Zong <i>et al.</i> [21]	Accuracy: 96.38%	96.14%	97.14%
Wisaeng <i>et al.</i> [42]	Accuracy: 98.35%	98.40%	98.13%
VGG-16	Accuracy: 98.1 %	88.12%	96.1 %
VGG-16 CBAM	Accuracy: 98.23%	89.46%	94.09%
RESNET 50	Accuracy: 98.09%	89.05%	96.05%
RESNET 50 CBAM	Accuracy: 97.04%	89.5%	97.2%
Hemorrhages			
Grinsven <i>et al.</i> [43]	AUC: 89.4%	91.9%	91.4%
Aziz <i>et al.</i> [19]	F1 Score 72.25%	74%	70%
VGG-16	Accuracy: 92.1 %	80.21%	94 %
VGG-16 CBAM	Accuracy: 92.09%	81.4%	94.9%
RESNET 50	Accuracy: 93.5%	81.6%	93.02%
RESNET 50 CBAM	Accuracy: 93.6%	82.01%	95.03%
Microaneurysms			
Long <i>et al.</i> [18]	AUC: 87 %	66.9 %	-
Kou <i>et al.</i> [29]	AUC: 99.99%	91.9%	93.6%
VGG-16	Accuracy: 93.1 %	73.13%	95.1 %
VGG-16 CBAM	Accuracy: 95.04%	74.6%	96.9%
RESNET 50	Accuracy: 95.69%	70.1%	97.8%
RESNET 50 CBAM	Accuracy: 96.2%	77.7%	98%

tation papers are high because the authors focused on improving the model in that specific task. Our proposed methodology focused on generalizing the model to achieve fast convergence in whatever assignment implies retinal images.

The training time in the segmentation stage by lesion was about one epoch or 28 min, achieving the results shown previously. We have excellent time training thanks to the TF applied in stage 1. The model doesn't need to fit the parameters from scratch.

If we only assess the segmenting accuracy, we could conclude that the metrics are very high. Nevertheless, this metric could be misleading since the imbalance present in retinal images is high. For example, the number of microaneurysms' pixels compared to the background pixels is very low. By showing the contrast between the actual and the predicted image, we can better understand the model's performance, Figure 5.

CONCLUSIONS

Training a model from scratch takes more time to fit the parameters until the excellent performance. TL is a powerful alternative to training models since it helps generalize faster than training from scratch. In this paper, using the knowledge learned in a binary classification, we proved that it is possible to perform a specific task like segmentation. The single requirement is a similar dataset as the main problem to solve.

Public datasets with segmenting masks are very limited because of the effort involved in preparing a single instance. This work proved that it is possible to take advantage of datasets created for detection/classification purposes to pre-train DL models to achieve better performance in segmentation tasks. The metrics achieved in our experiments are comparable to the state-of-the-art models and have the advantage of deploying a general methodology using a single fundus image database for the detection/segmentation of various retinal diseases achieving state-of-the-art results. This model could be in practice more valuable since it can be trained with a more realistic database containing a broad spectrum of conditions to detect/segment illnesses without sacrificing performance.

Future work would be to apply the same methodology presented in this work to the new architectures named Transformers, given that they require much more examples than CNN's, and tasks like medical image prediction or classification need a large number of samples, as we could see in the presented work. The advantage of the Transformers is the attention that its model could pay to some specific image regions, converting the Transformers into a strong candidate to replace the conventional CNN's. But we can ask, could we apply TF from CNN to a Transformer achieving fast convergence?

AUTHOR CONTRIBUTIONS

R.O.F. conceptualized the project, collected, and gathered raw data, performed data curation, proposed software for modelling and the methodology to seg-

ment and classify the lesions, designed the software for the implementation of models for the analyses, and contributed to writing the original draft. S.T.A. conceptualized the project, proposed software for modelling and the methodology to segment and classify the lesions and contributed to writing the original draft. J.C.P.O. performed data curation and contributed to the reviewing and editing of final version of the manuscript. A.T. proposed software for modelling and the methodology to segment and classify the lesions and contributed to the reviewing and editing of final version of the manuscript. All authors reviewed and approved the final version of the manuscript.

ETHICAL STATEMENT

The databases used in this work are public; therefore, all ethical considerations are met.

REFERENCES

- [1] Trucco E, MacGillivray T, Xu Y (eds). Computational Retinal Image Analysis [Internet]. Cambridge, United States: Elsevier; 2019. 481p. Available from: <https://doi.org/10.1016/B978-0-08-102816-2.09994-9>
- [2] Prado-Serrano A, Guido-Jiménez MA, Camas- Benítez JT. Prevalencia de retinopatía diabética en población mexicana. Rev Mex Oftalmol [Internet]. 2009; 83(5):261-266. Available: <https://www.medigraphic.com/pdfs/revmexoft/rmo-2009/rmo095c.pdf>
- [3] Ricci E, Perfetti R. Retinal Blood Vessel Segmentation Using Line Operators and Support Vector Classification. IEEE Trans Med Imaging [Internet]. 2007;26(10):1357-1365. Available from: <https://doi.org/10.1109/TMI.2007.898551>
- [4] Sarhan MH, Nasser MA, Zapp D, Maier M, et al. Machine Learning Techniques for Ophthalmic Data Processing: A Review. IEEE J Biomed Health Inform [Internet]. 2020;24(12):3338-3350. Available from: <http://dx.doi.org/10.1109/JBHI.2020.3012134>
- [5] Ammu R, Sinha N. Small Segment Emphasized Performance Evaluation Metric for Medical Images. 2020 International Conference on Signal Processing and Communications (SPCOM) [Internet]. Bangalore : IEEE;2020; 1-5. Available from: <http://dx.doi.org/10.1109/SPCOM50965.2020.9179617>
- [6] Quellec G, Charrière K, Boudi Y, Cochener B, et al. Deep image mining for diabetic retinopathy screening. Med Image Anal [Internet]. 2017;39:178-193. Available from: <https://doi.org/10.1016/j.media.2017.04.012>
- [7] Zhang X, Thibault G, Decencièrre E, Marcotegui B, et al. Exudate detection in color retinal images for mass screening of diabetic retinopathy. Med Image Anal [Internet]. 2014;18(7):1026-1043. Available from: <https://doi.org/10.1016/j.media.2014.05.004>
- [8] Feng Z, Yang J, Yao L, Qiao Y, et al. Deep Retinal Image Segmentation: A FCN-Based Architecture with Short and Long Skip Connections for Retinal Image Segmentation. In: Liu D, Xie S, Li Y, Zhao D, et al. (eds). Neural Information Processing ICONIP 2017. Lecture Notes in Computer Science, vol. 10637 [Internet]. Cham: Springer; 2017; 713-722. Available from: https://doi.org/10.1007/978-3-319-70093-9_76
- [9] Ye JC, Sung WK. Understanding Geometry of Encoder-Decoder CNNs. 36th International Conference on Machine Learning, ICML 2019 [Internet]. Long Beach: Proceedings of Machine Learning Research; 2019;97:12245-12254. Available from: <https://proceedings.mlr.press/v97/ye19a.html>
- [10] Tan C, Sun F, Kong T, Zhang W, et al. A Survey on Deep Transfer Learning. In: Manolopoulos Y, Hammer B, Iliadis L, Maglogiannis I (eds). Artificial Neural Networks and Machine Learning - ICANN 2018. ICANN 2018. Lecture Notes in Computer Science [Internet]. Cham: Springer; 2018. 11041: 270-279. Available from: http://dx.doi.org/10.1007/978-3-030-01424-7_27
- [11] Tang S, Qi Z, Granley J, Beyeler M. U-Net with Hierarchical Bottleneck Attention for Landmark Detection in Fundus Images of the Degenerated Retina. In: Fu H, Garvin MK, MacGillivray T, Xu Y, et al (eds). Ophthalmic Medical Image Analysis. OMIA 2021. Lecture Notes in Computer Science [Internet]. Cham: Springer; 2021. 12970:62-71. Available from: https://doi.org/10.1007/978-3-030-87000-3_7
- [12] Welikala RA, Foster PJ, Whincup PH, Rudnicka AR, et al. Automated arteriole and venule classification using deep learning for retinal images from the UK Biobank cohort. Comput Biol Med [Internet]. 2017;90:23-32. Available from: <https://doi.org/10.1016/j.combiomed.2017.09.005>
- [13] Fraz MM, Rudnicka AR, Owen CG, Barman SA. Delineation of blood vessels in pediatric retinal images using decision trees-based ensemble classification. Int J Comput Assist Radiol Surg [Internet]. 2014;9:795-811. Available from: <https://doi.org/10.1007/s11548-013-0965-9>
- [14] Adel A, Soliman MM, Khalifa NEM, Mostafa K. Automatic Classification of Retinal Eye Diseases from Optical Coherence Tomography using Transfer Learning. 2020 16th International Computer Engineering Conference (ICENCO) [Internet]. Cairo: IEEE; 2020: 37-42. Available from: <https://doi.org/10.1109/ICENCO49778.2020.9357324>
- [15] Xiao Z, Adel M, Bourennane S. Bayesian Method with Spatial Constraint for Retinal Vessel Segmentation. Comput Math Methods Med [Internet]. 2013:401413. Available from: <https://doi.org/10.1155/2013/401413>
- [16] Lam C, Yu C, Huang L, Rubin D. Retinal Lesion Detection with Deep Learning Using Image Patches. Invest Ophthalmol Vis Sci [Internet]. 2018;59(1):590-596. Available from: <https://doi.org/10.1167/iovs.17-22721>
- [17] Li Q, Feng B, Xie L, Liang P, et al. A Cross- Modality Learning Approach for Vessel Segmentation in Retinal Images. IEEE Trans Med Imaging [Internet]. 2016;35(1):109-118. Available from: <https://doi.org/10.1109/TMI.2015.2457891>
- [18] Long S, Chen J, Hu A, Liu H, et al. Microaneurysms detection in color fundus images using machine learning based on directional local contrast. Biomed Eng Online [Internet]. 2020;19(1):21. Available from: <https://doi.org/10.1186/s12938-020-00766-3>
- [19] Aziz T, Ilesanmi AE, Charoenlarnppaparut C. Efficient and Accurate Hemorrhages Detection in Retinal Fundus Images Using Smart Window Features. Appl Sci [Internet]. 2021;11(14):6391. Available from: <https://doi.org/10.3390/app11146391>
- [20] Liu Q, Liu H, Zhao Y, Liang Y. Dual-Branch Network with Dual-Sampling Modulated Dice Loss for Hard Exudate Segmentation in Colour Fundus Images. IEEE J Biomed Health Inform [Internet]. 2022;26(3):1091-1102. Available from: <https://doi.org/10.1109/jbhi.2021.3108169>
- [21] Zong Y, Chen J, Yang L, Tao S, et al. U-net Based Method for Automatic Hard Exudates Segmentation in Fundus Images Using Inception Module and Residual Connection. IEEE Access [Internet]. 2020;8:167225-35. Available from: <http://dx.doi.org/10.1109/ACCESS.2020.3023273>
- [22] Tan JH, Fujita H, Sivaprasad S, Bhandary SV, et al. Automated segmentation of exudates, haemorrhages, microaneurysms using single convolutional neural network. Inf Sci [Internet]. 2017;420:66-76. Available from: <https://doi.org/10.1016/j.ins.2017.08.050>
- [23] Kou C, Li W, Yu Z, Yuan L. An Enhanced Residual U-Net for Microaneurysms and Exudates Segmentation in Fundus Images. IEEE Access [Internet]. 2020;8:18514-18525. Available from: <http://dx.doi.org/10.1109/ACCESS.2020.3029117>






- [24] Gondal WM, Köhler JM, Grzeszick R, Fink GA, et al. Weakly-supervised localization of diabetic retinopathy lesions in retinal fundus images. 2017 IEEE International Conference on Image Processing (ICIP) [Internet]. Beijing: IEEE; 2017; 2069-2073. Available from: <https://doi.org/10.1109/ICIP.2017.8296646>
- [25] Joshi GD, Sivaswamy J, Krishnadas SR. Optic Disk and Cup Segmentation From Monocular Color Retinal Images for Glaucoma Assessment. IEEE Trans Med Imaging [Internet]. 2011;30(6):1192-1205. Available from: <https://doi.org/10.1109/TMI.2011.2106509>
- [26] Harangi B, Antal B, Hajdu A. Automatic exudate detection with improved naïve-Bayes classifier. 2012 25th IEEE International Symposium on Computer- Based Medical Systems (CBMS) [Internet]. Rome: IEEE; 2012; 1-4. Available from: <https://doi.org/10.1109/CBMS.2012.6266341>
- [27] Cheung CY, Xu D, Cheng CY, Sabanayagam C, et al. A deep-learning system for the assessment of cardiovascular disease risk via the measurement of retinal-vessel caliber. Nat Biomed Eng [Internet]. 2021;5(6):498-508. Available from: <https://doi.org/10.1038/s41551-020-00626-4>
- [28] Dai L, Wu L, Li H, Cai C, et al. A deep learning system for detecting diabetic retinopathy across the disease spectrum. Nat Commun [Internet]. 2021;12(1):3242. Available from: <https://doi.org/10.1038/s41467-021-23458-5>
- [29] Kou C, Li W, Liang W, Yu Z, et al. Microaneurysms segmentation with a U-Net based on recurrent residual convolutional neural network. J Med Imaging [Internet]. 2019;6(2):025008. Available from: <https://dx.doi.org/10.1117%2F1.JMI.6.2.025008>
- [30] Xu X, Tan T, Xu F. An Improved U-Net Architecture for Simultaneous Arteriole and Venule Segmentation in Fundus Image. In: Nixon M, Mahmoodi S, Zwiggelaar R (eds). Medical Image Understanding and Analysis. MIUA 2018. Communications in Computer and Information Science [Internet]. Cham: Springer; 2018; 333-340. Available from: https://doi.org/10.1007/978-3-319-95921-4_31
- [31] Yadav G, Maheshwari S, Agarwal A. Contrast limited adaptive histogram equalization based enhancement for real time video system. 2014 International Conference on Advances in Computing, Communications and Informatics (ICACCI) [Internet]. Delhi: IEEE; 2014; 2392-2397. Available from: <https://doi.org/10.1109/ICACCI.2014.6968381>
- [32] Decencière E, Zhang X, Cazuguel G, Lay B, et al. Feedback on a publicly distributed image database: The Messidor database. Image Anal Stereol [Internet]. 2014;33(3):231. Available from: <https://doi.org/10.5566/ias.1155>
- [33] Kaggle. Diabetic Retinopathy Detection. [Internet] Kaggle. 2015. Available from: <https://www.kaggle.com/c/diabetic-retinopathy-detection>
- [34] Porwal P, Pachade S, Kamble R, Kokare M, et al. Indian Diabetic Retinopathy Image Dataset (IDRID) [Internet]. IEEE Dataport; 2018. Available from: <https://dx.doi.org/10.21227/H25W98>
- [35] Decencière E, Cazuguel G, Zhang X, Thibault G, et al. TeleOphta: Machine learning and image processing methods for teleophthalmology. IRBM [Internet]. 2013;34(2):196-203. Available from: <https://doi.org/10.1016/j.irbm.2013.01.010>
- [36] Simonyan K, Zisserman A. Very deep convolutional networks for large-scale image recognition. In: Bengio Y, LeCun Y (eds). 3rd International Conference on Learning Representations, ICLR 2015 [Internet]. San Diego: arXiv;2015; 1-14. Available from: <https://doi.org/10.48550/arXiv.1409.1556>
- [37] He K, Zhang X, Ren S, Sun J. Deep Residual Learning for Image Recognition. 2016 IEEE Conference on Computer Vision and Pattern Recognition (CVPR) [Internet]. Las Vegas: IEEE; 2016; 770-778. Available from: <https://doi.org/10.1109/CVPR.2016.90>
- [38] Woo S, Park J, Lee JY, Kweon IS. CBAM: Convolutional Block Attention Module. In: Ferrari V, Hebert M, Sminchisescu C, Weiss Y (eds). Computer Vision - ECCV 2018. ECCV 2018. Lecture Notes in Computer Science [Internet]. Cham: Springer; 2018; 3-19. Available from: https://doi.org/10.1007/978-3-030-01234-2_1
- [39] Cortes C, Research G, Mohri M, Rostamizadeh A. L2 Regularization for Learning Kernels. 25th Conference on Uncertainty in Artificial Intelligence (UAI 2009) [Internet]. Montreal: Association for Uncertainty in Artificial Intelligence (AUAI); 2009; 109-116. Available from: <https://dl.acm.org/doi/pdf/10.5555/1795114.1795128>
- [40] Ioffe S, Szegedy C. Batch normalization: Accelerating deep network training by reducing internal covariate shift. In Proceedings of the 32nd International Conference on International Conference on Machine Learning - Volume 37 (ICML'15) [Internet]. Lille: JMLR; 2015; 448-456. Available from: <http://proceedings.mlr.press/v37/ioffe15.pdf>
- [41] Srivastava N, Hinton G, Krizhevsky A, Sutskever I, et al. Dropout: A Simple Way to Prevent Neural Networks from Overfitting. J Mach Learn Res [Internet]. 2014; 15(56):1929-1958. Available from: <http://jmlr.org/papers/v15/srivastava14a.html>
- [42] Wisaeng K, Sa-Ngiamvibool W. Exudates Detection Using Morphology Mean Shift Algorithm in Retinal Images. IEEE Access [Internet]. 2019;7:11946-11958. Available from: <http://dx.doi.org/10.1109/ACCESS.2018.2890426>
- [43] van Grinsven MJJP, van Ginneken B, Hoyng CB, Theelen T, et al. Fast Convolutional Neural Network Training Using Selective Data Sampling: Application to Hemorrhage Detection in Color Fundus Images. IEEE Trans Med Imaging [Internet]. 2016;35(5):1273-1284 Available from: <https://doi.org/10.1109/TMI.2016.2526689>

dx.doi.org/10.17488/RMIB.43.2.5

E-LOCATION ID: 1275

Secure Exchange of Medical Images Via Extended Visual Cryptography

Intercambio Seguro de Imágenes Médicas Mediante Criptografía Visual Extendida

Luis Angel Olvera-Martinez , Manuel Cedillo-Hernandez  , Carlos Adolfo Diaz-Rodriguez ,
Enrique Tonatiuh Jimenez-Borgonio 

Instituto Politécnico Nacional, Escuela Superior de Ingeniería Mecánica y Eléctrica (ESIME), Unidad Culhuacán

ABSTRACT

Medical image security is acquiring its importance to preserve the integrity and confidentiality of information (medical data) from malicious users given its importance in timely and successful diagnosis. In this context, several techniques have been developed to protect medical images, such as encryption, data hiding, image tagging, application of Hash algorithms, etc. This paper proposes a technique to cipher medical images by adding the metadata inside a cover image, based on extended visual cryptography as well as the inclusion of a Hash-like function to verify the integrity of the image and the metadata once they are recovered. The method proposed in this work is implemented using medical images with a grayscale resolution of [0,4095] that is a depth of 12 bits/pixel and color images with 24 bits/pixel depth. Experimental results prove the effectiveness of the proposed method in the task of secure exchange of medical images by allowing higher hiding capability, lower distortion in the visual quality of the image with the hidden medical data, as well as a means to verify the integrity of the sent data, compared to state-of-the-art.

KEYWORDS: DICOM imaging, visual cryptography, information security, circular shifting, least significant bit replacement

RESUMEN

La seguridad de imágenes médicas está incrementando su importancia para preservar la integridad y la confidencialidad de la información (datos médicos), frente a usuarios malintencionados dada su importancia en el diagnóstico oportuno y acertado. En este contexto, se han desarrollado varias técnicas para proteger las imágenes médicas, como el cifrado, la ocultación de datos, el etiquetado de imágenes, la aplicación de algoritmos Hash, etc. Este trabajo propone una técnica para cifrar imágenes médicas añadiendo los metadatos dentro de una imagen de cubierta, basada en la criptografía visual extendida, así como la inclusión de una función tipo Hash para comprobar la integridad de la imagen y los metadatos una vez estos sean recuperados. El método propuesto en este trabajo se implementa utilizando imágenes médicas con una resolución en escala de grises de [0,4095] es decir una profundidad de 12 bits/píxel e imágenes en color con 24 bits/píxel de profundidad. Los resultados experimentales demuestran la eficacia del método propuesto en la tarea de transmisión segura de imágenes médicas permitiendo una mayor capacidad de ocultamiento, una menor distorsión en la calidad visual de la imagen con los datos médicos ocultos, así como un medio para comprobar la integridad de los datos enviados, en comparación con los artículos publicados.

PALABRAS CLAVE: Imágenes DICOM, criptografía visual, seguridad de la información, desplazamiento circular, sustitución de bits menos significativos

Corresponding author

TO: Manuel Cedillo-Hernandez

INSTITUTION: Instituto Politécnico Nacional,
Escuela Superior de Ingeniería Mecánica y Eléctrica
(ESIME), Unidad Culhuacán

ADDRESS: Av. Santa Ana #1000, Col. San Francisco
Culhuacán, Culhuacán CTM V, Del. Coyoacán,
C. P. 04440, Ciudad de México, CDMX, México

CORREO ELECTRÓNICO: mcedilloh@ipn.mx

Received:

4 May 2022

Accepted:

22 July 2022

INTRODUCTION

The Digital Imaging and Communications in Medicine (DICOM) file is a standard^[1] with which sundry medical equipment work to produce digital images. In general terms is the way in which the stewardship of medical files services are defined, including the electronic patient record (EPR). In this context, a DICOM file is composed by a data set of pixels with metadata at the header which relates the image with its respective EPR^{[2] [3] [4] [5]}. In this way, the enhancement in technologies like telecom have leave us the growth of services based on DICOM files for medical images transmission throughout Picture Archiving and Communication Systems (PACS), which is a technology that complies the DICOM standard, also allows the creation of different applications such as telemedicine, the remotely diagnose, among others, opening the possibility of give a better clinical analysis or treatment, in interest of the plan of patient's care. Thus, during its lifetime, a medical image can be transmitted several times inside hospitals, or even, outside of them, however, this scenario can introduce some risks regarding to the management and information security that must be mitigated because medical data are confidential^{[2] [3] [4] [5]}, and the conventional informatics security tools such as antivirus, cryptography tools or firewalls, to name a few, cannot solve all security issues of medical data. In this way, data hiding is a research field that has been widely proposed for improving the management and information security of medical imaging, concealing mainly binary data to create a trustworthy link between these data and the image.

So, it is important to ensure that the internet exchanged images correspond from their original images as a malicious user can modify considerable evidence of a patient's condition when they are sent and change the outcome of the patient's diagnosis as has been demonstrated by Yisroel Mirsky^[6]. He modified 2D and 3D medical images by means of a generative adversarial network (GAN) deep neural network. As result the altered images presented variation in tonalities.

To preserve their integrity, various methods or techniques of cryptography^{[7] [8] [9] [10] [11]}, visual cryptography and visual steganography have been developed, both of which are used to hide or protect the information in the images.

Naor and Shamir^[12], first proposed visual cryptography to allow a user to share information through N shares of the secret image and its use has been extended to several applications^[13], since it represents a simple and computationally uncomplicated way to exchange images. On the other hand, there are several techniques used for steganography of images where the information is hidden exclusively in the images, these techniques can be divided into two groups focused on the spatial or frequency domain^{[14] [15] [16] [17]}.

Cryptography differs from steganography in the sense that cryptography focuses on protecting the content of the information while steganography focuses on hiding the information. Both forms allow us to exchange information securely, however neither is perfect and information can be broken or compromised. There are several researchers who propose to implement both techniques allowing to protect and hide the information of an image to increase the security of conventional methods.

Vinothkanna^[18], proposes to implement RSA cryptography incorporated into steganography for files in multiple formats applied to images, to increase security to common stenographic methods. Thus, provides a highly secure transmission of information, to validate his proposal performs *PSNR* and *SSIM* tests, ensuring the efficiency of the method. On the other hand, Gupta Shailender and Ankur Goya^[19], explain that the use of least significant bit (LSB) as a steganography method, in which the LSB of the image is supersede by a bit of the data, is susceptible to steganalysis. However, encrypting the data and hiding it in an image increases the security of the LSB method, with their proposed method concluded that it leads to an increase in execu-

tion time, but the resulting level of security is worth it. Dhiman and Kasana ^[20], present two visual cryptography techniques, in this process the secret image, the cover image and the resulting image have the same dimensions, the pixels selected from the cover image are replaced by pixels from the secret image, this allows the recovered image is the same as the original image. Back to previous work, Richa and Ashwani ^[21], proposed to expand the cover image to make the embedded pixels as imperceptible as possible, as well as increasing the security of the method by encrypting the pixel values of the secret image (medical image), which makes the recovery process more complex.

Despite the above, there are several methods to improve security and, as mentioned above, steganography, cryptography and hashing by themselves may not solve all issues related with the information security. However, the combination of these techniques could improve security, making it more difficult to retrieve information in an unauthorized way. Therefore, the following system is proposed, which is versatile to implement in real scenarios and allows the system to be secure. Using conventional cryptographic techniques such as circular encryption and steganography techniques by substitution of the least significant bits to increase the security of both methods as proposed by Vinothkanna and Gupta.

Employing pixel replacement as proposed by Dhiman and Richa with the variant of considering a cover image, as well as an increase in information because the hidden image has grayscale bit-depth of 12 bits, averaging the replaced pixels to provide some degree of imperceptibility, and finally adding the metadata and providing a system to verify the integrity of the file received by a hash function.

Motivation and contribution

Although the DICOM file has several security standards, these standards do not guarantee that the information it contains cannot be modified. Nowadays,

visual cryptography has focused on protecting the image of the DICOM file obtaining relevant results; however, these proposals leave aside the information related to the image, therefore, a method is proposed to hide both the medical image and its respective metadata in a color cover image of the patient.

The purpose is to briefly identify the user who owns the medical image, as well to allow the medical image to be hidden within an identification image so that it can be sent as a secure transmission media protecting the integrity of the hidden image. An important contribution is related to the recovered medical image having the same bit depth as the original image, this is because the system allows working with medical images with a bit depth equal to or less than 12 bits regardless of whether the bit depth of the covered image is 24 bits/pixel.

On the other hand, the metadata contains information that may be relevant to whoever performs a study on the image, as it contains both medical information and personal information that may be of use to the medical staff, as well as to ensure again that the retrieved DICOM file belongs to the person who appears in the cover image. Including an ID image as a cover image allows both medical institutions and physicians to verify immediately that the face of the person in the image corresponds to the person receiving the studies or being diagnosed is the same, thus allowing a study-patient linkage.

MATERIALS AND METHODS

The DICOM file hiding process is shown in Figure 1, where the medical image and metadata are separated. The medical image is encrypted by the circular encryption method, two images and a key are obtained. The first image contains the four most significant bits, the second one the eight least significant bits. On the other hand, the cover image is splitted into its RGB channels, to hide the data.

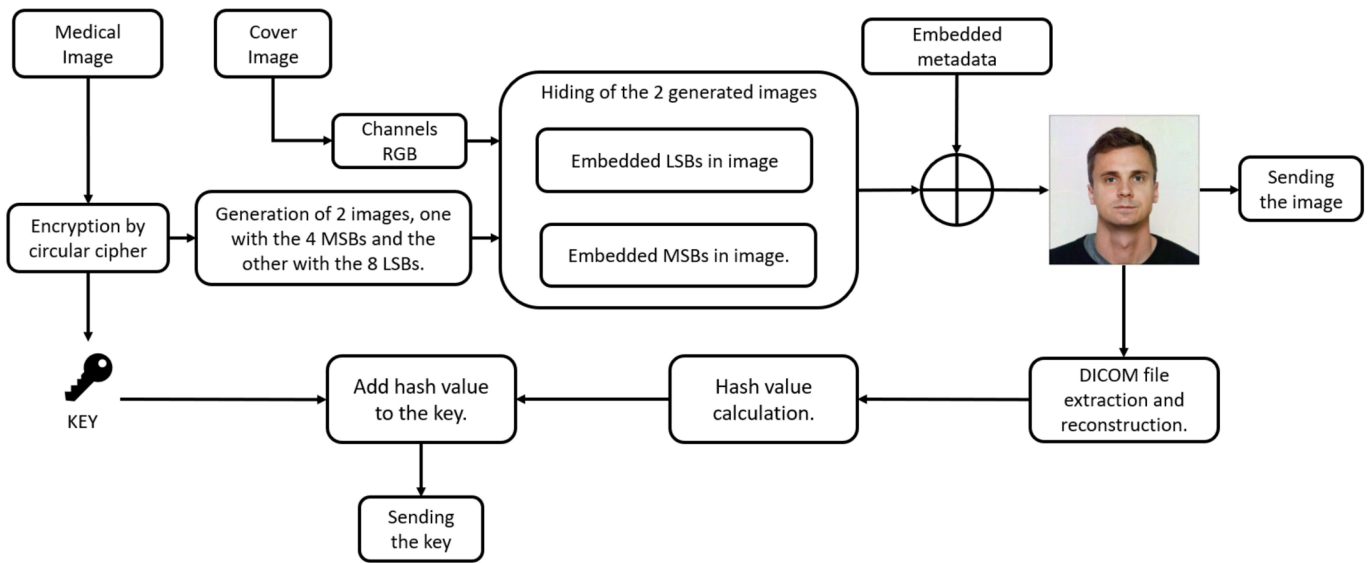


FIGURE 1. DICOM file embedding process.

The obtained two images and the metadata are hidden into the RGB channels of the cover image, resulting in the entire DICOM file embedded into the cover image. To validate the integrity of the DICOM file, it is retrieved to obtain its hash value and add it to the key.

are joined and decrypted, reconstructed DICOM file adding the metadata and then compared with their hash function. The quality of the retrieved medical image is compared with the original, the results are shown in section “Simulation, analysis and results”.

The extraction process shown in Figure 2, retrieves the metadata the Most Significant Bits (MSB's) and Least Significant Bits (LSB's) images. Then, the images

To have a better understanding of the methodology, the following subsections describe in greater detail each stage that makes up the proposal.

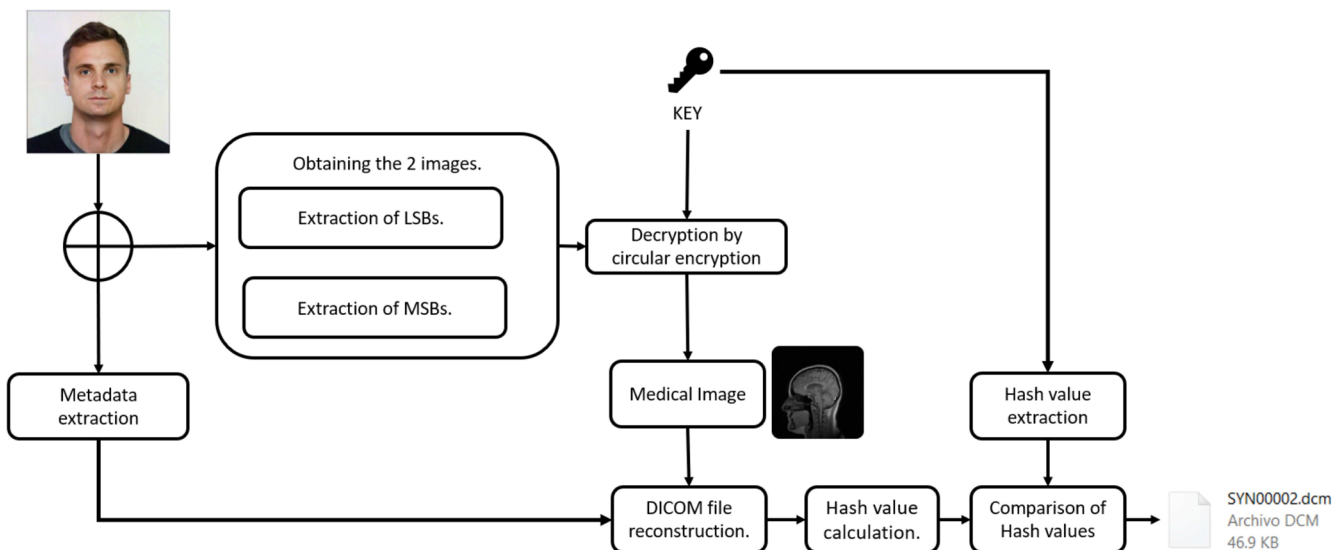


FIGURE 2. DICOM file extraction process

The encryption is described in subsection “Circular shift encryption”. The embedding of image with the remaining most significant bits is described in subsection “Embedded MSBs in cover image” and the least significant bits in subsection “Embedded LSBs in image”, the embedding of metadata information in subsection “Embedded metadata”, obtaining the SHA256 of the resulting DICOM file in subsection “Digital signature”. Finally, the extraction process of medical image and metadata information in subsection “Extraction Procedure”.

Circular shift encryption

The circular Shift Encryption process shifts the columns and rows n positions to right and down respectively [22]. The number of shifts depends on certain values contained on a previously defined key. E.g., assuming a small key, which value is (2,3,0,1) applied to an (5*5) array; the following steps are showed:

1. The first digit (2) performs a circular right shift.
2. The second digit (3) performs a circular down shift.
3. Steps 1 and 2 are looped until completing all digits
4. If the digit is zero, no shift is performed. Show Figure 3.

The key is pre-computed through a series of random numbers stored in a one-dimensional array, the length of the array corresponds to the width of the cover image, and the maximum number stored corresponds to the maximum value of the dimensions of the cover image.

It is important to assume that the maximum depth of the medical image is 12 bits, with the selected image, the circular encryption process is performed. The resulting medical image is converted into two arrays (images) one of 4 bits most significant bits (MSB) and the other of least significant bits (LSB) 8bits.

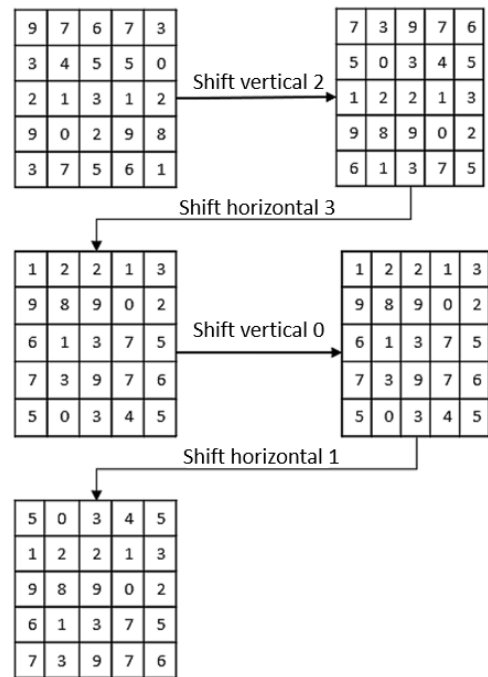


FIGURE 3. Circular Shift Encryption.

Embedded MSBs in cover image

In order to embed an MSB array, we select a 3x3 pixel array of each RGB channel from the cover image. From each RGB arrays, 3 non-deterministic selected pixels will be used to embed the values of the MSB array as shown in Figure 4.

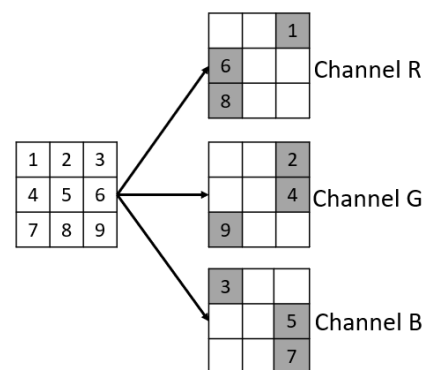


FIGURE 4. Pixel selection in channels RGB.

The pixel values in the MSB group will be embedded by modifying the last 4 bits of the selected pixels in each of the RGB channels, as shown in Figure 5, where the first row of the MSB array was selected and the last 4 bits of the selected pixels in the RGB channels were replaced.

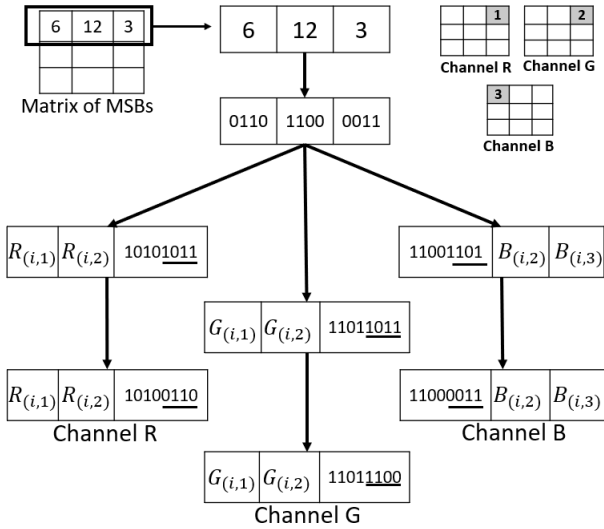


FIGURE 5. Embedded MSBs in channels RGB.

Embedded LSBs in cover image

Same as the MSB embedding process, a 3×3 pixels array is selected for the LSB group. Then 3 non-deterministically selected pixels of each RGB channels, excluding those pixels that were already modified previously, as shown in Figure 6.

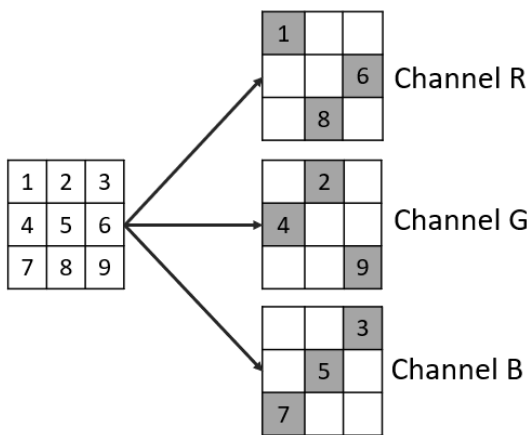


FIGURE 6. Pixel selection in channels RGB.

The values of the LSBs are embedded by replacing them with the value of the selected pixels, then each value inserted is averaged with the neighboring pixels whose values have not been modified. Considering that the embedded LSBs pixels have a value within the

range of 0 to 254, averaging makes the value be imperceptible as well as being in the range of values allowed in the 8-bit cover image, as shown in Figure 7.

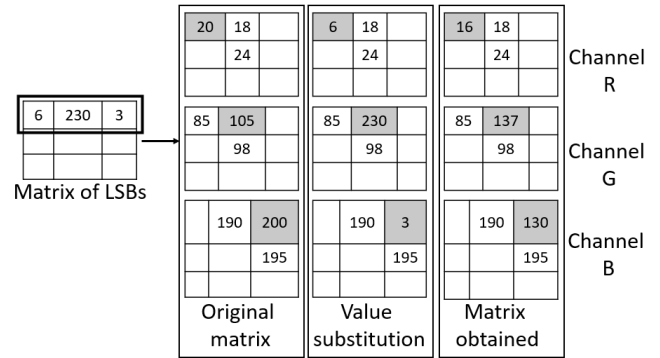


FIGURE 7. Embedded LSBs in channels RGB.

Embedded metadata

The DICOM file's metadata are relevant, since may contain patient ID information, the performed study; the medical equipment used; the medical institution information; image characteristics such as color, model, dimensions, bit resolution, etc. Therefore, it is crucial select the data that may be helpfully for the diagnosis.

For this proposal, selected data include ID data and data on the study performed, to be useful for the physician or medical institution.

Before performing the embedding, first an array of the same medical image dimensions is generated. The $n_i \times m_i$ position of the array will contain the ASCII value of each of the i -th letter information.

To embed the information, two pixels are selected at position n_i, m_j of each of the RGB channels. The selected pixels should not be those whose value has been changed during the embedding process of the medical image.

Each letter has an 8 bits assigned in the ASCII code. Therefore, the process modifies the last 4 bits of the selected pixels in the position n_i, m_j of the cover image.

There must be 2 pixels in the position n_i, m_j whose value had not been modified in the RGB channels, this ensures to hide a letter of the metadata in that position for the RGB channels. Modifying the last 4 bits of the cover image allows to preserve an imperceptibility at the moment of viewing the image.

Digital Signature

After the reconstruction of the DICOM file, it must be verified to make sure that it has not been altered. To verify the information's integrity, it is proposed to use the Secure Hash Algorithm (SHA-256) [23], of the sent file. Once the hash has been calculated, the hash is compared with hash that was received, as is shown in Figure 8.

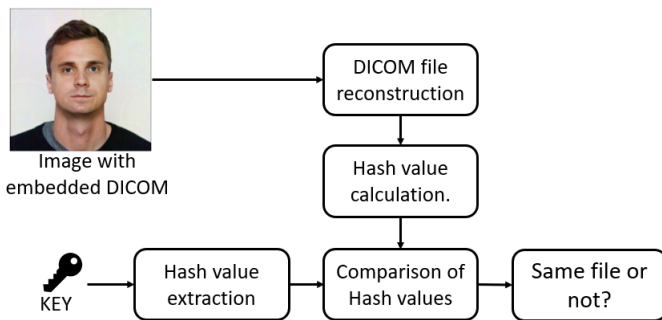


FIGURE 8. Obtaining hash value for validation.

In the process of reconstructing the DICOM file by the receiver, the SHA256 of the received file is recalculated and compared with the signature of the key file.

The objective of this process is to ensure that the reconstructed file was not modified by an external person, if the result of the comparison of both hashes match, it can be concluded that the DICOM file sent and the one obtained by the receiver are the same. In case of a function comparison mismatch, the received file should be discarded, which means that has been altered.

Extraction procedure

Once the cover image is received, the process to reconstruct the DICOM file starts. The steps for the extraction procedure are given below and show in Figure 2.

1. For every cover image's RGB channel, LSBs and MSBs images are extracted.
2. Both images are combined according to the position of the MSBs and LSBs.
3. The resulting image is decrypted with the key.
4. Metadata is extracted from the cover image.
5. The DICOM file is reconstructed with the metadata and the resulting medical image.

RESULTS AND DISCUSSION

The proposed method was tested in MATLAB, in a 16 GB RAM machine and 3Ghz processor. The tests were performed using a set of 10 MRI images consisting of 2 body parts, side view of the head and brain, with a depth of 12 bits or a maximum hue level of 4095. The images in Figure 9, constitute the set of medical images corresponds to a dataset provided by Instituto Mexicano del Seguro Social (IMSS) for research purposes.

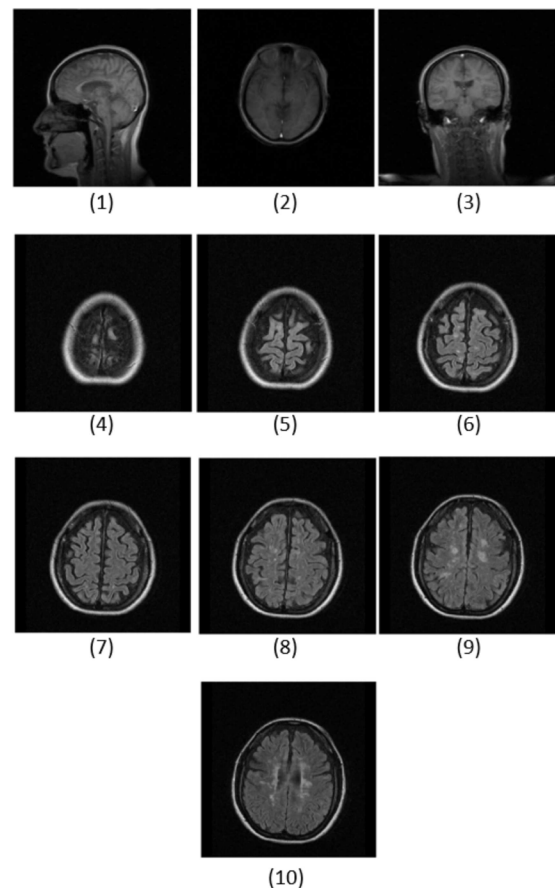


FIGURE 9. DICOM medical images used in the experiment.

On the other hand, the patient identification images used as cover images, have different background colors, clothing, as well as different skin and hair tones, shown in Figure 10 (a). The images used in this process are 255x255.

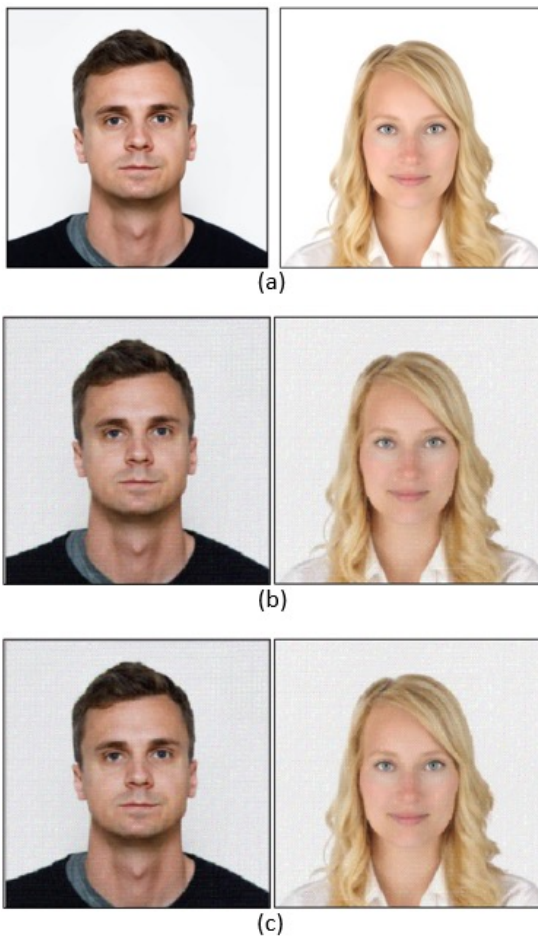


FIGURE 10. (a) Cover images, (b) Resulting cover images with only embedded DICOM image, (c) Resulting cover image with DICOM image and metadata.

The dimensions of the test images are multiples of 3, in case both images are not multiples of 3, both images are analyzed to eliminate those rows and/or columns that contain little or no relevant information in order not to distort both images.

The medical image of dimensions 255x255 with a depth of 12 bits contains approximately 780,300 bits as shown:

$$255 \times 255 \times 12 \text{ Bit depth} = 780,300 \text{ bits} \quad (1)$$

While the color cover image with the same dimensions and a depth of 8 bits in each of the RGB channels contains 1,560,600 bits as shown below:

$$255 \times 255 \times 8 \text{ Bit depth} \times 3(\text{RGB}) = 1,560,600 \text{ bits} \quad (2)$$

It can be concluded that the cover image has the capacity to store the medical image as well as the respective metadata.

From the test DICOM file, the medical image is extracted to begin the image and metadata embedding process, as is described in section “Proposed methodology”. After the encryption, the image is shown in Figure 11.

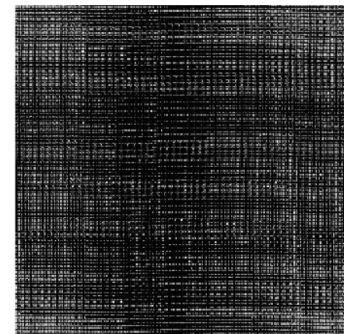


FIGURE 11. Encrypted medical image.

Then is converted to a 12-bit image and splitted into two images with a resolution of 8 bits and 4 bits the resulting images are shown in Figure 12, respectively.

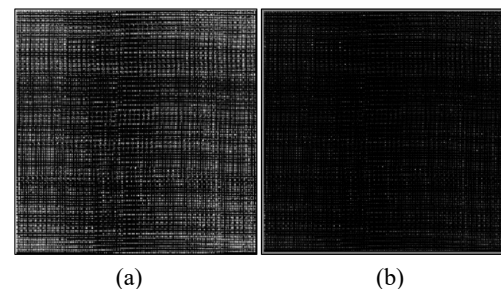


FIGURE 12. (a) Image with the 8 LSBs and (b) image with the 4 MSBs

With both resulting images, the embedding process is performed. Since in the MSB process the values of certain pixels are modified and in the LSB embedding process, the adjacent pixels of which some pixels were previously modified are considered, this order allows the hue level of the recovered pixel be like the original pixel and the changes made in the patient identification image to be less visible. The resulting image of the patient once the embedded process was performed shows in Figure 10 (b).

In the LSB embedding process, it is considered that one third of the cover image will be modified, so calculating the number of bits to be modified, the following result is obtained:

$$1,560,600 \text{ bits} / 3(\text{RGB}) = 520,200 \text{ bits} \quad (3)$$

On the other hand, if we calculate the number of bits contained in the LSB image, we obtain the following result:

$$255 \times 255 \times 8 \text{ Bit depth} = 520,200 \text{ bits} \quad (4)$$

As can be observed, the space available in the cover image coincides with the space used to hide the bits in the LSB image. From the MSB embedding process, if we calculate the number of bits in the MSB image, we obtain the following result:

$$255 \times 255 \times 4 \text{ Bit depth} = 260,100 \text{ bits} \quad (5)$$

Adding the values of (4) and (5) gives the number of bits to be hidden calculated as (1), so there is no loss of bits.

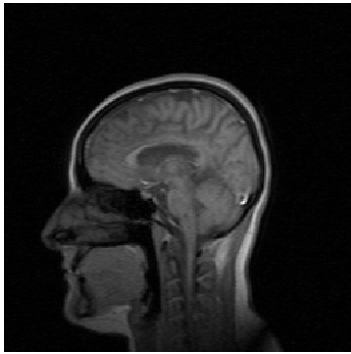
As is previously mentioned, the DICOM formats contain a diverse collection of data from which it will be select the crucial data needed a correct diagnosed, Table 1, shows the selected data in the test DICOM file.

TABLE 1. Selected data.

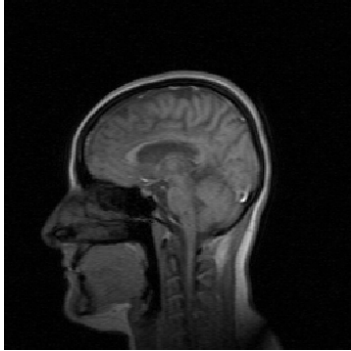
DICOM metadata field	Type
Format	CHAR
Width	INT
Height	INT
Bit Depth	INT
Color Type	CHAR
Study Date	INT
Accession Number	INT
Modality	CHAR
Study Description	CHAR
Code Meaning	CHAR
Resolution Factor	CHAR
Private Creator	CHAR
Manufacturer	INT
Institution Name	INT
Name	CHAR
Last Name	CHAR
Patient ID	INT
Patient Birthday	INT
Patient Sex	CHAR
Image Text	CHAR

With the selected data the array is generated, with $n \times m$ dimensions like the cover image where in the position n_i, m_j it will contain a character, corresponding to the data. Once the array is filled, the data is inserted in the cover image as indicated section “Embedded metadata”. The resulting image is shown in Figure 10 (c). Once the DICOM file embedding process is finished, the resulting image is sent to the receiver, who then extracts the medical image as well as the metadata and reconstructs the DICOM file, calculates its SHA256 value and extracts the one contained in the key, compares both values to verify that the file preserves its integrity and was unmodified during its sending.

After verifying the integrity of the DICOM file, the similarity as also the quality of the recovered image with respect to the original medical image is determined by Peak Signal to Noise Ratio (PSNR) and Similarity Index Metrix (SSIM) tests [24], the original medical image and the recovered image are shown in Figure 13.



(a) Original medical image.



(b) Reconstructed medical image.

FIGURE 13. Original medical image and resulting medical image.

PSNR test is measure of reconstruction quality of an image, if the calculated value for *PSNR* is high or tends to infinity it is concluded that the image recovered quality is similar compared

PSNR calculates the image quality ratio between the signal power and the distorting noise. This ratio is in decibels and the equation is expressed as ^[21]:

$$PSNR = 10 \log\left(\frac{peakval^2}{MSE}\right) \quad (6)$$

From (6) peakval (Peak Value) is the maximum pixel value of the image, if it is an 8-bit image, the maximum value is 255, and MSE is the Mean Square Error defined as follow:

$$MSE = \frac{1}{MN} \sum_{n=0}^M \sum_{m=1}^N [\hat{g}(n, m) - g(n, m)]^2 \quad (7)$$

On the other hand, the *SSIM* ^{[25] [26]} is used to measure the similarity between two images with respect to 3 factors which can be expressed as:

$$SSIM(x, y) = f(l(x, y), c(x, y), s(x, y)) \quad (8)$$

from which:

l is the brightness between two images comparison

c is the contrast distortion, which differs the brightest and darkest ranges

s is the correlation loss, it compares the pattern of local luminance

The luminescence distortion, contrast distortion and correlation loss can be expressed separately as:

$$l(x, y) = \frac{2\mu_x\mu_y + C_1}{\mu_x^2 + \mu_y^2 + C_1} \quad (9)$$

$$c(x, y) = \frac{2\sigma_x\sigma_y + C_2}{\sigma_x^2 + \sigma_y^2 + C_2} \quad (10)$$

$$s(x, y) = \frac{\sigma_{xy} + C_3}{\sigma_x\sigma_y + C_3} \quad (11)$$

If the value of *SSIM* is close to 1 it is concluded that the original image and the recovered image are structurally similar.

The results obtained by implementing the proposed method are shown in Table 2.

TABLE 2. Imperceptibility results.

	PSNR	SSIM
Cover Image 1	94.6233	0.9876
Cover Image 2	94.600	0.9875

The proposed method was applied to the rest of the medical images using only the cover image 1, the *PSNR* and *SSIM* tests were performed, the values obtained are shown in Table 3.

TABLE 3. Visual quality results in terms of *PSNR* and *SSIM*.

DICOM images ID	PSNR	SSIM
1	94.6233	0.9876
2	94.5824	0.9843
3	94.5699	0.9867
4	86.5022	0.9898
5	89.7878	0.9884
6	86.4916	0.9896
7	92.3604	0.9885
8	89.7604	0.9876
9	92.3575	0.9891
10	86.9698	0.9874
Average	90.8005	0.9879
DICOM images ID	PSNR	SSIM

In the same way, Figure 14, shows some results of the tests performed, on the left the original images and on the right the reconstructed images, where at first sight they do not present any alteration now of being recovered by the receiver.

Table 4, compares the *PSNR* obtained from the original medical image and the encrypted image with the results obtained by implementing the proposal of Richa and Ashwani [16]. In this case, a minimum value of *PSNR* is expected since it ensures that the original medical image and the encrypted image are no correlated and as can be appreciated our results obtain lower values, inferring that the correlation between the two images is lower with the results previously published.

Although Richa only evaluates in terms of *PSNR*, based on the contributions presented here, it is possible to have a very detailed comparison of the processes performed, for example, Richa considers medical images with a depth of 8 bits and 3 cover images, expanding them to have a greater hiding capacity. On

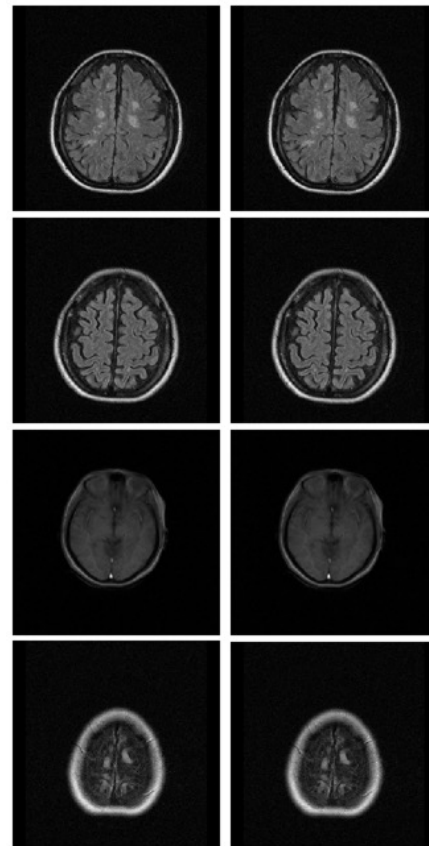


FIGURE 14. Results obtained.

the other hand, the methodology proposed in this paper allows hiding medical images up to a bit depth of 12 bits and adding the metadata, only one cover image is considered without expanding it and finally a way to verify the integrity of the file sent by a HASH function is included, adding value to the results obtained.

TABLE 4. *PSNR* (dB) of original images vs encrypted image.

DICOM Image ID	Proposed method	Richa [21]
1	56.1543	56.4547
2	56.0163	56.2816
3	56.4283	56.6693
4	52.4912	52.6509
5	52.3014	52.4326
6	51.4581	51.5942
7	51.0167	51.2845
8	50.6105	50.8029
9	50.0141	50.1966
10	50.8472	50.9351

CONCLUSIONS

The proposal provides a way to embed a medical image, as well as its respective metadata in the RGB channels in an identification patient's image. Allowing medical institutions securely share the DICOM file to preserve its integrity. For this purpose, stenographic and cryptographic techniques were combined, which proves to increase the security of conventional methods as supported in the previous research, making tough the information retrieval by malicious users.

On the other hand, the proposed method allows working with medical images with a bit-depth of more than 8 bits/pixel and incorporates the metadata, allowing a greater capacity to hide data within the color image, compared to the methods already proposed, because these methods only work with medical images with a bit-depth of 8 bits/pixel and without considering the metadata hiding.

The fact of using an ID image allows the medical institutions in responsible for delivering and evaluating the medical images to verify at a naked eye that the face of the person in the ID image corresponds to the actual patient receiving the studies, thus allowing the study-patient linkage.

Finally, experimental results prove that the proposed methodology allows the resulting image (ID image with the hidden medical data) in comparison with the original image, to have changes in tonalities that are the least perceptible to the human eye, in addition to

providing an outstanding level of medical image recovery in terms of visual quality and similarity as demonstrated in the resulting *PSNR* and *SSIM* tests.

As part of future work this methodology is proposed to be applied to other color models to increase the level of security and to make it more difficult to obtain the data embedded in the cover image as well as to improve the resulting visual quality. On the other hand, it is considered to implement it in other medical imaging modalities as well as its application to 3D medical imaging.

AUTHOR CONTRIBUTIONS

L.A.O.M. conceptualized the project, participated in the use of specialized software and developed the methodology, carried out research, formal analysis and visualization, participated in the writing of the manuscript. M.C.H. conceptualized the project, developed the methodology, participated in validation of data and/or results and data curation, carried out formal analysis and visualization, contributed providing resources and funding, oversaw the project. E.T.J.B. conceptualized the project, participated in the use of specialized software, and carried out research and visualization. C.A.D.R. conceptualized the project, participated in the development and implementation of the methodology, carried out formal analysis and data validation, carried out visualization, oversaw the project, participated in the writing, editing, and reviewing of the original manuscript. All authors reviewed and approved the final version of the manuscript.

REFERENCES

- [1] National Electrical Manufacturers Association. DICOM Security [Internet]. DICOM Digital Imaging and Communication in Medicine; 2019. Available from: <https://www.dicomstandard.org/using/security>
- [2] Coatrieux G, Quantin C, Montagner J, Fassa M, et al. Watermarking medical images with anonymous patient identification to verify authenticity. *Stud Health Technol Inform* [Internet]. 2008;136:667-672. Available from: <https://pubmed.ncbi.nlm.nih.gov/18487808/>
- [3] Qasim AF, Meziane F, Aspin R. Digital watermarking: Applicability for developing trust in medical imaging workflows state of the art review. *Comput Sci Rev* [Internet]. 2018;27:45-60. Available from: <https://doi.org/10.1016/j.cosrev.2017.11.003>
- [4] Mousavi SM, Naghsh A, Abu-Bakar SAR. Watermarking Techniques used in Medical Images: a Survey. *J Digit Imaging* [Internet]. 2014;27(6):714-729. Available from: <https://doi.org/10.1007/s10278-014-9700-5>
- [5] Cedillo-Hernandez M, Cedillo-Hernandez A, Nakano-Miyake M, Perez-Meana H. Improving the management of medical imaging by using robust and secure dual watermarking. *Biomed Signal Process Control* [Internet]. 2020;56:101695. Available from: <https://doi.org/10.1016/j.bspc.2019.101695>
- [6] Mirsky Y, Mahler T, Shelef I, Elovici Y. CT-GAN: malicious tampering of 3D medical imagery using deep learning. In: *Proceedings of the 28th USENIX Conference on Security Symposium* [Internet]. Santa Clara, CA; 2019:461-478. Available from: <https://doi.org/10.48550/arXiv.1901.03597>
- [7] Stallings W. *Cryptography and network security: Principles and practice* [Internet]. New York: Prentice Hall; 2011. 719p. Available from: <http://pozi.omsu.ru/docs/docs/stallings.pdf>
- [8] Medina Velandia LN. *Criptografía y mecanismos de seguridad* [Internet]. Bogotá: Fundación Universitaria del Área Andina; 2017. 141p. Available from: <https://digitk.areandina.edu.co/handle/areandina/1423>
- [9] Blackledge J, Bezobrazov S, Tobin P, Zamora F. Cryptography using evolutionary computing. In: *24th IET Irish Signals and Systems Conference (ISSC 2013)* [Internet]. Letterkenny: Institution of Engineering and Technology; 2013:1-8. Available from: <https://doi.org/10.1049/ic.2013.0029>
- [10] Diffie W, Hellman M. New directions in cryptography. *Secure communications and asymmetric cryptosystems*. *IEEE Trans Inf Theory* [Internet]. 1976;22(6):644-654. Available from: <https://doi.org/10.1109/TIT.1976.1055638>
- [11] Menezes AJ, van Oorschot PC, Vanstone SA. *Handbook of Applied Cryptography* [Internet]. Boca Raton: CRC press; 2018. 810p. Available from: <https://doi.org/10.1201/9780429466335>
- [12] Naor M, Shamir A. Visual cryptography. In: De Santis A (eds). *EUROCRYPT'94. EUROCRYPT 1994. Lecture Notes in Computer Science, vol 950* [Internet]. Berlin: Springer; 1994:1-12. Available from: <https://doi.org/10.1007/BFb0053419>
- [13] Olvera-Martinez L, Jimenez-Borgonio T, Frias-Carmona T, Abarca-Rodríguez M, et al. First SN P visual cryptographic circuit with astrocyte control of structural plasticity for security applications. *Neurocomputing* [Internet]. 2021;457(7):67-73. Available from: <https://doi.org/10.1016/j.neucom.2021.05.057>
- [14] Morkel T, Eloff J, Olivier M. An overview of image steganography. In: Eloff JHP, Labuschagne L, Eloff MM, Venter HS (eds). *Proceedings of the ISSA 2005 New Knowledge Today Conference* [Internet]. Pretoria: ISSA; 2005. 1-11p. Available from: http://icsa.cs.up.ac.za/issa/2005/Proceedings/Full/098_Article.pdf
- [15] Cox IJ, Pakura G, Sheel M. Information Transmission and Steganography. In: Barni M, Cox I, Kalker T, Kim HJ (eds). *Digital Watermarking. IWDW 2005. Lecture Notes in Computer Science, vol 3710* [Internet]. Siena, Italy: Springer; 2005. 15-17. Available from: https://doi.org/10.1007/11551492_2
- [16] Wu X, Qiao T, et al. Sign steganography revisited with robust domain selection. *Signal Process* [Internet]. 2022;196:108522. Available from: <https://doi.org/10.1016/j.sigpro.2022.108522>
- [17] Yousefi Valandar M, et al. A chaotic video steganography technique for carrying different types of secret messages. *J Inf Secur Appl* [Internet]. 2022;66:103160. Available from: <https://doi.org/10.1016/j.jisa.2022.103160>
- [18] Vinothkanna R. A secure steganography creation algorithm for multiple file formats. *J Innov Image Process* [Internet]. 2019;1(01):20-30. Available from: <https://doi.org/10.36548/jiip.2019.1.003>
- [19] Gupta A, Goyal A, Bhushan B. Information Hiding Using Least Significant Bit Steganography and Cryptography. *Int J Mod Educ Comput Sci* [Internet]. 2012;4(6):27-34. Available from: <https://doi.org/10.5815/ijmecs.2012.06.04>
- [20] Dhiman K, Kasana SS. Extended visual cryptography techniques for true color images. *Comput Electr Eng* [Internet]. 2018;70:647-658. Available from: <https://doi.org/10.1016/j.compeleceng.2017.09.017>
- [21] Maurya R, Kannojiya AK, Rajitha B. An Extended Visual Cryptography Technique for Medical Image Security. In: *2020 2nd Int Conf on Innov Mech for Ind App (ICIMIA)* [Internet]. Bangalore, India: IEEE; 2020: 415-421. Available from: <https://doi.org/10.1109/ICIMIA48430.2020.9074910>
- [22] Omari AH, Al-Kasasbeh BM, Al-Qutaish RE, Muhairat MI. A new cryptographic algorithm for the real time applications. In: Zaharim A, Mastorakis N, Gonos I (eds). *Proceedings of the 7th WSEAS international conference on Information security and privacy* [Internet]. Cairo, Egypt; World Scientific and Engineering Academy and Society (WSEAS). 2008: 33-38. Available from: <https://dl.acm.org/doi/10.5555/1576645.1576651>
- [23] Schneier B. *Applied Cryptography* [Internet]. Indianapolis: John Wiley & Sons; 1996. 784p. Available from: <https://www.schneier.com/books/applied-cryptography/>
- [24] Horé A, Ziou D. Image Quality Metrics: PSNR vs. SSIM. *20th Int Conf on Pat Rec* [Internet]. Istanbul, Turkey; IEEE. 2010: 2366-2369. Available from: <https://doi.org/10.1109/ICPR.2010.579>
- [25] Sara U, Akter M, Uddin MS. Image Quality Assessment through FSIM, SSIM, MSE and PSNR-A Comparative Study. *J Comput Commun* [Internet]. 2019;7(3):8-18. Available from: <https://doi.org/10.4236/jcc.2019.73002>
- [26] Wang Z, Bovik AC, Sheikh HR, Simoncelli EP. Image quality assessment: from error visibility to structural similarity. *IEEE Trans Image Process* [Internet]. 2004;13(4):600-612. Available from: <https://doi.org/10.1109/TIP.2003.819861>